Magnon spintronics in non-collinear magnetic insulator/metal heterostructures

Aqeel, Aisha

Magnon Spintronics in non-collinear magnetic insulator/metal heterostructures

Aisha Aqeel

university of groningen / faculty of mathematics and natural sciences / zernike institute for advanced materials

Zernike Institute PhD thesis series 2017-02
ISSN: 1570-1530
ISBN: 978-90-367-9360-5
ISBN: 978-90-367-9359-9 (electronic version)

The work described in this thesis was performed in the research groups Solid State Materials for Electronics and Physics of Nanodevices of the Zernike Institute for Advanced Materials at the University of Groningen, the Netherlands. This work was supported by NanoLab NL and the Zernike Institute for Advanced Materials.

Printed by: Ipskamp Printing, Enschede

rijksuniversiteit
groningen

Magnon Spintronics in non-collinear magnetic insulator/metal heterostructures

Proefschrift

ter verkrijging van de graad van doctor aan de
Rijksuniversiteit Groningen
op gezag van de
rector magnificus prof. dr. E. Sterken,
en volgens besluit van het College voor Promoties.

De openbare verdediging zal plaatsvinden op

vrijdag 10 februari 2017 om 12:45 uur

door

Aisha Aqeel

geboren op 8 juli 1988
te Punjab, Pakistan

Promotors
Prof. dr. T. T. M. Palstra
Prof. dr. ir. B. J. van Wees

Beoordelingscommissie
Prof. dr. C. H. Back
Prof. dr. B. Koopmans
Prof. dr. J. T. Ye

To my parents

Contents

1 Introduction **1**
- 1.1 Spintronics . . . 1
- 1.2 Magnon Spintronics: A new approach towards dissipationless spin electronics 2
- 1.3 Motivation and Outline . . . 2
- Bibliography . . . 5

2 Concepts of spin transport in metal|magnetic insulator heterostructures **7**
- 2.1 Spin transport in normal metal|magnetic insulator heterostructures . . . 7
- 2.2 Pure spin currents . . . 8
- 2.3 Generation (detection) of spin currents by (inverse) spin Hall effect . . . 10
- 2.4 Spin Hall magnetoresistance . . . 12
- 2.5 Spin-mixing conductance at the insulator|metal interface . . . 13
- 2.6 Spin-caloritronic effect: spin Seebeck effect . . . 14
- 2.7 Magnetic insulators . . . 16
  - 2.7.1 Non-collinear magnetic insulators . . . 17
  - 2.7.2 Non-centrosymmetric magnetic insulators . . . 18
  - 2.7.3 Low-dimensional magnetic systems . . . 18
- 2.8 Device fabrication and measurement techniques . . . 19
  - 2.8.1 Electron-beam lithography . . . 19
  - 2.8.2 Lock-in detection . . . 21
  - 2.8.3 Measurement Setup . . . 22
- Bibliography . . . 24

3 Spin Seebeck effect in a single crystal YIG|Pt system **31**
- 3.1 Introduction . . . 31
- 3.2 Experimental technique . . . 32
- 3.3 Results and discussion . . . 34
- 3.4 Conclusions . . . 39
- Bibliography . . . 41

4 Spin-Hall magnetoresistance and spin Seebeck effect in multiferroic $CoCr_2O_4$ films 45
4.1 Introduction . . . 45
4.2 Sample growth and characteristics . . . 47
4.2.1 $CoCr_2O_4$ film magnetization . . . 48
4.3 Measurement techniques . . . 48
4.3.1 Lock-in detection . . . 49
4.4 Results and discussion . . . 50
4.4.1 Spin-Hall magnetoresistance in Pt|$CoCr_2O_4$ . . . 50
4.4.2 Spin Seebeck effect in Pt|$CoCr_2O_4$ . . . 54
4.4.3 SMR and the SSE in Pt|$CoCr_2O_4$ vs. Pt|YIG . . . 57
4.5 Conclusions . . . 58
Bibliography . . . 60

5 Electrical detection of spiral spin structures in Pt|Cu_2OSeO_3 heterostructures 65
5.1 Introduction . . . 65
5.2 Experimental procedure . . . 67
5.3 Results and discussion . . . 68
5.3.1 Spin-Hall magnetoresistance . . . 68
5.3.2 Spin Seebeck effect . . . 71
5.4 Conclusion . . . 72
5.5 Appendix . . . 73
5.5.1 Sample characteristics and measurement technique . . . 73
5.5.2 First harmonic response in Pt on the Cu_2OSeO_3 crystal . . . 75
5.5.3 Continuum model for the SMR effect in Pt|Cu_2OSeO_3 . . . 77
5.5.4 Second harmonic response in Pt|Cu_2OSeO_3 . . . 80
Bibliography . . . 82

6 Probing current-induced magnetic fields in Au|YIG heterostructures with LEμSR 87
6.1 Introduction . . . 87
6.2 Device fabrication and measurement technique . . . 88
6.3 Results . . . 90
6.4 Conclusions . . . 94
Bibliography . . . 96

7 Growth of non-centrosymmetric Cu_2OSeO_3 single crystals 99
7.1 Introduction . . . 99
7.2 Synthesis and experimental methods . . . 100
7.3 Results . . . 101
7.4 Discussion . . . 103
7.4.1 Chemical vapor transport . . . 103
7.4.2 Absolute structure determination . . . 104
7.4.3 Broadband helimagnon resonance measurements . . . 105
7.5 Conclusions . . . 107
Bibliography . . . 108

Summary **110**

Samenvatting **116**

Acknowledgements **122**

Publications **127**

Chapter 1

Introduction

1.1 Spintronics

Today's technology-oriented world with billions of daily-use electronic devices including computers and mobile phones could never have been realized without the availability of small and cheap information storage devices. Interestingly, these devices including the modern hard drives, utilize not the charge of the electron but its intrinsic angular momentum called the electron spin. The famous demonstration of the potential of spintronics to be used in electronic devices was done by A. Fert [1] and P. Grünberg [2] in 1988 by the discovery of the Giant Magneto Resistance (GMR) effect and they were rewarded with the Nobel Prize in Physics in 2007 for their discovery. The GMR effect, the working principle for read-out in today's hard drives, makes it possible to read out the magnetic state of a tiny magnetic domain, as a change in the electrical resistance depending on the relative magnetic alignment of magnetic domains. Every tiny magnetic domain therefore will act as a distinct binary (1/0) magnetic state. Together with the successful downscaling of the size of a stable bit, hard disks can be packed with areal densities reaching up to 128 GBit/cm^2 dramatically lowering the cost down to \$0.032 per gigabyte till now.

Over the last two decades in the field of spintronics, different methods have been investigated to use the electron's spin degree of freedom for storage, transport and manipulation of information. For example, in the spin-valves, a typical spintronics device with two magnetic layers for information storage, the GMR effect is used to read the magnetic states. Spin transfer torque (STT) [3, 4] is used to manipulate the spin information. Spintronic devices, including spin-valves, are mostly based on the flow of spin-polarized charge currents. Undoubtedly, spintronics has uncovered many fundamental questions in pursuit of its goal to control electronic spin currents and their interaction with magnetic order in metals. Several spin-related phenomena including spin transfer torque in magnetic layers [3, 4], spin pumping driven by magnetization precession [5, 6] and thermally induced spin currents [7–9] are being currently used to manipulate spin currents in metallic systems. However, spin currents in magnetic metals carried by moving electrons are limited by spin relaxation and Joule heating.

1.2 Magnon Spintronics: A new approach towards dissipationless spin electronics

Magnon spintronics is the field of spintronics in which the spin currents are carried by magnons instead of moving charge carriers. Magnons are the quanta of collective spin-wave excitations in magnetic materials. Magnons are *charge current free* and, therefore, less subject to dissipation caused by scattering with impurities on the atomic level. This renders magnons a promising information carrier alternative compared to electric (spin) currents. Spintronics in magnetic insulators is fundamentally different from that in metals and gives rise to quantum many-body phenomena that lie beyond the paradigm of single-electron spintronics [10]. Magnon spintronics promises to find ways to exploit magnonic spin currents for novel energy-harvesting and power-conserving spintronics technologies that are urgently needed for tomorrow's information society [11].

Magnon spintronics came into focus by two recent discoveries that demonstrate the conversion between charge currents carried by itinerant electrons and magnonic spin currents at an interface between a normal metal and a magnetic insulator. This conversion can be driven thermally [12] or electrically [13], and opens the possibility for integrating electron and magnon spintronics. In the long term, these breakthroughs may lead to novel device concepts that exploit magnons for spin transport with minimal dissipation over much longer distances than the spin relaxation lengths.

1.3 Motivation and Outline

The research presented in this thesis focusses on the growth of complex magnetic materials with unique magnetic properties and experimental investigation of fundamental spintronic phenomena in these magnetic insulators with magnetic orders varying from collinear to non-collinear chiral spin structures. The usage of non-collinear magnetic insulators for spintronic devices opens up not only the possibility to study and control pure spin currents but also their interaction with non-collinear nano-magnetic spin structures like helices and skyrmions. We study different spintronic effects including spin Hall magnetoresistance (SMR) and spin-caloritronics effects like spin Seebeck effect (SSE) by using a metal|insulator bilayer nanoscale device configuration. In these bilayer devices a Pt metal electrode, with large spin-orbit coupling, is used to electrically inject or detect spin currents. The magnetic insulators including prototype yttrium iron garnet - $Y_3Fe_5O_{12}$ (a room-temperature collinear magnetic insulator), cobalt chromate - $CoCr_2O_4$ (a non-collinear magnet) and copper oxoselenite - Cu_2OSeO_3 (a chiral magnet) are investigated in these bilayer devices. Moreover, some investigations have been carried out by replacing Pt metal by Au on top of a magnetic insulator.

This thesis consists of the following chapters, of which a brief overview is given below:

- *Chapter 2* introduces the fundamental concepts needed to understand the work presented in the following chapters. Firstly, a general introduction into spin transport is given including the (inverse) spin Hall effect, which is the most important feature for the interconversion of charge currents and pure spin-currents by using Pt as metallic

electrode. Further, two main spintronic effects presented in this thesis are introduced: SSE and SMR. Thereafter, important material properties of different magnetic insulators are discussed, followed by the Dzyaloshinskii-Moriya interaction, which can be used to describe the magnetization behavior in chiral magnetic insulators. Moreover, we briefly introduce the low-dimensional antiferromagnets with the ongoing discussion about the possibility of their use in spintronic devices. The final part of this chapter is based on the device fabrication and measurement methods which are used for the experiments presented in this thesis.

- *Chapter 3* shows the investigation of the SSE in a single crystal Yttrium iron garnet (YIG)|Pt bilayer system. By using the inverse spin Hall effect, the spin currents carried by magnons in a magnetic insulator can be electrically detected. Here, the magnons are excited by creating a thermal gradient with an external heater on top of Pt. Magnetic field dependence of the SSE is measured at room temperature for several devices prepared with different mechanical treatment conditions for YIG surface, showing a strong dependence of the signal on the interface condition of the Pt|YIG bilayer system.

- *Chapter 4* manifests the SMR and SSE in a non-collinear magnetic insulator $CoCr_2O_4$|Pt device and shows their behavior in different magnetic states of $CoCr_2O_4$ (CCO). We were the first group to experimentally demonstrate these effects in a non-collinear spiral magnetic insulator. Both effects were simultaneously detected at different temperatures (5 K - 300 K), in different applied magnetic fields (0 T - 7 T). Finally, also a comparison has been made between CCO|Pt and YIG |Pt systems, showing a large influence on the measured SMR and SSE signals, depending on the magnetic order of the magnetic insulator.

- *Chapter 5* continues on the investigation of the SMR and SSE in a non-collinear magnetic insulator, focusing on a magnetic system without inversion center Cu_2OSeO_3 (CSO). Angular dependence of these effects has been measured in a single crystal CSO|Pt bilayer device, in different magnetic fields ($B \leq 8$ T) and temperatures ($T \leq 70$ K). By this work it has been shown for the first time that the SMR and SSE are not only sensitive to the magnetization direction but also locally sensitive to the angles of magnetic moment constructing nanomagnetic spin structures; depending on the angle of these helical spirals, the SMR signal changes from positive to negative values. Furthermore, theoretical simulations have been shown indicating a good qualitative agreement with the experimental observations.

- *Chapter 6* presents a study of the depth dependence of the current-induced magnetic fields including the Oersted and dipolar fields in a thin-film YIG|Au device, by using low energy muon spectroscopy (LEμSR). The measurements are done at different muon implantation energies, allowing us to probe muons at different depths from the YIG|Au interface. Furthermore, a model to quantify the dipolar field close to the interface is presented. Finally, the limits on the spatial resolution and the sensitivity of LEμSR are discussed to provide guidance for a future experiment designed to probe spin Hall effects with muons.

- *Chapter 7* describes the method used to grow single crystals of CSO used for the SMR and SSE study presented in Chapter 5. Furthermore, the single crystal x-ray diffraction analysis is provided including the analysis of the absolute structures for both enantiomers of CSO. Finally, the ferromagnetic resonance data with presence of higher harmonic modes is shown, confirming the excellent quality of grown single crystals.

Bibliography

[1] M. N. Baibich, J. M. Broto, A. Fert, F. N. Van Dau, F. Petroff, P. Etienne, G. Creuzet, A. Friederich, and J. Chazelas, "Giant Magnetoresistance of (001)Fe/(001)Cr Magnetic Superlattices," *Physical Review Letters* **61**, pp. 2472–2475, Nov 1988.

[2] G. Binasch, P. Grünberg, F. Saurenbach, and W. Zinn, "Enhanced magnetoresistance in layered magnetic structures with antiferromagnetic interlayer exchange," *Physical Review B* **39**, pp. 4828–4830, Mar 1989.

[3] A. Brataas, A. D. Kent, and H. Ohno, "Current-induced torques in magnetic materials," *Nature Materials* **11**, pp. 372–381, 2012.

[4] D. Ralph and M. Stiles, "Spin transfer torques," *Journal of Magnetism and Magnetic Materials* **320**(7), pp. 1190 – 1216, 2008.

[5] Y. Tserkovnyak, A. Brataas, and G. E. W. Bauer, "Enhanced Gilbert Damping in Thin Ferromagnetic Films," *Physical Review Letters* **88**, p. 117601, Feb 2002.

[6] Y. Tserkovnyak, A. Brataas, and G. E. W. Bauer, "Spin pumping and magnetization dynamics in metallic multilayers," *Physical Review B* **66**, p. 224403, Dec 2002.

[7] A. Slachter, F. L. Bakker, J.-P. Adam, and B. J. van Wees, "Thermally driven spin injection from a ferromagnet into a non-magnetic metal," *Nature Physics* **6**, pp. 879 – 882, 2010.

[8] K. Uchida, S. Takahashi, K. Harii, J. Ieda, W. Koshibae, K. Ando, S. Maekawa, and E. Saitoh, "Observation of the spin Seebeck effect," *Nature* **455**, pp. 778–781, Oct. 2008.

[9] G. E. W. Bauer, E. Saitoh, and B. J. van Wees, "Spin caloritronics," *Nature Materials* **11**, pp. 391–399, Apr. 2012.

[10] R. A. Duine, A. Brataas, S. A. Bender, and Y. Tserkovnyak, "Spintronics and Magnon Bose-Einstein Condensation," *ArXiv e-prints, arXiv:1505.01329* , 2015.

[11] A. V. Chumak, V. I. Vasyuchka, A. A. Serga, and B. Hillebrands, "Magnon spintronics," *Nature Physics* **11**, pp. 453–461, 2015.

[12] K. Uchida, J. Xiao, H. Adachi, J. Ohe, S. Takahashi, J. Ieda, T. Ota, Y. Kajiwara, H. Umezawa, H. Kawai, G. E. W. Bauer, S. Maekawa, and E. Saitoh, "Spin Seebeck insulator," *Nature Materials* **9**, p. 894, 2010.

[13] Y. Kajiwara, K. Harii, S. Takahashi, J. Ohe, K. Uchida, M. Mizuguchi, H. Umezawa, H. Kawai, K. Ando, K. Takanashi, S. Maekawa, and E. Saitoh, "Transmission of electrical signals by spin-wave interconversion in a magnetic insulator," *Nature* **464**, p. 262, Mar 2010.

1

Chapter 2

Concepts of spin transport in metal|magnetic insulator heterostructures

Abstract

In this chapter the basic physical concepts needed to understand the work presented in the upcoming chapters on spin transport in magnetic insulators are explained. Spin transport mechanisms including the spin Hall magnetoresistance are discussed. Thereafter, the concepts of the spin-mixing conductance, which is important to define the quality of interface, and the spin Seebeck effect are discussed. A variety of novel magnetic insulators are discussed which can be used to investigate the spin transport. Next, the fabrication and measurement techniques, used to perform the spin transport experiments presented in this thesis, are introduced. The fabrication part includes detailed information about different steps used for patterning device structures with electron-beam lithography followed by sputtering. The measurement techniques part includes the working principle of lock-in detection used to measure the electrical signals and a detailed scheme of the measurement setup used for this work.

2.1 Spin transport in normal metal|magnetic insulator heterostructures

Spintronics (electronics with the electron's spin) is a rapidly growing research area with a huge potential to overcome the problems of the continuous miniaturization faced by silicon-based electronics. One of the famous applications of spintronics is in the magnetic random access memories, based on the giant magnetoresistance, where reading and writing of the data is done by exploiting the spin-polarized currents without any direct spin manipulation. However, the ongoing miniaturization of these devices is limited by the generation of Joule heating associated with a net charge flow. Therefore, pure spin currents (a flow of spin angular momentum without net charge flow) are needed for further developments.

A novel approach is to use magnetic insulators instead of metals, referred as 'magnon spintronics' [1]. The advantage of using insulators is the absence of moving charges and thus the spin information (spin current) is carried only by spin-wave excitations (magnons) [2, 3]. These spin currents in magnetic insulators can be excited thermally [4] or electrically [2]. It has been shown recently that the spin information can be transported up to tens of millimeters in magnetic insulators [5]. The most commonly used device structures consist of bilayers

of a normal metal with strong spin-orbit coupling and a ferromagnetic insulator. In these structures, by taking advantage of the large spin-orbit coupling (SOC), a NM metal is used to convert charge (spin) currents to transverse spin (charge) currents by the (inverse) spin Hall effect. By using this bilayer device configuration, it has been shown recently that magnons can be excited and detected fully electrically carrying a spin information that can be transported over macroscopic distances through a magnetic insulator, by diffusion of non-equilibrium magnons [3]. The experimentally observed length scales over which the spin information can be transported are shown to be at least 40 μm, with an effective magnon spin diffusion length around 10 μm [3].

2.2 Pure spin currents

In the spintronic devices consisting of multilayers of ferromagnetic and non-magnetic metals, the spin-dependent electrical transport is often described by the two spin channel model [6]. In this model, where magnetization is considered to be collinear, the electrical transport of majority and minority spins (often named as spin-up and spin-down, respectively) are treated independently. Therefore, the electric charge current density J_c can be written as sum of spin-up ($J_\uparrow$) and spin-down ($J_\downarrow$) charge current densities propagating in same direction,

$$J_c = J_\uparrow + J_\downarrow, \tag{2.1}$$

whereas, the spin current J_s is defined as the difference of spin-up and spin-down charge current densities as follows:

$$J_s = \frac{\hbar/2}{e} J_\uparrow + \frac{-\hbar/2}{e} J_\downarrow = \frac{\hbar}{2e}(J_\uparrow - J_\downarrow), \tag{2.2}$$

Here, $J_\uparrow$ is defined as positive spin current. The prefactor $\hbar/2e$, used here and sometimes in literature, reflects the fact that $J_\uparrow$ and $J_\downarrow$ are considered as the flow of charge carriers, whereas J_s is defined as a flow of angular momentum.

Using Eqs. 2.1 and 2.2 we can distinguish three different scenarios, as is schematically shown in Fig. 2.1:

1. pure charge currents: when both spin-up and spin-down current densities are equal and propagate in same direction, the situation corresponds to a net charge current flow without any flow of angular momentum and can be defined as pure charge current. The situation is valid for paramagnetic metals with negligible spin-orbit coupling.
2. spin-polarized currents: when $J_\uparrow \neq J_\downarrow$, both charge and spin information are transported through the material and the current is called spin-polarized. The situation can be observed in ferromagnetic metals.
3. pure spin currents: when both spin-up and spin-down current densities are equal and propagate in opposite directions. It leads to the flow of angular momentum alone without flow of net charge current. This flow of angular momentum is known as a pure spin current.

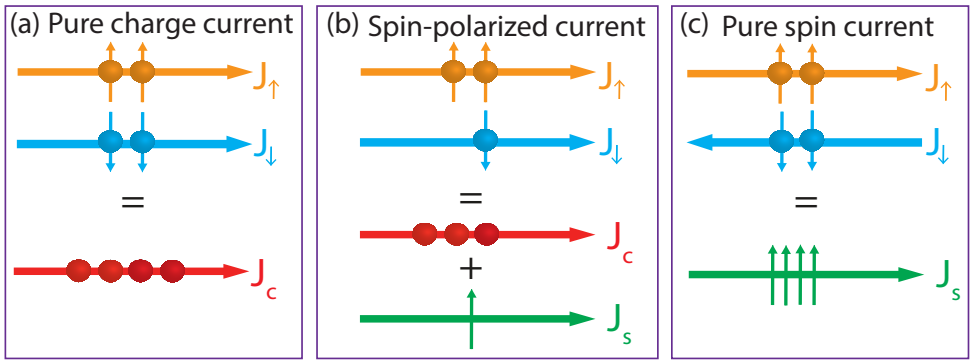

Figure 2.1: *Three different types of currents. (a) Pure charge current in which an equal number of spin-up and spin-down electrons propagate in the same direction with current densities $J_\uparrow$ and $J_\downarrow$, respectively. This results in the propagation of a pure charge current without any net flow of angular momentum. (b) When $J_\uparrow$ and $J_\downarrow$ propagate in the same direction with different number of spin-up and spin-down electrons, this leads to a transport of both, spin and charge represented as J_c and J_s, respectively. This situation represents the propagation of a spin-polarized current. (c) Assuming a situation where the number of spin-up and spin-down electrons are equal but propagate in opposite directions. This situation leads to the flow of a pure spin current in which a net transport of spin alone occurs, without any net charge current contribution. Figure adapted from Ref. [7].*

In magnetic insulators having no free electrons, a spin current J_s is carried by quasiparticles known as magnons. Magnons can be excited in a magnetically ordered material by the collective precessional motion of electronic spins. The ground state of a ferromagnetic insulator can be imagined as all the "net" spins being aligned parallel to the applied field direction, as shown in Fig. 2.2(a). The excited state of this magnetic system would then be obtained by flipping one spin, as shown in Fig. 2.2(b). However, due to strong exchange interactions, the excited state obtained by flipping the spin is not energetically favorable and the net spin reduction is distributed over the whole systems, resulting in a collective spin-wave excitation, as shown in Fig. 2.2(c). These collective spin-wave excitations (known as magnons) carry J_s with spin-polarization along the average magnetization direction of the magnetic material.

When a ferromagnetic metal (F) is connected with a non-magnetic metal (NM) and a charge current is sent through this F|NM bilayer system, in the bulk of the magnet F, the current is spin-polarized ($J_\uparrow \neq J_\downarrow$), whereas in the bulk of NM material the current is unpolarized ($J_\uparrow = J_\downarrow$). The conversion from spin-polarized to unpolarized charge current happens at the F|NM interface via spin relaxation which results into a spin-accumulation at the interface. The spin accumulation is $\mu_s = \mu_\uparrow - \mu_\downarrow$, where $\mu_\uparrow$ and $\mu_\downarrow$ are the chemical potentials for spin-up and spin-down electrons. μ_s decays exponentially with the distance away from the interface and can be described by using the Valet-Fret equation from spin diffusion [6]:

$$\nabla^2 \mu_s = \frac{\mu_s}{\lambda^2}, \tag{2.3}$$

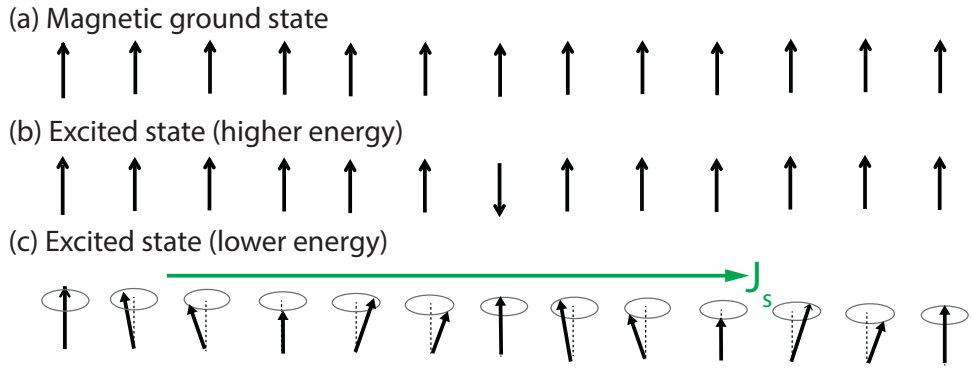

Figure 2.2: *A simple illustration of a ferromagnet. (a) Ground state: All spins are aligned. (b) Excited state: one spin is flipped, (c) to minimize the energy, the net spin reduction is distributed over the whole system by a collective rotation (precession) of all spins around their equilibrium, resulting a magnon carrying a spin current J_s.*

where λ represents the spin relaxation length of the material. Like in fully metallic systems, in the magnetic insulator|non-magnetic metal systems, a spin accumulation can also be created. In these not fully metallic systems, the spin accumulation can be created at the interface. The spin accumulations in these systems also diffuse and relax in the non-magnetic metal. The spin accumulations can be electrically generated by the spin Hall effect and detected by the inverse spin Hall effect (both effects are discussed in detail in section 2.3 below.)

2.3 Generation (detection) of spin currents by (inverse) spin Hall effect

As discussed above, pure charge currents can be found in paramagnetic metals, but the prediction of generation of pure spin currents in a paramagnetic metal by the spin Hall effect started a new paradigm for spintronics. The SHE is in analogy with the ordinary Hall effect in which a voltage difference is generated transverse to the electric current in a metal when a magnetic field is applied. However, the SHE is a purely spin-based phenomenon which is conceptually more related to the anomalous Hall effect (AHE). In AHE, the relativistic spin-orbit interaction generates an asymmetric deflection of the charge carriers depending on their spin direction [8] in a ferromagnetic metal. Like the AHE, the SHE is also caused by spin-orbit interaction and can be observed in heavy paramagnetic metals with strong spin-orbit interaction - an interaction of a particle with its motion. The idea of the SHE was predicted firstly by Dyakonov and Perel in 1971 [9] and rediscovered later by Hirsch in 1999 [10]. Almost 30 years later after its prediction the SHE was experimentally observed [11].

In the SHE, an electrical current J_c is sent through a metal with strong spin-orbit interaction. This interaction leads to an asymmetric scattering of spin-up and spin-down electrons,

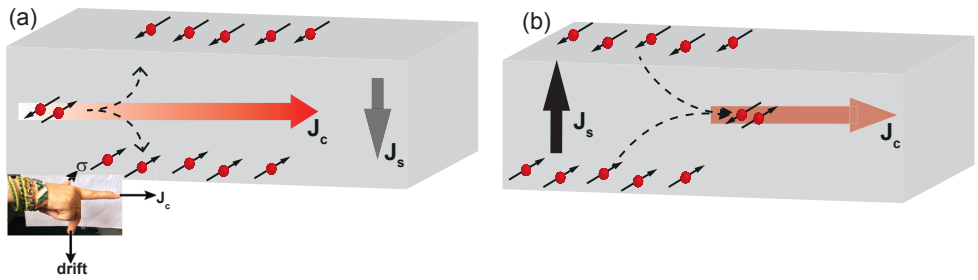

Figure 2.3: *(a) Schematic illustration of the spin Hall effect, where an initial charge current $\boldsymbol{J}_c$ results in a transverse spin current $\boldsymbol{J}_s$. The electrons moving initially along the index finger direction with a spin-polarization $\boldsymbol{\sigma}$ pointing along the thumb direction drift towards the direction of middle finger, leading to a spin accumulation at the interface. The situation of the right-hand rule is defined here for a metal like Pt with a positive spin Hall angle, however for a metal like Ta with a negative spin Hall angle the drift direction will be opposite [22]. (b) Illustration of the inverse spin Hall effect, where an injected spin current $\boldsymbol{J}_s$ generates a charge current $\boldsymbol{J}_c$.*

resulting in a net spin current J_s transverse to the charge current direction [11–13], as shown in Fig. 2.3(a). The reciprocal effect known as the inverse spin Hall effect is based on the same principle: the initial pure spin current results in a transverse charge current due to spin-orbit coupling (Fig. 2.3(b)). As explained above, the efficiency of the charge to spin current interconversion depends on the spin-orbit interaction and, therefore, it is specific for each material and parametrized by a dimensionless quantity known as spin Hall angle θ_{SH} [14]. The magnitude and sign of the generated spin current are defined as follows:

$$\vec{J}_s = \theta_{\mathrm{SH}} \vec{\sigma} \times \vec{J}_c, \tag{2.4}$$

$$\vec{J}_c = \theta_{\mathrm{SH}} \vec{\sigma} \times \vec{J}_s, \tag{2.5}$$

where $\vec{\sigma}$ represents the spin-polarization direction. The scattering mechanisms resulting in the SHE in paramagnetic metals or in the AHE in ferromagnetic metals are divided into extrinsic mechanisms, named skew scattering [15] and side-jump scattering [16] and intrinsic effects [8, 17, 18], which are related to the electronics band structure of the metal itself [19]. It has been reported that for 4d and 5d transition metals (e.g. Pt and Ta) intrinsic scattering mechanisms dominate over the extrinsic ones [20, 21].

Among the several possibilities to create spin currents, the SHE has gained a distinct place in the field of magnon spintronics, since its first observation a decade ago [11, 12] together with its reciprocal effect, the ISHE. Moreover, the interplay of both phenomena, SHE and ISHE, forms the basis for the spin Hall magnetoresistance discussed in section 2.4. Considering the extensive focus of current research, recently, several groups have combined their research efforts and suggested a right-hand rule to define the positive spin Hall angle (see Fig. 2.3) [22], for consistency of future work.

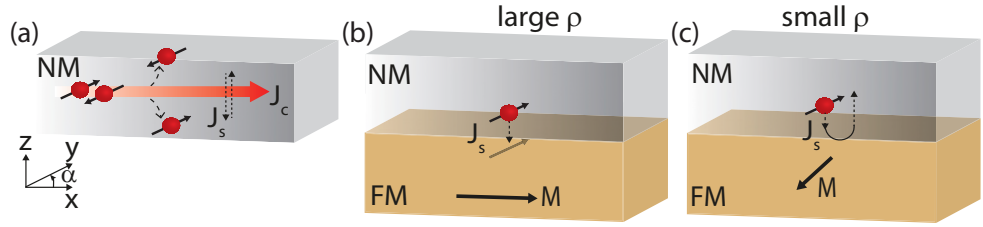

Figure 2.4: *(a) Schematic illustration of the three main steps constituting the SMR in a FM|NM system. (a) Creation of the spin accumulation: A charge current sent through the NM creates a spin current by SHE resulting in the spin accumulation at the FM|NM interface. (b) Interaction between the itinerant spins in the NM and localized spins in the insulating FM: the spin-polarized electrons lose angular momentum when it is perpendicular to M by the spin-transfer torque effect, resulting in a spin current injected into the FM. (c) The spins arriving at the interface are fully reflected back in a NM when parallel to M resulting in an additional charge current by ISHE.*

2.4 Spin Hall magnetoresistance

The spin Hall magnetoresistance (SMR) is a spin current driven magnetoresistance effect. The effect originates from the transport of spin current across a magnetic insulator|metal interface. The metal, such as Pt, has strong spin-orbit coupling resulting a finite spin Hall angle.

The SMR was discovered in 2012 in a prototype ferrimagnetic insulator YIG|Pt system, both in our group [23, 24] and by Nakayama *et al*. [25]. Its origin was theoretically explained by Chen *et al*. in 2013 [26]. In the same year the SMR was reported in the YIG|Pt [27, 28] and YIG|Ta [29] systems by several other groups. Recently the SMR has been reported in more complex systems like $CoFe_2O_4$|Pt [30] and by our group in $CoCr_2O_4$|Pt (Chapter 4) and Cu_2OSeO_3|Pt (Chapter 5).

In the SMR both SHE and the ISHE act in a concerted manner. When an in-plane current flows through a resistive NM bar with strong spin-obit coupling, electrons with spins of opposite polarities accumulate at the opposite surfaces of the bar by the SHE, as shown in Fig. 2.4(a). In the plain NM bar, this spin accumulation is not visible because it will be followed by a spin current back flow in NM. Both spin currents have the same spin orientation and propagate in opposite directions, resulting in zero net contribution from the spin current to the electrical resistance (Fig. 2.4(a)).

When a NM metal is in close vicinity of a FM layer, the interplay of SHE and ISHE becomes visible due to the spin-torque effect (discussed in section 2.5). The spin accumulation due to SHE at the FM|NM interface can be partially absorbed or fully reflected, depending on the interface magnetization $\vec{M}$ of the FM. When $\boldsymbol{\mu}_s \perp \boldsymbol{M}$, the electron spins arriving at the Pt|CSO interface are partially absorbed (see Fig. 2.4(b)), thereby increasing the resistance. When $\boldsymbol{\mu}_s \parallel \boldsymbol{M}$, spins will be fully reflected. The reflected spin currents generate an extra charge current via the ISHE (see Fig. 2.4(c)), thereby reducing the resistance. Therefore by rotating the magnetization of FM, a change in the resistance of NM due to SMR can be mea-

sured. In a planar Hall-bar geometry of a NM contact, the change in the resistance by the SMR can be measured not only along the current (longitudinal) direction but also transverse to the applied current direction. When $\boldsymbol{M}$ makes an angle with $\boldsymbol{\mu}_s$, this additionally generated charge current also has a component pointing in the transverse direction resulting in a change in the transverse resistance. This change in the transverse resistance has a maximum modulation between two configurations for $\alpha = 45^{\text{o}}$ or 135^{o} - known as the transverse SMR response. In contrast, the longitudinal resistance establishes the maximum modulation between two configurations for $\alpha = 0^{\text{o}}$ or 90^{o}. In this thesis, we focused on the transverse SMR response. The SMR signal in the longitudinal and transverse configurations can be described as follows:

$$\rho_{\text{trans}} = \Delta\rho_1 m_x m_y + \Delta\rho_2 m_z, \tag{2.6}$$

$$\rho_{\text{long}} = \rho + \Delta\rho_0 + \Delta\rho_1(1 - m_y^2), \tag{2.7}$$

here ρ_{trans} and ρ_{long} represent the transverse and the longitudinal resistivity, respectively. ρ is the electrical resistivity of NM. m_x, m_y, m_z are the components of the magnetization of FM in the $\hat{x}$, $\hat{y}$, and $\hat{z}$ directions, respectively. $\Delta\rho_0$, $\Delta\rho_1$ and $\Delta\rho_2$ are different changes in the resistivity defined as follows [26]:

$$\frac{\Delta\rho_0}{\rho} = -\theta_{\text{SH}}^2 \frac{2\lambda}{t} \tanh\frac{t}{2\lambda}, \tag{2.8}$$

$$\frac{\Delta\rho_1}{\rho} = \theta_{SH}^2 \frac{\lambda}{t} \text{Re}\left(\frac{2\lambda G_{\uparrow\downarrow} \tanh^2 \frac{t}{2\lambda}}{\sigma + 2\lambda G_{\uparrow\downarrow} \coth \frac{t}{\lambda}}\right), \tag{2.9}$$

$$\frac{\Delta\rho_2}{\rho} = -\theta_{SH}^2 \frac{\lambda}{t} \text{Im}\left(\frac{2\lambda G_{\uparrow\downarrow} \tanh^2 \frac{t}{2\lambda}}{\sigma + 2\lambda G_{\uparrow\downarrow} \coth \frac{t}{\lambda}}\right). \tag{2.10}$$

Here λ, t, θ_{SH}, σ, and $G_{\uparrow\downarrow}$ represent the spin relaxation length, thickness, spin Hall angle, bulk conductivity of the NM layer and the spin mixing conductance of the FM|NM interface, respectively. Note that for out-of-plane magnetic field configurations the ordinary Hall effect will be also taken into account in Eq. 2.6 [31].

Till now the SMR is considered as an interface effect [26, 30, 32] and can be used to determine the magnetization direction of the magnetic layer, without the need to send the charge current through this magnetic layer itself. The magnitude of the spin transfer torque, STT and therefore, the SMR depends on the quality of the FM|NM interface, described by the spin-mixing conductance. A higher spin-mixing conductance results in a large STT resulting in more absorption of the spin current at the interface (when $\boldsymbol{\mu}_s \perp \boldsymbol{M}$) and therefore a larger change in the NM resistance - a higher SMR signal. The spin-mixing conductance is explained in detail in section 2.5.

2.5 Spin-mixing conductance at the insulator|metal interface

Both for the SMR and SSE (discussed in the next section), the interaction between the spins of the itinerant electrons in a metallic layer NM and the localized moments in a magnetic

layer FM is essential. This interaction is parametrized by the spin-mixing conductance at the interface defined as $G_{\uparrow\downarrow} = G_r + iG_i$, where G_r and G_i represent its real and imaginary parts. The magnitude of $G_{\uparrow\downarrow}$ is observed to be very sensitive to the interface quality. It describes the transfer of angular momentum across the interface; a higher $G_{\uparrow\downarrow}$ means more spins can be injected from the NM to the FM layer which results in a higher spin transfer torque [26, 33]:

$$\boldsymbol{\tau}_{\mathrm{STT}} = G_r \boldsymbol{m} \times \boldsymbol{\mu_s} \times \boldsymbol{m} + G_i \boldsymbol{\mu_i} \times \boldsymbol{m}, \tag{2.11}$$

where $\boldsymbol{\tau}_{\mathrm{STT}}$ is the spin transfer torque acting on FM, $\boldsymbol{m} = (m_i, m_j, m_k)^{\mathrm{T}}$ is the normalized unit vector of the magnetization direction and μ_s is the spin accumulation at the FM|NM interface with a specific spin-polarization direction [7, 31]. The real part G_r of the spin mixing conductance is linked to the in-plane magnetic field torque [34, 35] and is accessible from experiments like spin pumping [2, 36–38]. The imaginary part G_i is related to the spin precession and interpreted as an effective field acting on the magnetization, and is therefore also referred as *effective field* torque and thus can be either positive or negative [39]. The SMR allows to quantify both G_r and G_i experimentally in FM|NM heterostructures. From Eqs. (2.6) and (2.10) it can be seen that by tuning the magnetization of FM layer (in such a way that the product $m_x m_y$ vanishes), the imaginary part G_i can be exclusively detected. It has been observed that G_i is almost an order of magnitude smaller than G_r [39], as shown in a YIG|Pt system with $G_r = (7 \pm 3) \times 10^{14} \Omega^{-1} m^{-2}$ and $G_i = (5 \pm 3) \times 10^{13} \Omega^{-1} m^{-2}$ [24]. Therefore, in most experiments only G_r is taken into account.

2.6 Spin-caloritronic effect: spin Seebeck effect

Recovery of waste heat as electricity is traditionally the main concern of thermoelectricity, and thermoelectric materials are the only option for harvesting relatively small temperature gradients, where most of the energy wasted as heat is available [40]. Conventional thermoelectrics occur via the Seebeck effect which turns a temperature difference into a voltage. However, the spin Seebeck effect is a new approach discovered in 2008 [41] - the spin analogy of the Seebeck effect. The conventional Seebeck effect, discovered in 1821, generates an electric voltage $\vec{\Delta} V$ as a result of a temperature gradient $\vec{\nabla} T$ in a conductor, which can drive an electric current in a closed circuit, along $\vec{\nabla} T$ [42]. The voltage that builds up due to this effect is gauged by the Seebeck coefficient $S = \frac{\vec{\Delta} V}{\vec{\nabla} T}$. The origin of the Seebeck effect is that the electrons' conductivity is energy dependent. When a conductor is heated from one side, the electrons on the hot side are more energetic and therefore have greater velocities than those in the cold side of the conductor. Due to this difference in the energies of electrons at different sides, a net diffusion of electrons occurs from hot end towards the cold end. This diffusion causes a charge imbalance between two sides, resulting in a voltage build-up between two ends [43]. The widely used thermocouples are based on the principle of the Seebeck effect.

Unlike the conventional thermoelectric effect (e.g. Seebeck effect) where the charge of electrons couples to the heat, the field of spin caloritronics focuses on the study of mechanisms based on coupling of electronic spin with heat. There are several mechanisms recently discovered in the field of spin caloritronics including the spin Seebeck (SSE) and spin-dependent

Seebeck (SdSE) effects which involve the generation of spin currents by applying a thermal gradient. In both effects, the FM|NM bilayer heterostructures are utilized to generate and detect spin currents. Although the SSE is very different from the SdSE that is driven by the spins of itinerant (or tunnelling) electrons, and it results in a change in the charge Seebeck coefficient by changing the magnetization configuration [44, 45].

A bulk ferromagnetic metal fundamentally acts as a thermocouple in which two parallel spin-channels, with spin-dependent Seebeck coefficients, act as its two legs. When a temperature gradient is applied across this ferromagnet, under a closed circuit condition, the classical thermoelectric effect causes a charge current to circulate though this metal parallel to the thermal gradient. As the thermopower of this ferromagnetic metal is spin-dependent, the charge current will be accompanied by a spin current. The SdSE cannot be observed in insulators as it requires the presence of conduction electrons. In contrast to SdSE, which can occur in a bulk ferromagnetic metal, the SSE is a two-step process that requires an interface between a magnetic insulator (FM) and a normal metal (NM). In the first step of the SSE, a pure spin current is generated by exciting magnons with an applied thermal gradient across a magnetic insulator. In the second step of the SSE, the spin current is injected across the NM|FM interface into the NM contact. The injected spin current is measured as an-open circuit voltage in NM by the ISHE. Hence, the SSE utilizes the collective spin degree of freedom of a magnetic insulator as a route to new physical phenomena that convert waste heat into useful spin currents that flow with minimal dissipation.

In a magnetic insulator at a finite temperature the spins are not statically aligned along the average magnetization direction but due to thermal excitation they are randomly rotated. When a thermal gradient is applied across this insulator, it leads to stronger thermal excitations on the hot side compared to the cold side. This difference in the spin excitation on both ends excites magnons which can transport spin along the temperature gradient direction. These thermally excited magnons can be detected electrically in the SSE. These magnons carry a spin current which can be transferred at the interface into a normal metal NM. The adjacent NM will act as a sink for magnons, resulting in a pure spin current injection into the NM. The spin-polarization direction of the injected spin current depends on the direction of thermal gradient, reversing the thermal gradient direction will also invert the sign of the spin-polarization. This spin current is detected electrically by the ISHE (explained in section 2.3).

In the beginning, only metallic FM|NM bilayers were used to study the SdSE. However, recently after the discovery of the SSE, the insulating FM have attracted much attention. These FM systems, like the yttrium iron garnet (YIG), with a long-range magnetic order, enable the propagation of magnetic excitations carrying spin currents, but at the same time are electrically insulating. Therefore, the insulating FM|NM heterostructure provides a clean separation of spin and charge currents, as the charge currents are restricted to the conductive NM layer, while the spin currents can propagate in both insulating FM and NM layers. The large potential for applications of magnon spintronics is illustrated by the spin Seebeck effect which already has some distinct advantages over the ordinary Seebeck effect, owing to the ease of device fabrication, scalability, and efficiency near room temperature. This is demonstrated, for example, in the device-concept of spin-thermoelectric coating [40, 46].

The SSE is till now explained as a bulk effect in which thermal magnons play an important

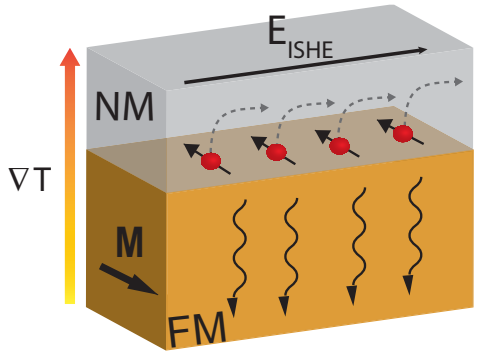

Figure 2.5: *(a) Illustration of the spin Seebeck effect in a ferromagnetic insulator - normal metal (FM|NM) system, where a thermal gradient* ΔT *excites thermal magnons in FM. These magnons will transfer the angular momentum at the interface by polarizing the electrons in a NM close to the interface. These spin-polarized electrons will be detected electrically by the inverse spin Hall effect in a NM.*

role [47–49]. The microscopic origin of the SSE was theoretically explained firstly by Xiao *et al* [50]. Using earlier work by Sanders and Walton [51], they explained that in SSE the injected spin current in the adjacent NM by thermal spin pumping is caused by the difference in temperature at the FM|NM interface between the magnons in FM and electrons in the NM contact. In their theoretical model they assumed the electron-temperature being equal to the phonon-temperature, obtaining $J_s \propto \Delta T_{me}$, where J_s is the injected spin current density into a NM and ΔT_{me} is the temperature difference between the magnons and electrons at the FM|NM interface. Later on, Hoffman *et al*. reformulated the theory of Xiao *et al*. by considering the Landau-Lifshitz-Gilbert equation. However, recent experiments by Kehlberger *et al*. [48] show that the theoretical interpretation of the SSE by Xiao et al. is not sufficient to explain their observed SSE signal as a function of YIG thickness in a YIG|Pt system. Moreover, non-local SSE signals observed recently by Cornelissen *et al*. also cannot be explained by this theory. To explain their work, a different theoretical interpretation of the SSE proposed by Rezende *et al*. [52] was used. According to this theoretical model, the SSE results from the bulk magnon spin currents created by the temperature gradient across the thickness of the ferromagnetic insulator. Further research is still going on to find the possible coexistence of the interface as well as bulk effect [53].

2.7 Magnetic insulators

Spintronics in magnetic insulators, like the yttrium iron garnet (YIG) with a long-range magnetic order, enable the propagation of magnetic excitations carrying the spin currents. At the same time, they are electrically insulating, providing a clean separation of spin and charge currents, as the charge currents are restricted to the conductive metallic electrodes. Many spintronic phenomena have already been demonstrated in magnetic insulators including the spin Hall magnetoresistance (SMR) [23, 24, 54], spin Seebeck effect (SSE) [4, 41, 55], spin-Peltier effect [56], spin-pumping [57, 58] and spin-transfer torque [1, 59, 60].

These effects have been investigated mostly in the prototype YIG which is a room-temperature magnetic insulator with low magnetic damping [61]. However, magnetic insulators come in a large variety of magnetic order which can offer improved efficiency and new functionality for

spin transport. As recently reported by Kirihara *et al.* [40], the efficiency of a thermoelectric device based on the SSE can be ten times improved compared to a conventional thermoelectric by making use of $Ni_{0.2}Zn_{0.3}Fe2.5O_4$ magnetic layers coated on a flexible plastic sheet. A spray-coating method known as 'ferrite plating' is used offering favorable features for thermoelectric applications.

The potential of new magnetic materials became more clearer after the discovery of a sign change as a function of magnetic field in the SSE signal observed in a Gd iron garnet (GIG) [62]. This shows that an unexpected behavior that leads to novel functionality may be found by considering new magnetic materials. Apart from garnets, the frustrated non-collinear and chiral magnetic insulators can be interesting for spin transport study due to their enriched magnetic phase diagrams [63–65].

2.7.1 Non-collinear magnetic insulators

In non-collinear frustrated magnets, the second nearest neighbor magnetic interactions are of the same order as those for the first one, generating geometric frustration that favors spin canting. This spin canting leads to various spin-spiral orders, like proper screw, cycloidal, longitudinal-conical and transverse-conical spiral. An example of such a non-collinear frustrated magnet is $CoCr_2O_4$ (CCO), discussed in chapter 4.

To understand frustrated magnetism we can consider the Hamiltonian for a simple situation with a quasi-one dimensional spin chain which can be written as follows:

$$\mathcal{H} = \sum_n J_1 \boldsymbol{S}_n . \boldsymbol{S}_{n+1} + J_2 \boldsymbol{S}_n . \boldsymbol{S}_{n+2}, \tag{2.12}$$

where J_1 and J_2 are the first and second nearest neighbour interactions. The nearest neighbor interaction prefers a (anti-) ferromagnetic ground state, determined by the sign of J_1, and competes with the next nearest neighbor antiferromagnetic interaction J_2. When J_1 is sufficiently strong ($|J_1| < 4J_2$), the ground state will be collinear (anti-) ferromagnetic as in case of the prototype YIG. Otherwise, the ground state will be a spiral state $S_n = (\cos qn, \sin qn)$ with a wave vector $q = \arccos(-\frac{J_1}{4J_2})$ [66]. This mechanism is responsible for spiral ordering for materials like $CoCr_2O_4$ discussed in chapter 4.

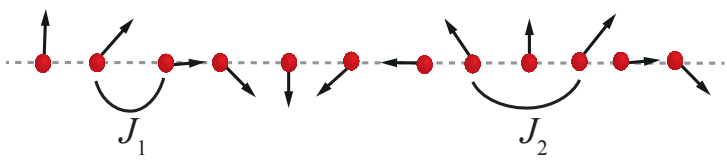

Figure 2.6: *(a) Structure illustration of magnetic spiral ordering in the chain of the quasi-1D magnet with J_1 and J_2 the first and second nearest neighbor interactions, respectively.*

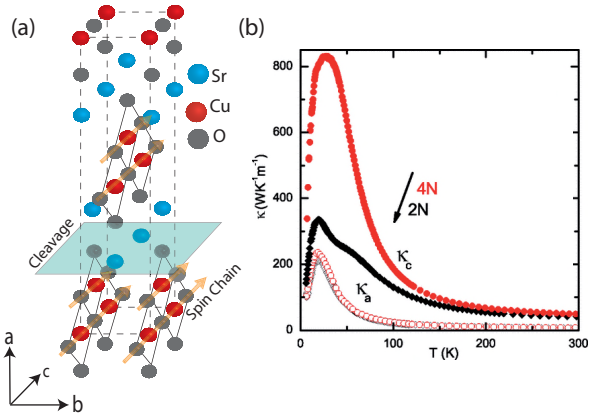

Figure 2.7: *(a) Structure of the spin-chain compound* $SrCuO_2$. *(b) adapted from Ref. [71], shows the thermal conductivities,* κ_a *and* κ_c *of* $SrCuO_2$ *along a and c axes, respectively. Closed (open) symbols represent c-axis (a-axis) data, circles (diamonds) corresponding to samples with different purity, 4N (2N).*

2.7.2 Non-centrosymmetric magnetic insulators

The non-centrosymmetric magnetic systems with no inversion center are of a great interest due to presence of variety of non-collinear spin states including spiral, helical and skyrmionic magnetic states. In these magnetic systems the relativistic Dzyaloshinskii-Moriya (DM) interaction plays an important role. The DM interaction is an antisymmetric exchange which favors a spin canting of otherwise (anti)parallel aligned magnetic moments and its strength is proportional to the spin-orbit coupling constant. This DM interaction result in a twist of the initially ferromagnetic spin arrangement, leading to the formation of non-collinear incommensurate (chiral) helical structures [67–70]. The most famous example of such a magnetic insulator Cu_2OSeO_3, the first magnetic insulator in which the skyrmion lattice phase is observed, discussed in chapters 5 and 7.

2.7.3 Low-dimensional magnetic systems

Apart from three-dimensional magnets, the quasi-one-dimensional magnetic insulators such as $SrCuO_2$, Sr_2CuO_3 and $(Sr,Ca,La)_{14}Cu_{24}O_4$ can be potential candidates to improve the efficiency of spin caloritronic effects like SSE. The magnonic spin-heat currents can be orders of magnitude larger in these low-dimensional systems compared to that in three-dimensional bulk materials due to the fact that the low dimensionality suppresses decay channels by limiting the scattering phase space. Moreover, the crystal anisotropy of the heat conductivity in these materials can be used to tune the phononic contribution to the heat flow with respect to the magnonic contribution. An example of such a system is $SrCuO_2$, which is a layered material. Each layer is separated by non-magnetic strontium atoms and the magnonic heat transport can only occur in the ac-plane containing Cu-O-Cu spin-chains (see Fig. 2.7(a)). These Cu-O-Cu chains have strong superexchange interaction within the chain and almost 10 times weaker between the chains. $SrCuO_2$ crystals have shown very large anisotropy in the heat conductivity with almost ballistic heat transport along the chains, as shown in Fig. 2.7(b).

2.8 Device fabrication and measurement techniques

This section describes the techniques used to fabricate devices studied in this thesis. The devices are fabricated from crystals as well as thin films. For both films and crystals the same device fabrication procedure is used, apart from the starting step of surface preparation. The Cu_2OSeO_3 (CSO) single crystals and $CoCr_2O_4$ (CCO) are grown in our lab, the growth procedure for CSO is summarized in chapter 7. Exceptions are YIG single crystals described in chapter 3 which are not grown in our lab but are bought from Crystal Systems Corporation, Hokuto, Yamanashi, Japan. The starting point for device fabrication of crystals (CSO and YIG) is getting a reasonably flat surface along the required crystallographic plane, by first orienting the crystal by single-crystal x-ray diffraction and lapping away a part of the crystal with a diamond saw cutter. After getting a surface (approximately 4×4 mm^2), the crystals (CSO, CCO) were polished with different polishing particles (sizes down to 40 nm) to achieve minimum surface roughness (< 2 nm) in our lab. For thin films no polishing was required. Further processing steps of the devices are done in NanoLabNL clean room facility in Groningen and described in the following sections.

2.8.1 Electron-beam lithography

To pattern the device structures of the Hall-bars on different magnetic surfaces, electron beam lithography is carried out. In this technique a polymer mask is spin-coated on the sample and exposed to high-energy electrons (30 kV) in a required pattern. The exposed areas of the polymer become soluble in a solution of MIBK (4-Methyl-2-pentanone) and IPA (2-propanol) (1:3) due to breakage of polymer chains during the e-beam exposure.

The Hall-bar device patterns were defined using three e-beam lithography steps, each followed by a standard deposition and lift-off procedure described below. The first step produces a marker pattern, used to align the subsequent steps. The second step defines the Hall-bar structure, deposited by DC sputter deposition technique. The third step defines metallic leads and bonding pads also deposited by the sputtering technique.

Each e-beam lithography step consists of the following subsequent procedures (schematically shown in Fig. 2.8).

1. **Cleaning substrates**: First, all samples (crystals or films) were cleaned by submerging them in a beaker containing warm acetone (48°C) and, when required, using low-power ultrasonication. The samples were rinsed by IPA and dried by blowing nitrogen. Exceptions are the CCO films used for experiments discussed in chapter 4, which are also annealed at 200°C for $60\,\mathrm{minutes}$ in an O_2 atmosphere before further processing.
2. **Resist spinning** The positive e-beam photoresist PMMA (polymethyl methacrylate) with 950k molecular weight resins in 3 % ethyl lactate solvent is used, resulting in 0.15 μm thickness of the resist layer. The photoresist is spun on the sample at a rate of 4000 rpm for 60 seconds followed by baking on a hotplate at 180°C for 90 seconds. All magnetic substrates used in this study are insulators, therefore, a water soluble conductive polymer (aquaSave-53za) is spun on top of a PMMA layer at 6000 rpm for 120 seconds.

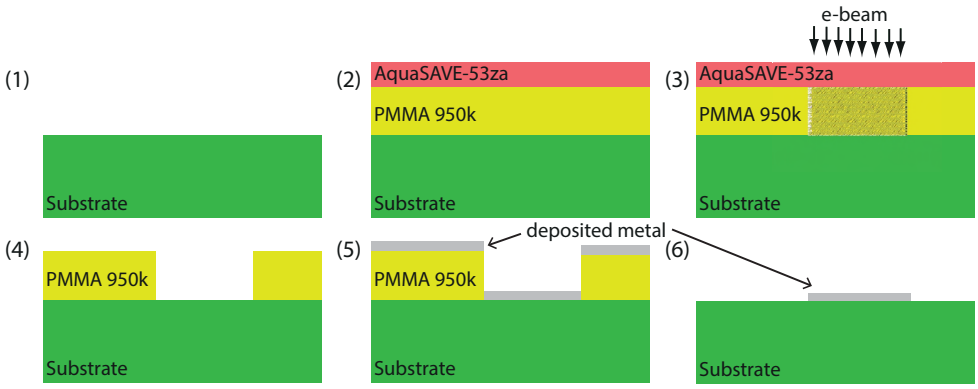

Figure 2.8: *Schematic illustration of the deposition procedure for patterning Hall-bar device structures with EBL. (1) Cleaning substrate, (2) resist spinning, (3) e-beam exposure, (4) development (5) deposition, (6) lift-off.*

3. **E-beam exposure**: The exposure is performed in a Raith e-line electron-beam system with a base pressure of $< 1 \times 10^{-5}$ mbar. The device pattern with multiple layers is drawn in the e-line software with flexibility of desired layer to be exposed. The first step of EBL, which is patterning the cross-shaped markers, is used to align the structures in the subsequent EBL steps. Area dose of $450 \mu C/cm^2$ with an acceleration voltage of 30 kV is used. A writefield of 2.4×2.4 mm^{2}combined with an aperture size of 60 μm to 120 μm is used.

   Exposure of e-beam to certain areas will break the polymer chains in that region, making it soluble in a (1:3) solution of MIBK and IPA.

4. **Development**: For developing the exposed structures, the aquaSave-53za layer is removed by rinsing the sample in deionized water for 30 seconds. Afterwards the sample is immersed in a (1:3) solution of MIBK:IPA for 30 seconds with a consecutive step of rinsing in IPA for another 30 seconds.

   By using the development procedure mentioned above, the exposed PMMA areas will be dissolved, leaving a PMMA mask with the required pattern for metallic electrode deposition. The development of the sample is checked under an optical microscope before further processing.

5. **Deposition**: The desired material is deposited on the sample with dc-sputtering in an Ar^+ plasma at an argon pressure of 3.3×10^3 mbar.

6. **Lift-off**: To remove the PPMA and unnecessary material sputtered on top, the sample is placed in a beaker containing warm acetone for 15 minutes. To assist this process, a pipette is used to stir the hot acetone and the beaker is additionally placed in an ultrasonic bath at low power when necessary.

   After deposition of all layers by following the procedure described above, the device is finalized by gluing it on a 12-pin PPMS chip carrier by using a little drop of G-varnish.

Afterwards, the contact pads on the sample are bonded to the chip carrier by AlSi wires which provide easy contacting of the device to the measurement setup. Exceptions are devices made on crystals (discussed in chapter 3 and chapter 5) where Pt wires are used to make contacts.

2.8.2 Lock-in detection

Most of the electrical measurements are performed by using the lock-in detection technique. Using this technique, the first, second or higher order responses of a system, by sending AC current through it, can be separated. Generally, any generated voltage can be expressed as the sum of first, second and higher order responses to an applied current as

$$V(t) = R_1 I(t) + R_2 I^2(t) + R_3 I^3(t) + \cdots, \tag{2.13}$$

where R_n represent the n-th order resistance response. For $I(t) = \sqrt{2} I_o \sin \omega t$, with angular frequency ω and rms value I_0, R_n are obtained by measuring the different frequency components $(1\omega, 2\omega, \cdots)$ with a lock-in amplifier, making use of the orthogonality of sinusoidal harmonic functions. To extract different frequency components, the output voltage signal from the device and the reference input signal (a sine wave function) are multiplied and integrated over time. When two signals with different frequencies are multiplied and integrated over many periods, the output will result in zero signal. However, when both sine wave functions are in-phase and have the same frequency, the output will be a nonzero signal. Therefore, the lock-in detection technique enables to separately extract different harmonic signals with reduced noise. The reduced noise in this technique is resulting from the fact that the measurement is only sensitive to a very narrow range of frequencies where the central frequency can be freely selected, giving a much better signal to noise ratio than in DC measurement techniques.

The detected n-th harmonic response at a set phase ϕ can be written as

$$V_n(t) = \frac{\sqrt{2}}{T} \int_{t-T}^{t} \sin\left(n\omega s + \phi\right) V(s) ds. \tag{2.14}$$

By solving Eq. (4.2) for an input voltage V from device, different harmonic voltage signals can be obtained which can be separately measured by the lock-in amplifiers (V_n). By considering only first and second harmonic voltage signals, the first and second order resistance responses can be defined by using Eq. (7.2) and Eq. (4.2) as follows:

$$\begin{array}{cc} V_1 = I_0 R_1 & \phi = 0^{\circ} \\ V_2 = I_0^2 R_2/\sqrt{2} \quad \text{for} & \phi = -90^{\circ} \end{array} \tag{2.15}$$

Note that V_1 (V_2) does not purely scale linearly (quadratically) with I_0 as shown in Eq. 4.3. A third (fourth) order current dependence can also be present in the measured V_1 (V_2). Nevertheless, the higher harmonic response till fourth harmonic signal is checked and observed to be negligible compared to the first and second harmonic voltage response, thus they are mostly neglected in this thesis.

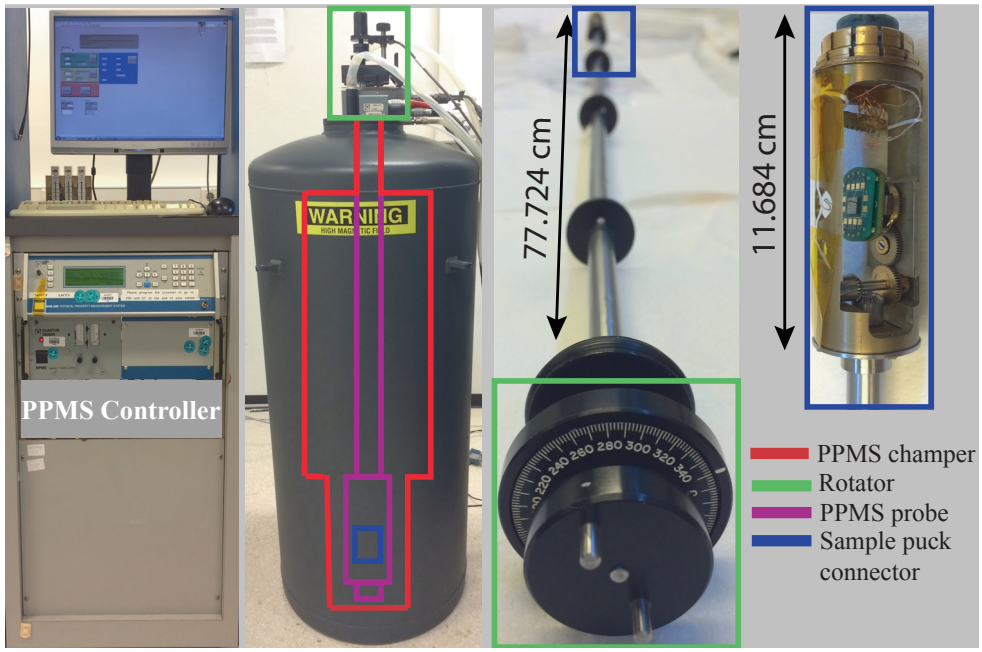

Figure 2.9: *PPMS measurement setup picture including the PPMS chamber controller, PPMS chamber and a sample stick containing a rotator.*

2.8.3 Measurement Setup

Most of the electrical measurements described in this thesis are done in the Quantum Design 'Physical Properties Measurement system' (PPMS), shown in Fig. 2.9. Exceptions are the measurements described in chapter 6. After the device fabrication the sample is mounted on a chip carrier, as described in section 2.8 and placed in the sample puck connector of the PPMS stick. The PPMS system can be configured up to 9 T fields with a superconducting magnet. The sample can be cooled down up to 4 K. The PPMS rotator stick is connected with the stepper motor, such that the magnetic field varies in the plane of the sample.

After placing the sample in PPMS, it is connected to the measurement setup via a home-built switchbox, used to specify the input current and output voltage contacts. For the input current a home-built VI-IV meetkast ('measurement box') is used. The meetkast consists of a voltage-controllable current source which is used to generate the AC current sent to the sample at a frequency set by the lock-in amplifier. The meetkast also contains a voltage pre-amplifier with adjustable gain and bandwidth, used to pre-amplify the output voltage signals from the sample. Moreover, the measurement setup contains one or more Stanford Research Systems SR830 lock-in amplifiers, which filter the first, second or higher harmonic voltage signals from the pre-amplified output voltage signal. A picture of the measurement setup including a simplified connection scheme for the electrical detection is shown in Fig. 2.10.

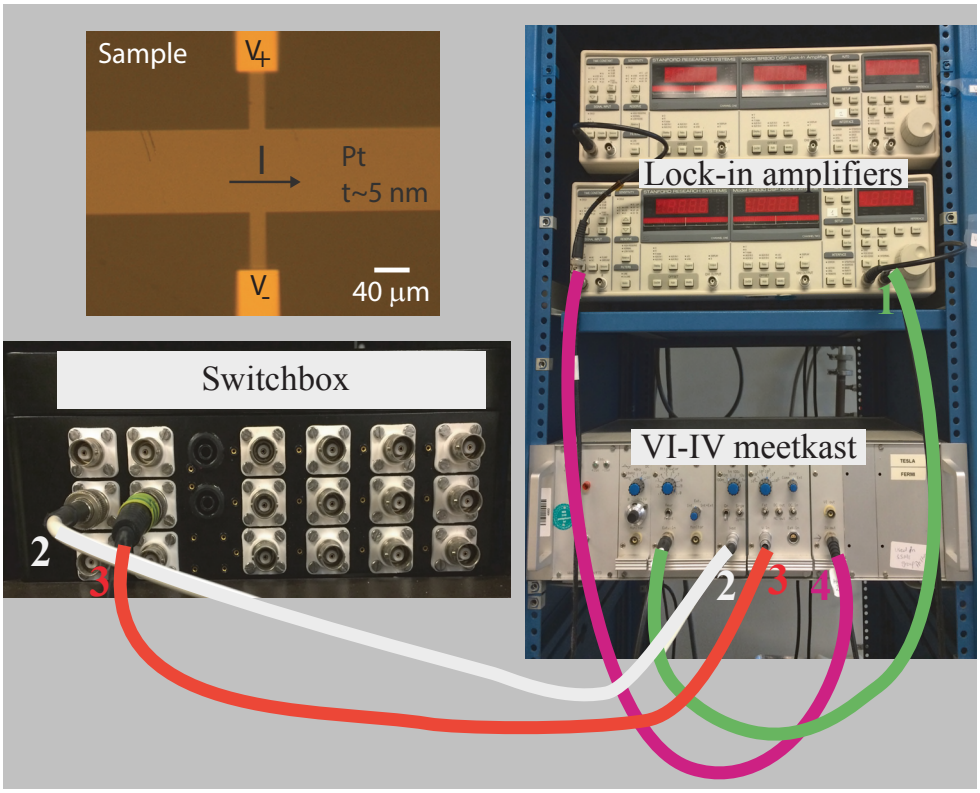

Figure 2.10: *(top left) Optical image of a typical device with a Hall-bar structure. (bottom left) A switchbox to connect the sample with desired electronics. (right) Measurement setup picture, illustrating the scheme of the lock-in detection technique: The first lock-in amplifier is set to a required frequency (f = 17 Hz), generating an AC voltage (at 1) which is sent to VI-IV meetkast where it is converted to an AC current (at 2) of desired amplitude. This current is sent to the sample via the switchbox, from another set of contacts (at 3) of the switchbox the voltage generated by the sample is detected and pre-amplified. Afterwards, the generated voltage is sent to the lock-in amplifiers (at 4) to separate the first, second and higher harmonic voltages.*

Bibliography

[1] A. V. Chumak, V. I. Vasyuchka, A. A. Serga, and B. Hillebrands, "Magnon spintronics," *Nature Physics* **11**, pp. 453–461, 2015.

[2] Y. Kajiwara, K. Harii, S. Takahashi, J. Ohe, K. Uchida, M. Mizuguchi, H. Umezawa, H. Kawai, K. Ando, K. Takanashi, S. Maekawa, and E. Saitoh, "Transmission of electrical signals by spin-wave interconversion in a magnetic insulator," *Nature* **464**, p. 262, Mar 2010.

[3] L. J. Cornelissen, J. Liu, R. A. Duine, J. B. Youssef, and B. J. van Wees, "Long-distance transport of magnon spin information in a magnetic insulator at room temperature," *Nature Physics* **11**, pp. 1022–1026, Dec 2015.

[4] K. Uchida, H. Adachi, T. Ota, H. Nakayama, S. Maekawa, and E. Saitoh, "Observation of longitudinal spin-Seebeck effect in magnetic insulators," *Applied Physics Letters* **97**(17), p. 172505, 2010.

[5] T. Schneider, A. A. Serga, B. Leven, B. Hillebrands, R. L. Stamps, and M. P. Kostylev, "Realization of spin-wave logic gates," *Applied Physics Letters* **92**(2), 2008.

[6] T. Valet and A. Fert, "Theory of the perpendicular magnetoresistance in magnetic multilayers," *Physical Review B* **48**, pp. 7099–7113, Sep 1993.

[7] S. U. Meyer, "Spin transport and dynamics in magnetic insulator/metal systems," *PhD thesis, Technical University of Munich* , Nov. 2015.

[8] N. Nagaosa, J. Sinova, S. Onoda, A. H. MacDonald, and N. P. Ong, "Anomalous Hall effect," *Reviews of Modern Physics* **82**, pp. 1539–1592, May 2010.

[9] M. Dyakonov and V. Perel, "Current-induced spin orientation of electrons in semiconductors," *Physics Letters A* **35**(6), pp. 459 – 460, 1971.

[10] J. E. Hirsch, "Spin hall effect," *Physical Review Letters* **83**, pp. 1834–1837, Aug 1999.

[11] Y. K. Kato, R. C. Myers, A. C. Gossard, and D. D. Awschalom, "Observation of the Spin Hall Effect in Semiconductors," *Science* **306**(5703), pp. 1910–1913, 2004.

[12] J. Wunderlich, B. Kaestner, J. Sinova, and T. Jungwirth, "Experimental Observation of the Spin-Hall Effect in a Two-Dimensional Spin-Orbit Coupled Semiconductor System," *Physical Review Letters* **94**, p. 047204, Feb 2005.

[13] J. Sinova, S. O. Valenzuela, J. Wunderlich, C. H. Back, and T. Jungwirth, "Spin Hall effects," *Reviews of Modern Physics* **87**, pp. 1213–1260, Oct 2015.

[14] E. Sagasta, Y. Omori, M. Isasa, M. Gradhand, L. E. Hueso, Y. Niimi, Y. Otani, and F. Casanova, "Tuning the spin hall effect of pt from the moderately dirty to the superclean regime," *Physical Review B* **94**, p. 060412, Aug 2016.

[15] R. Karplus and J. M. Luttinger, "Hall Effect in Ferromagnetics," *Physical Review* **95**, pp. 1154–1160, Sep 1954.

[16] L. Berger, "Side-Jump Mechanism for the Hall Effect of Ferromagnets," *Physical Review B* **2**, pp. 4559–4566, Dec 1970.

[17] M. V. Berry, "Quantal Phase Factors Accompanying Adiabatic Changes," *Proceedings of the Royal Society of London A* **392**(1802), pp. 45–57, 1984.

[18] S. Onoda, N. Sugimoto, and N. Nagaosa, "Quantum transport theory of anomalous electric, thermoelectric, and thermal Hall effects in ferromagnets," *Physical Review B* **77**, p. 165103, Apr 2008.

[19] T. Tanaka, H. Kontani, M. Naito, T. Naito, D. S. Hirashima, K. Yamada, and J. Inoue, "Intrinsic spin Hall effect and orbital Hall effect in $4d$ and $5d$ transition metals," *Physical Review B* **77**, p. 165117, Apr 2008.

[20] M. Isasa, E. Villamor, L. E. Hueso, M. Gradhand, and F. Casanova, "Temperature dependence of spin diffusion length and spin Hall angle in Au and Pt," *Physical Review B* **91**, p. 024402, Jan 2015.

[21] M. Morota, Y. Niimi, K. Ohnishi, D. H. Wei, T. Tanaka, H. Kontani, T. Kimura, and Y. Otani, "Indication of intrinsic spin Hall effect in $4d$ and $5d$ transition metals," *Physical Review B* **83**, p. 174405, May 2011.

[22] M. Schreier, G. E. W. Bauer, V. I. Vasyuchka, J. Flipse, K. ichi Uchida, J. Lotze, V. Lauer, A. V. Chumak, A. A. Serga, S. Daimon, T. Kikkawa, E. Saitoh, B. J. van Wees, B. Hillebrands, R. Gross, and S. T. B. Goennenwein, "Sign of inverse spin Hall voltages generated by ferromagnetic resonance and temperature gradients in yttrium iron garnet platinum bilayers," *Journal of Physics D: Applied Physics* **48**(2), p. 025001, 2015.

[23] N. Vlietstra, J. Shan, V. Castel, B. J. van Wees, and J. Ben Youssef, "Spin-Hall magnetoresistance in platinum on yttrium iron garnet: Dependence on platinum thickness and in-plane/out-of-plane magnetization," *Physical Review B* **87**, p. 184421, May 2013.

[24] N. Vlietstra, J. Shan, V. Castel, J. Ben Youssef, G. E. W. Bauer, and B. J. van Wees, "Exchange magnetic field torques in YIG/Pt bilayers observed by the spin-Hall magnetoresistance," *Applied Physics Letters* **103**(3), 2013.

[25] H. Nakayama, M. Althammer, Y.-T. Chen, K. Uchida, Y. Kajiwara, D. Kikuchi, T. Ohtani, S. Geprägs, M. Opel, S. Takahashi, R. Gross, G. E. W. Bauer, S. T. B. Goennenwein, and E. Saitoh, "Spin Hall Magnetoresistance Induced by a Nonequilibrium Proximity Effect," *Physical Review Letters* **110**, p. 206601, May 2013.

[26] Y.-T. Chen, S. Takahashi, H. Nakayama, M. Althammer, S. T. B. Goennenwein, E. Saitoh, and G. E. W. Bauer, "Theory of spin Hall magnetoresistance," *Physical Review B* **87**, p. 144411, Apr 2013.

[27] M. Althammer, S. Meyer, H. Nakayama, M. Schreier, S. Altmannshofer, M. Weiler, H. Huebl, S. Geprägs, M. Opel, R. Gross, D. Meier, C. Klewe, T. Kuschel, J. Schmalhorst, G. Reiss, L. Shen, A. Gupta, Y.-T. Chen, G. E. W. Bauer, E. Saitoh, and S. T. B. Goennenwein, "Quantitative study of the spin Hall magnetoresistance in ferromagnetic insulator/normal metal hybrids," *Physical Review B* **87**, p. 224401, Jun 2013.

[28] A. Brataas, "Insulating Magnets Control Neighbors Conduction," *View point in Physics 6* **56**, 2013.

[29] C. Hahn, G. de Loubens, O. Klein, M. Viret, V. V. Naletov, and J. Ben Youssef, "Comparative measurements of inverse spin Hall effects and magnetoresistance in YIG/Pt and YIG/Ta," *Physical Review B* **87**, p. 174417, May 2013.

[30] M. Isasa, A. Bedoya-Pinto, S. Vélez, F. Golmar, F. Sánchez, L. E. Hueso, J. Fontcuberta, and F. Casanova, "Spin hall magnetoresistance at $\mathrm{Pt}/\mathrm{CoFe_2O_4}$ interfaces and texture effects," *Applied Physics Letters* **105**(14), pp. –, 2014.

[31] N. Vlietstra, "Spin transport and dynamics in magnetic insulator/metal systems," *PhD thesis, University of Groningen* , Mar. 2016.

[32] X. Jia, K. Liu, K. Xia, and G. E. W. Bauer, "Spin transfer torque on magnetic insulators," *Europhysics Letters* **96**, p. 17005, Oct. 2011.

[33] A. Brataas, Y. Tserkovnyak, G. Bauer, and P. Kelly, "Spin pumping and spin transfer," in *Spin Current*, S. Maekawa, S. Valenzuela, E. Saitoh, and T. Kimura, eds., pp. ch.8,pp. 87 – 135, Oxford University Press, Oxford, 2012.

[34] D. Ralph and M. Stiles, "Spin transfer torques," *Journal of Magnetism and Magnetic Materials* **320**(7), pp. 1190 – 1216, 2008.

[35] Z. Wang, Y. Sun, Y.-Y. Song, M. Wu, H. Schultheiß, J. E. Pearson, and A. Hoffmann, "Electric control of magnetization relaxation in thin film magnetic insulators," *Applied Physics Letters* **99**(16), p. 162511, 2011.

[36] Y. Tserkovnyak, A. Brataas, and G. E. W. Bauer, "Spin pumping and magnetization dynamics in metallic multilayers," *Physical Review B* **66**, p. 224403, Dec 2002.

[37] E. Saitoh, M. Ueda, H. Miyajima, and G. Tatara, "Conversion of spin current into charge current at room temperature: Inverse spin-Hall effect," *Applied Physics Letters* **88**(18), 2006.

[38] F. D. Czeschka, L. Dreher, M. S. Brandt, M. Weiler, M. Althammer, I.-M. Imort, G. Reiss, A. Thomas, W. Schoch, W. Limmer, H. Huebl, R. Gross, and S. T. B. Goennenwein, "Scaling Behavior of the Spin Pumping Effect in Ferromagnet-Platinum Bilayers," *Physical Review Letters* **107**, p. 046601, Jul 2011.

[39] K. Xia, P. J. Kelly, G. E. W. Bauer, A. Brataas, and I. Turek, "Spin torques in ferromagnetic/normal-metal structures," *Physical Review B* **65**, p. 220401, May 2002.

[40] A. Kirihara, K. Kondo, M. Ishida, K. Ihara, Y. Iwasaki, H. Someya, A. Matsuba, K. Uchida, E. Saitoh, N. Yamamoto, S. Kohmoto, and T. Murakami, "Flexible heat-flow sensing sheets based on the longitudinal spin Seebeck effect using one-dimensional spin-current conducting films," *Scientific Reports* **6**, p. 23114, 2016.

[41] K. Uchida, J. Xiao, H. Adachi, J. Ohe, S. Takahashi, J. Ieda, T. Ota, Y. Kajiwara, H. Umezawa, H. Kawai, G. E. W. Bauer, S. Maekawa, and E. Saitoh, "Spin Seebeck insulator," *Nature Materials* **9**, p. 894, 2010.

[42] T. J. Seebeck, "Ueber die magnetische Polarisation der Metalle und Erze durch Temperaturdifferenz," *Annalen der Physik* **82**(3), pp. 253–286, 1826.

[43] F. Bakker, "Thermoelectric effects in magnetic nanostructures," *PhD thesis, University of Groningen* , Oct. 2012.

[44] A. Slachter, F. L. Bakker, J.-P. Adam, and B. J. van Wees, "Thermally driven spin injection from a ferromagnet into a non-magnetic metal," *Nature Physics* **6**, pp. 879 – 882, 2010.

[45] F. K. Dejene, J. Flipse, G. E. W. Bauer, and B. J. van Wees, "Spin heat accumulation and spin-dependent temperatures in nanopillar spin valves," *Nature Physics* **9**, pp. 636–639, 2013.

[46] A. Kirihara, K.-i. Uchida, Y. Kajiwara, M. Ishida, Y. Nakamura, T. Manako, E. Saitoh, and S. Yorozu, "Spin-current-driven thermoelectric coating," *Nature Materials* **11**, pp. 686–689, Mar 2012.

[47] M. Agrawal, V. I. Vasyuchka, A. A. Serga, A. Kirihara, P. Pirro, T. Langner, M. B. Jungfleisch, A. V. Chumak, E. T. Papaioannou, and B. Hillebrands, "Role of bulk-magnon transport in the temporal evolution of the longitudinal spin-Seebeck effect," *Physical Review B* **89**, p. 224414, Jun 2014.

[48] A. Kehlberger, U. Ritzmann, D. Hinzke, E.-J. Guo, J. Cramer, G. Jakob, M. C. Onbasli, D. H. Kim, C. A. Ross, M. B. Jungfleisch, B. Hillebrands, U. Nowak, and M. Kläui, "Length Scale of the Spin Seebeck Effect," *Physical Review Letters* **115**, p. 096602, Aug 2015.

[49] S. M. Rezende, R. L. Rodrìguez-Suàrez, R. O. Cunha, J. C. L. Ortiz, and A. Azevedo, "Bulk magnon spin current theory for the longitudinal spin Seebeck effect," *Journal of Magnetism and Magnetic Materials* **400**, pp. 171 – 177, 2016.

[50] J. Xiao, G. E. W. Bauer, K.-c. Uchida, E. Saitoh, and S. Maekawa, "Theory of magnon-driven spin Seebeck effect," *Physical Review B* **81**, p. 214418, Jun 2010.

[51] D. J. Sanders and D. Walton, "Effect of magnon-phonon thermal relaxation on heat transport by magnons," *Physical Review B* **15**, pp. 1489–1494, Feb 1977.

[52] S. M. Rezende, R. L. Rodríguez-Suárez, R. O. Cunha, A. R. Rodrigues, F. L. A. Machado, G. A. Fonseca Guerra, J. C. Lopez Ortiz, and A. Azevedo, "Magnon spin-current theory for the longitudinal spin-Seebeck effect," *Physical Review B* **89**, p. 014416, Jan 2014.

[53] R. A. Duine, A. Brataas, S. A. Bender, and Y. Tserkovnyak, "Spintronics and Magnon Bose-Einstein Condensation," *ArXiv e-prints,arXiv:1505.01329* , 2015.

[54] N. Vlietstra, J. Shan, B. J. van Wees, M. Isasa, F. Casanova, and J. Ben Youssef, "Simultaneous detection of the spin-Hall magnetoresistance and the spin-Seebeck effect in platinum and tantalum on yttrium iron garnet," *Physical Review B* **90**, p. 174436, Nov 2014.

[55] A. Aqeel, I. J. Vera-Marun, B. J. van Wees, and T. T. M. Palstra, "Surface sensitivity of the spin Seebeck effect," *Journal of Applied Physics* **116**(15), 2014.

[56] J. Flipse, F. K. Dejene, D. Wagenaar, G. E. W. Bauer, J. B. Youssef, and B. J. van Wees, "Observation of the Spin Peltier Effect for Magnetic Insulators," *Physical Review Letters* **113**, p. 027601, Jul 2014.

[57] S. A. Manuilov, C. H. Du, R. Adur, H. L. Wang, V. P. Bhallamudi, F. Y. Yang, and P. C. Hammel, "Spin pumping from spinwaves in thin film YIG," *Applied Physics Letters* **107**(4), 2015.

[58] M. Haertinger, C. H. Back, J. Lotze, M. Weiler, S. Geprägs, H. Huebl, S. T. B. Goennenwein, and G. Woltersdorf, "Spin pumping in YIG/Pt bilayers as a function of layer thickness," *Physical Review B* **92**, p. 054437, Aug 2015.

[59] V. Lauer, D. A. Bozhko, T. Brächer, P. Pirro, V. I. Vasyuchka, A. A. Serga, M. B. Jungfleisch, M. Agrawal, Y. V. Kobljanskyj, G. A. Melkov, C. Dubs, B. Hillebrands, and A. V. Chumak, "Spin-transfer torque based damping control of parametrically excited spin waves in a magnetic insulator," *Applied Physics Letters* **108**(1), 2016.

[60] M. Schreier, T. Chiba, A. Niedermayr, J. Lotze, H. Huebl, S. Geprägs, S. Takahashi, G. E. W. Bauer, R. Gross, and S. T. B. Goennenwein, "Current-induced spin torque resonance of a magnetic insulator," *Physical Review B* **92**, p. 144411, Oct 2015.

[61] A. A. Serga, A. V. Chumak, and B. Hillebrands, "YIG magnonics," *Journal of Physics D: Applied Physics* **43**(26), p. 264002, 2010.

[62] S. Geprägs, A. Kehlberger, F. D. Coletta, Z. Qiu, E.-J. Guo, T. Schulz, C. Mix, S. Meyer, A. Kamra, M. Althammer, H. Huebl, G. Jakob, Y. Ohnuma, H. Adachi, J. Barker, S. Maekawa, G. E. W. Bauer, E. Saitoh, R. Gross, S. T. Goennenwein, and M. Kläui, "Origin of the spin Seebeck effect in compensated ferrimagnets," *Nature Communications* **7**, p. 10452, 2016.

[63] A. A. Omrani, J. S. White, K. Prša, I. Živković, H. Berger, A. Magrez, Y.-H. Liu, J. H. Han, and H. M. Rønnow, "Exploration of the helimagnetic and skyrmion lattice phase diagram in Cu_2OSeO_3 using magnetoelectric susceptibility," *Physical Review B* **89**, p. 064406, Feb 2014.

[64] V. Tsurkan, S. Zherlitsyn, S. Yasin, V. Felea, Y. Skourski, J. Deisenhofer, H.-A. K. von Nidda, J. Wosnitza, and A. Loidl, "Unconventional Magnetostructural Transition in $CoCr_2O_4$ at High Magnetic Fields," *Physical Review Letters* **110**, p. 115502, Mar 2013.

[65] Y. Tokura and N. Kida, "Dynamical magnetoelectric effects in multiferroic oxides," *Philosophical Transactions of the Royal Society A* **369**(1951), pp. 3679–3694, 2011.

[66] M. Boer, "Incommensurate magnetism in $PrBa_2Cu_3O_{6+x}$," *Master thesis, University of Groningen* , Dec. 2015.

[67] N. Nagaosa and Y. Tokura, "Topological properties and dynamics of magnetic skyrmions," *Nature Nanotechnology* **8**, p. 899, Dec. 2013.

[68] H.-B. Braun, "Topological effects in nanomagnetism: from superparamagnetism to chiral quantum solitons," *Advances in Physics* **61**(1), pp. 1–116, 2012.

[69] Y. Tokura and S. Seki, "Multiferroics with Spiral Spin Orders," *Advanced Materials* **22**(14), pp. 1554–1565, 2010.

[70] T. Kimura, "Magnetoelectric Hexaferrites," *Annual Review of Condensed Matter Physics* **3**(1), pp. 93–110, 2012.

[71] N. Hlubek, P. Ribeiro, R. Saint-Martin, A. Revcolevschi, G. Roth, G. Behr, B. Büchner, and C. Hess, "Ballistic heat transport of quantum spin excitations as seen in $SrCuO_2$," *Physical Review B* **81**, p. 020405, Jan 2010.

2

Published as: A. Aqeel, I. J. Vera-Marun, B. J. van Wees & T. T. M. Palstra – *"Surface Sensitivity of spin Seebeck effect,"* J. Appl. Phys. **116**, 153705 (2014).

Chapter 3

Spin Seebeck effect in a single crystal YIG|Pt system

Abstract

We have investigated the influence of the interface quality on the spin Seebeck effect (SSE) of the bilayer system yttrium iron garnet (YIG) − platinum (Pt). The magnitude and shape of the SSE is strongly influenced by mechanical treatment of the YIG single crystal surface. We observe that the saturation magnetic field (H_{sat}^{SSE}) for the SSE signal increases from 55.3 mT to 72.8 mT with mechanical treatment. The change in the magnitude of H_{sat}^{SSE} can be attributed to the presence of a perpendicular magnetic anisotropy due to the treatment induced surface strain or shape anisotropy in the Pt/YIG system. Our results show that the SSE is a powerful tool to investigate magnetic anisotropy at the interface.

3.1 Introduction

The discovery of the spin Seebeck effect (SSE) [1] in insulators triggered the modern era of the field of spin caloritronics [2]. In insulators, instead of moving charges, only spin excitations (magnons) drive the non-equilibrium spin currents. In the spin Seebeck effect, spin currents are thermally excited in a ferromagnet FM and detected in a normal metal NM deposited on the FM. The bilayer NM/FM system in the SSE provides the opportunity to separately tune the properties of both layers to optimize the magnitude and magnetic field dependence of the SSE effect. The platinum (Pt) and yttrium iron garnet (YIG) bilayer system has attracted considerable attention for studying the spin Seebeck effect [1, 3–5] and for other spin dependent transport experiments [1, 6–13]. Platinum (Pt) has a large inverse spin Hall response [14] whereas YIG is an ideal ferromagnetic insulator due to low magnetic damping [2, 6, 15] and a large band gap [16] at room temperature.

The origin of the spin Seebeck effect is commonly explained by the difference in the magnon temperature in the FM and the phonon temperature in the NM, ΔT_{mp} [17, 18]. When the temperature gradient ∇T is applied across the NM/FM system, it creates a ΔT_{mp} based on the thermal conductivities of the magnon and the phonon subsystems [17]. This ΔT_{mp} induces a spin current density at the interface which

is detected in the normal metal Pt by the inverse spin Hall effect (ISHE). The ISHE signal depends on a scaling parameter, the interfacial SSE coefficient L_s, related to how efficiently the spin current density can be created across the interface under a certain ΔT_{mp}. The resulting spin Seebeck signal scales linearly with the length of the NM (l_{Pt}), therefore for the Pt/YIG system

$$V_{\text{ISHE}} \propto l_{Pt} \,.\, L_s \,.\, \nabla T \tag{3.1}$$

The scaling parameter L_s is proportional to the real part of the spin mixing conductance $g_r^{\uparrow\downarrow}$ at the interface. The spin mixing conductance $g_r^{\uparrow\downarrow}$ and therefore the SSE are very sensitive to the interface quality [19]. In recent years substantial effort has been made to improve the spin mixing conductance on thin films of YIG [19, 20] and bulk crystals [16, 21]. Unlike thin films, bulk crystals need an extra surface polishing step for the device fabrication, due to the initial surface roughness. The polishing of the crystal surface can influence the spin mixing conductance in several ways. Apart from changing the surface roughness, mechanical polishing can change the magnetic structures at the interface by inducing a small perpendicular anisotropy at the surface layer of the YIG crystal [22–24]. However, the effect of polishing on the spin Seebeck effect (SSE) has not yet been systematically studied. In this chapter, we report the effect of mechanical surface treatment of the YIG single crystals on the SSE effect. This systematic study reveals the surface sensitivity of the SSE and indicates new ways of surface modification for improved thermoelectric efficiency.

3.2 Experimental technique

In this study, we use the longitudinal configuration [3] for the spin Seebeck effect where the temperature gradient is applied across a NM/FM interface and parallel to the spin current direction J_s. In Fig. 3.1(a), we illustrate schematically the device configuration for measuring the SSE used in this study. The sample consists of a single crystal YIG slab and a Pt film sputtered on a (111) surface of the YIG crystal. When an out-of-plane (along z-axis) temperature gradient is applied to the Pt/YIG stack, magnons are thermally excited. Magnons inject a spin current along the z-axis and polarize the spins in the Pt film close to the interface parallel to the magnetization of the YIG crystal, as illustrated in Fig. 3.1(b). Due to the strong spin-orbit coupling in the Pt film, the spin polarization σ is converted to a voltage signal V_{ISHE}. The single crystals of YIG with the same purity were used in all measurements which were purchased from Crystal Systems Corporation, Hokuto, Yamanashi, Japan. These YIG crystals were grown by the floating zone method along the (111) direction. A diamond saw was used to cut the crystals. The YIG crystals were cleaned ultrasonically first in acetone and then ethanol baths.

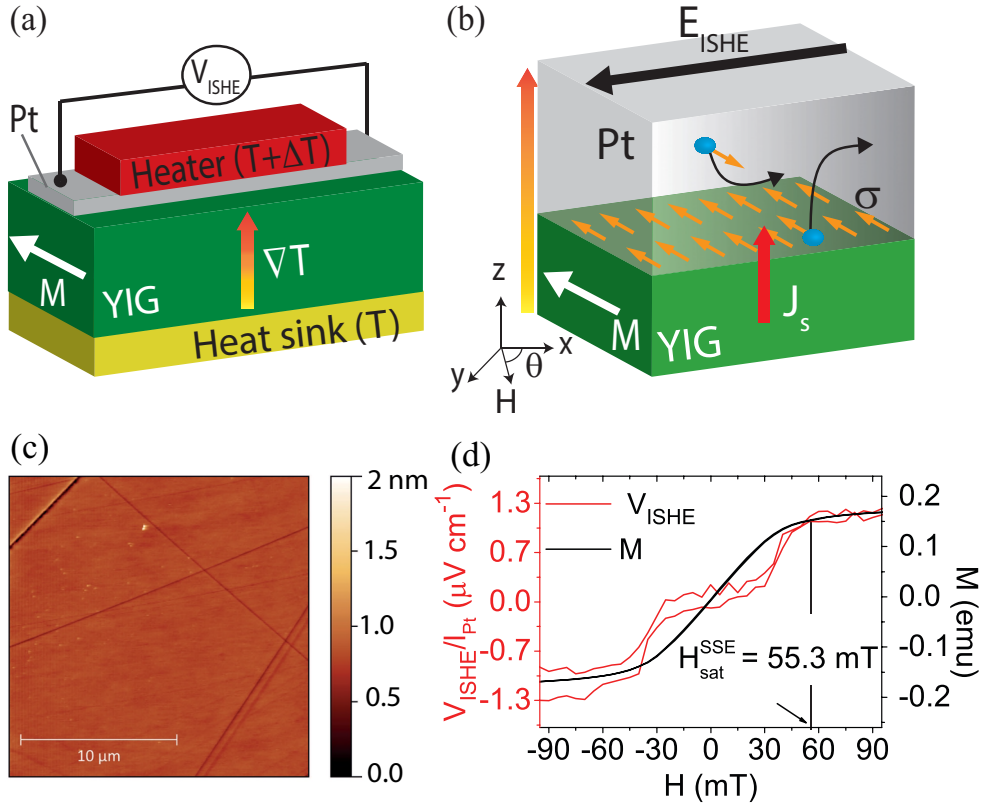

Figure 3.1: *(a) Device configuration of the longitudinal SSE where ∇T represents the temperature gradient across the Pt/YIG system. (b) Detection of spin current by the ISHE. The orange arrows indicate the spin polarization σ at the interface of the Pt/YIG system. M, J_S and E_{ISHE} represent the magnetization of YIG, spatial direction of the thermally generated spin current, and electric field induced by the ISHE, respectively. θ represents the angle between the external magnetic field H in the xy plane and the x-axis. (c) AFM height image of a single crystal YIG surface (20 x 20 μm^2) for sample S1. (d) a comparison between the magnetic field dependence of V_{ISHE} at ΔT = 3.6 K for sample S1 and the magnetization M of the YIG crystal.*

Three different types of surfaces were prepared for samples S1 - S3 by the following treatments:

- For S1: the YIG crystals were grinded with abrasive grinding papers (SiC P1200 - SiC P4000) at 150 rpm for 1h. After grinding, diamond particles were used with a sequence of 9 μm, 3 μm and 1 μm at 300 rpm for 30 mins, respectively. To remove the surface strain or surface damage due to diamond particles [22–

24], colloidal silica OPS (oxide polishing suspension) with a particle size of 40 nm was used, which can give mechanical as well as chemical polishing. To remove the residuals of polishing particles, samples were heated at 200 °C for 1h at ambient conditions. Then crystals were cleaned by acetone and ethanol in an ultrasonic bath before depositing the Pt layer on top.

- For S2: grinding, polishing and cleaning of the samples were done in the same way as described for S1. However, the colloidal silica OPS was not used for sample S2. Thus, the strained or damaged surface layer due to diamond polishing was retained.
- For S3: no mechanical polishing was done to obtain flat surfaces as done for samples S1 and S2. After cleaning in the same way as done for samples S1 and S2, Pt was deposited on the unpolished YIG crystal surface.

Table 3.1: *Surface treatment, surface roughness, and orientation of the YIG crystals for different samples.*

Samples	Polishing	Roughness	Orientation
S1	Silica	< 3 nm	(111)
S2	diamond	≥ 12 nm	(111)
S3	no	> 300 nm	(111)

The surface treatments are summarized in Table 3.1. The measurements of the spin Seebeck effect (SSE) were performed in the following way. The samples were magnetized in the xy plane of the YIG crystal by an external magnetic field H, as shown in Fig. 3.1. To excite magnons an external heater generates a temperature gradient ∇T across the Pt/YIG stack where the temperature of heat sink is denoted as T. The thickness of the YIG (Pt bar) is 3 mm (15 nm) for all samples. Regarding the lateral dimension of the Pt bar, the length (width) varies from 5 mm to 3 mm (2.5 mm to 1.5 mm) with all samples having ratios 2:1. The surface of the YIG crystals was analyzed by atomic force microscopy (AFM) before deposition of the Pt film on top. The observed spin Seebeck signals show a small offset which we removed. The field at which 95% of the SSE signal saturates is defined as $H_{\text{sat}}^{\text{SSE}}$. The magnetization M of the YIG crystal with a dimension of 2 mm x 1 mm was measured with a SQUID (Superconducting QUantum Interference Device) magnetometer.

3.3 Results and discussion

Fig. 3.1(c) shows the AFM height image of sample S1 with a surface roughness smaller than 3 nm. A distinct V_{ISHE} signal appears and saturates around ~ 55.3

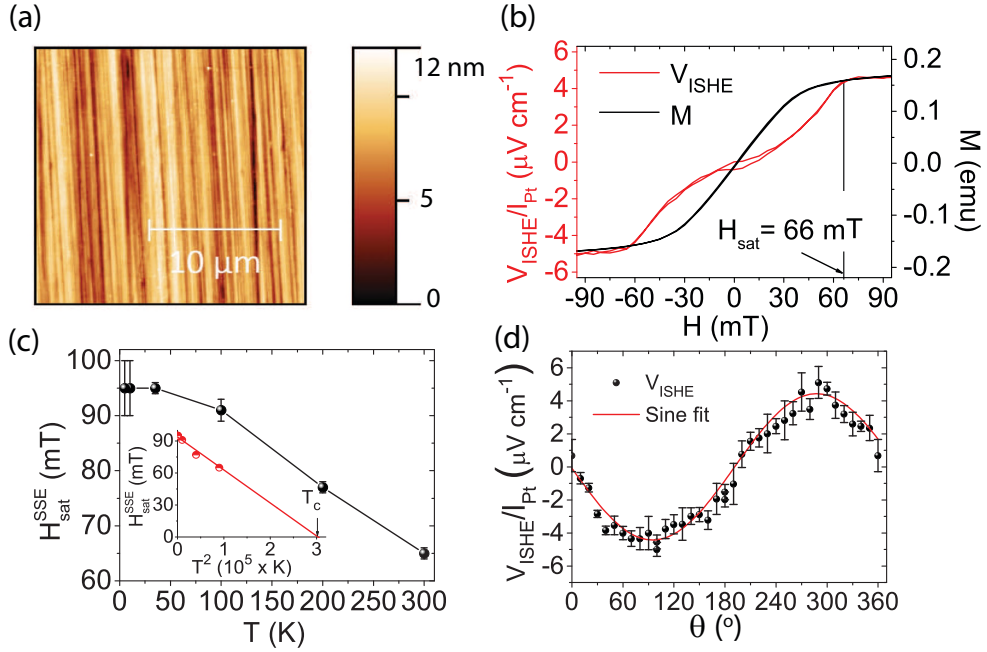

Figure 3.2: *(a) AFM height image of a single crystal YIG surface for sample S2 (20 x 20 μm^2). (b) Comparison between the H dependence of V_{ISHE} at ΔT = 3.6 K in sample S2 and the magnetization M of the YIG crystal. (c) Temperature dependence of H_{sat}^{SSE}. The inset shows H_{sat}^{SSE} as a function of T^{ε} where ε = 2. (d) V_{ISHE} as a function of the external magnetic field direction θ in the Pt/YIG system at a fixed magnetic field 80 mT.*

mT, which is close to the field required to saturate the magnetization of the YIG crystal, as illustrated in Fig. 3.1(d). Similarly, the YIG surface of sample S2 was analyzed by AFM. Fig. 3.2(a) shows that sample S2 has a surface roughness $\sim$ 12 nm with strip-like trenches at the surface. A clear spin Seebeck response has been observed for sample S2 by changing the applied magnetic field H. The signal saturates at relatively higher values of H ($\sim$ 66.1 mT) compared to the magnetization of YIG as shown in Fig. 3.2b. In addition, we checked the magnetic field dependence of the spin Seebeck response at low temperatures for sample S2, the temperature dependence of the $H_{\mathrm{sat}}^{\mathrm{SSE}}$ is given in Fig. 3.2(c). As the YIG crystal is a 3D isotropic ferrimagnet, the temperature dependence of the magnetic order parameter obeys a T^2 universality scaling [25]. To understand the temperature dependence of $H_{\mathrm{sat}}^{\mathrm{SSE}}$, we fitted $H_{\mathrm{sat}}^{\mathrm{SSE}}$ at low temperatures by assuming T_c = 553 K as shown in the inset of Fig. 3.2(c). The temperature dependence of $H_{\mathrm{sat}}^{\mathrm{SSE}}$ closely obeys the T^2 universality behavior of the order parameter of the YIG crystal with exponent ε = 2. It suggests

that the H_{sat}^{SSE} directly depends on the order parameter of the YIG crystal. To confirm further the origin of the observed signal, H is rotated in the xy plane. The V_{ISHE} signal follows the expected sinusoidal dependence for a spin Seebeck signal, as shown in Fig. 3.2(d).

Unlike the samples S1 and S2, sample S3 has a very large surface roughness (> 300 nm) as shown in Fig. 3.3(a). Nevertheless, a clear spin Seebeck signal was observed as shown in Fig 3.3(b).

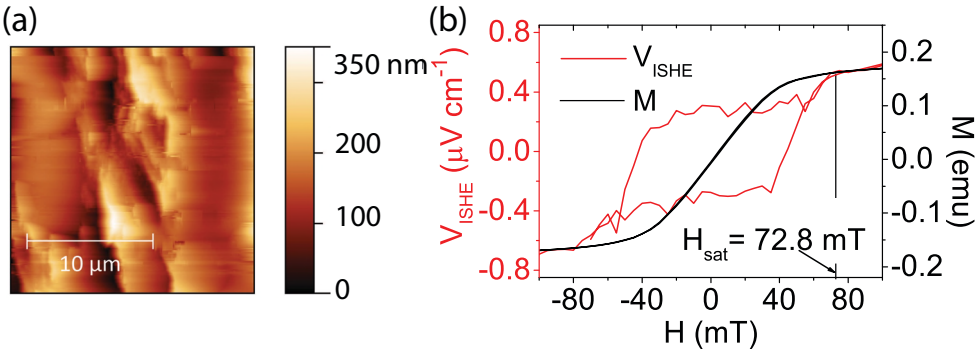

Figure 3.3: *(a) AFM height image of the YIG surface for sample S3 (20 x 20 μm^2) and (b) a comparison between the H dependence of V_{ISHE} at ΔT = 7.5 K in sample S3 and the magnetization M of the YIG crystal.*

From equation 3.1, it follows that the inverse spin Hall voltage V_{ISHE} is proportional to the applied temperature gradient ∇T and the length of the Pt bar l_{Pt}. V_{ISHE} increases by reducing the thickness of the Pt film t_{Pt}, for both the spin pumping [26] and the SSE [27] experiments. Therefore to compare samples with different Pt thickness we can define a parameter C as follows [26–28]:

$$C = \frac{1}{\tanh[\frac{t_{Pt}}{2\lambda_{Pt}}]\,\rho_{Pt}\,\frac{l_{Pt}}{t_{Pt}}}\,\frac{V_{ISHE}}{\nabla T} \tag{3.2}$$

Here, ∇T is defined as the temperature difference across the Pt/YIG stack normalized with the thickness of the YIG crystal, ρ_{Pt} is the resistivity of Pt and λ_{Pt} is the spin diffusion length of Pt. In these experiments, unlike ρ_{Pt}, λ_{Pt} cannot be measured directly, therefore we assumed that it remains constant for different samples. Note that for all samples discussed here $t_{Pt} > 2\,\lambda_{Pt}$ (where λ_{Pt} = 1.5 nm [12, 13]) so the $\tanh[\frac{t_{Pt}}{2\lambda_{Pt}}]$ term is approximately equal to 1 leading to $V_{ISHE} \propto 1/t_{Pt}$. Moreover, the C parameter is independent of the YIG thickness when the thickness is larger than the magnon mean free path and therefore it can be used as an indicator of changes in other parameters related to the interfacial mechanisms of the SSE.

Table 3.2: *Comparison of the resistance R of the Pt film, the C parameter and the H_{sat}^{SSE} for the SSE response in bulk single crystals and thin films*

	Bulk crystals				Thin films
	S1	S2	S3	Ref. [3]	Ref. [13]
R (Ω)	33.8	52.2	119	-	-
C (10^{-8}V Ω^{-1} K^{-1})	0.917	1.369	0.043	0.554	1.105
H_{sat}^{SSE} (mT)	55.3	66.1	72.8	40	2.5

The resistance of the Pt film varies between the samples S1-S3, nevertheless all samples have similar resistance within an order of magnitude as shown in Table 3.2. The observed change in the resistance is correlated with the roughness of the crystals, although we do not observe the same scaling for the SSE response. For example, the resistance of sample S2 is 50% higher than that of sample S1 whereas the SSE signal for sample S2 is only 30% higher than for sample S1. Furthermore the resistance of sample S3 is almost four times bigger than sample S1, however the SSE response actually follows the opposite trend, as it is actually more than an order of magnitude lower for S3 than the response for the samples S1 and S2. Therefore, we establish that the dominant mechanism relevant for the observed differences in the SSE signal is not the resistivity of the NM films but the quality of the NM/FM interface. Sample S1 gives a C parameter that is comparable to the value reported for thin films and bulk crystals as shown in Table 3.2. However, sample S2 shows 30% bigger and sample S3 shows more than an order of magnitude smaller value of the C parameter than sample S1. The observed variation in the value of the C parameter indicates the importance of mechanical treatment induced surface effects that we will discuss below.

Based on the experimental conditions listed in Table 3.1 and the results summarised in Table 3.2, we propose a possible mechanism for our observations. Fig. 3.4(a-c) schematically illustrates possible interface morphologies and the surface magnetization for the NM/FM system, for different interface conditions between the NM film and the FM crystal. Fig. 3.4(a) represents the case for a NM film deposited on an atomically flat FM crystal. Here, the case for sample S1 corresponds to Fig. 3.4(a). Fig. 3.4(b) depicts a situation for a NM deposited on a flat FM crystal but having a small perpendicular anisotropy at the surface. The situation represented in Fig. 3.4(b) corresponds to the case for sample S2. The surface of the YIG crystal for sample S2 contains trenches due to polishing of the YIG crystal with coarse diamond particles as shown in Fig. 3.2(a). The trenches at the interface can induce strain or shape anisotropy resulting in a perpendicular anisotropy at the interface. The presence of a small perpendicular anisotropy at the interface would increase the H_{sat}^{SSE}

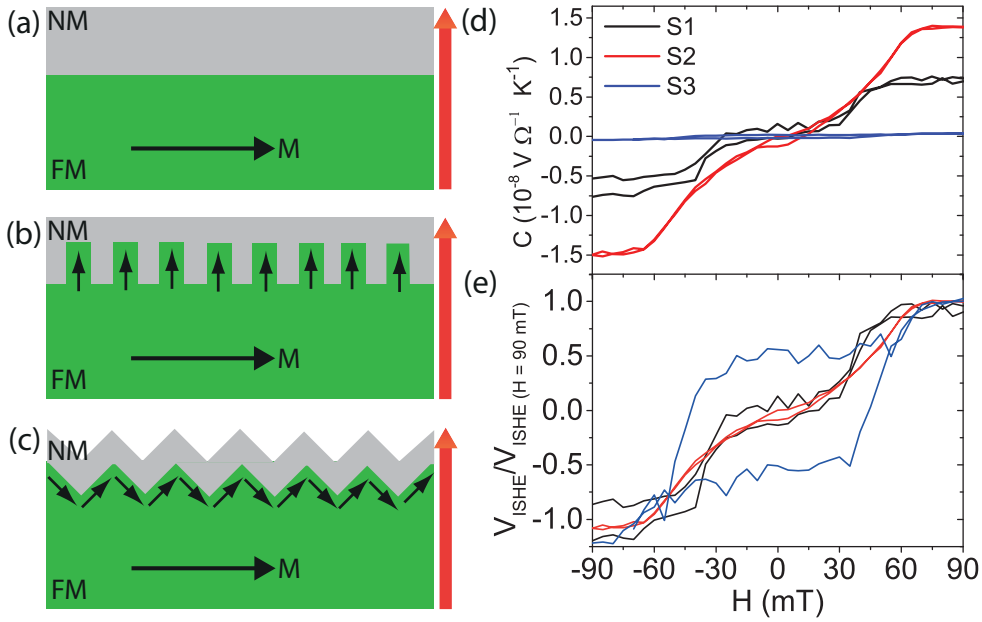

Figure 3.4: *(a-c) A schematic illustration of the interface morphologies of the NM/FM system for different surface treatments of the FM where orange arrows represent ∇T: (a) An atomically flat interface, (b) an interface with a perpendicular anisotropy and (c) a rough interface. (d) Comparison between the magnitude of the C parameter and (e) comparison between the line profile of the SSE signal as a function of H for all samples.*

compared to the bulk magnetization of the YIG crystal, which has been clearly observed for sample S2 (see Fig. 3.2(b)).

In addition, the magnitude of the SSE signal can also change if the mechanical polishing changes the atomic termination for the density of Fe atoms that are in direct contact with the Pt metal. If the density of Fe atoms at the surface is larger than the bulk of the YIG, the observed SSE signal would be larger [16, 21]. The increase in the SSE signal for sample S2 compared to sample S1 can be attributed to different chemical termination due to polishing with coarse diamond particles. Fig. 3.4(c) shows the case for a rough interface between the NM and the FM crystal which corresponds to the situation for sample S3. In case of sample S3, the lack of further mechanical treatment after cutting with a diamond saw leaves a very rough surface of the YIG crystal. The $H_{\mathrm{sat}}^{\mathrm{SSE}}$ is around 72.8 mT for sample S3 as shown in Fig. 3.3(b). The increase in the value of $H_{\mathrm{sat}}^{\mathrm{SSE}}$ for sample S3 compared to the magnetization of YIG can be due to a non-uniform magnetization at the interface resulting from high surface roughness of the YIG crystal.

Fig. 3.4(d) gives a comparison of the magnitude of the SSE signal in terms of the C parameter (as defined in equation 3.2) for samples with different mechanical treatments. The observed signal for sample S3 is smallest compared to other samples. This can be explained due to the increase of surface roughness [7, 16] resulting in the small spin mixing conductance at the interface. The sample S1 has the lowest surface roughness, however the SSE signal observed for sample S2 is the largest compared to the samples S1 and S3 as shown in Fig. 3.4(d). Therefore, for the largest roughness of sample S3 we see a relation between roughness and the SSE signal, but not for the samples S1 and S2. Hence, the roughness is not the only parameter and this might be related to the more abrasive nature of the diamond particles leaving a different chemical termination at the interface.

To compare the line profile of the V_{ISHE} signal, in Fig. 3.4(e) the signals are normalized by their value at H = 90 mT, where they reach saturation. Fig. 3.4(e) shows that the line profile of the SSE signal changes when moving from soft silica to coarse diamond particle polishing. For the samples S1 and S2 the V_{ISHE} is very small at zero applied field compared to the value measured at 90 mT. However, for sample S3 the V_{ISHE} is almost 64% of the value measured at H = 90 mT. The value of $H_{\mathrm{sat}}^{\mathrm{SSE}}$ is highest for sample S3 with the largest surface roughness and lowest for sample S1 with the smallest surface roughness. Therefore, $H_{\mathrm{sat}}^{\mathrm{SSE}}$ directly correlates with the roughness of sample. The large deviation in the magnitude of the SSE signal and $H_{\mathrm{sat}}^{\mathrm{SSE}}$ in the YIG crystals with different surface treatments emphasizes the surface sensitivity of the spin Seebeck effect. Our results indicate that not only the surface roughness but actual atomic structures and chemical termination at the interface also play an important role in the SSE.

3.4 Conclusions

In conclusion, we have shown a strong dependence of the spin Seebeck signal on the interface condition of the Pt/YIG bilayer system. We observed a change of 18 mT in the saturation field of the SSE signal by changing the type of polishing. Furthermore we observe the change in the magnitude of the SSE signal for different samples. No definite relation has been found between the SSE response and the sample roughness. However, we observe a direct correlation between the $H_{\mathrm{sat}}^{\mathrm{SSE}}$ and the roughness of sample, as the former increases by moving from soft toward coarse particle polishing. To understand the origin of the magnitude and change in the saturation field $H_{\mathrm{sat}}^{\mathrm{SSE}}$ for the observed SSE signal, due to different types of surface treatments, the crystal surfaces need to be investigated further in detail.

Author contributions

A. Aqeel and I. J. Vera-Marun designed the experiments. Crystal polishing, device fabrication and the measurements were carried out by A. Aqeel. A. Aqeel, I. J. Vera-Marun, B. J. van Wees, and T. T. M. Palstra carried out the analysis. A. Aqeel wrote the paper, involving all co-authors.

Bibliography

[1] K. Uchida, J. Xiao, H. Adachi, J. Ohe, S. Takahashi, J. Ieda, T. Ota, Y. Kajiwara, H. Umezawa, H. Kawai, G. E. W. Bauer, S. Maekawa, and E. Saitoh, "Spin Seebeck insulator," *Nature Materials* **9**, pp. 894–897, Nov. 2010.

[2] G. E. W. Bauer, E. Saitoh, and B. J. van Wees, "Spin caloritronics," *Nature Materials* **11**, pp. 391–399, Apr. 2012.

[3] K.-i. Uchida, H. Adachi, T. Ota, H. Nakayama, S. Maekawa, and E. Saitoh, "Observation of longitudinal spin-Seebeck effect in magnetic insulators," *Applied Physics Letters* **97**(17), p. 172505, 2010.

[4] A. Kehlberger, U. Ritzmann, D. Hinzke, E.-J. Guo, J. Cramer, G. Jakob, M. C. Onbasli, D. H. Kim, C. A. Ross, M. B. Jungfleisch, B. Hillebrands, U. Nowak, and M. Kläui, "Length Scale of the Spin Seebeck Effect," *Physical Review Letters* **115**, p. 096602, Aug 2015.

[5] A. Kirihara, K.-i. Uchida, Y. Kajiwara, M. Ishida, Y. Nakamura, T. Manako, E. Saitoh, and S. Yorozu, "Spin-current-driven thermoelectric coating," *Nature Materials* **11**, pp. 686–689, June 2012.

[6] Y. Kajiwara, K. Harii, S. Takahashi, J. Ohe, K. Uchida, M. Mizuguchi, H. Umezawa, H. Kawai, K. Ando, K. Takanashi, S. Maekawa, and E. Saitoh, "Transmission of electrical signals by spin-wave interconversion in a magnetic insulator," *Nature* **464**, pp. 262–266, Mar. 2010.

[7] C. Burrowes, B. Heinrich, B. Kardasz, E. A. Montoya, E. Girt, Y. Sun, Y.-Y. Song, and M. Wu, "Enhanced spin pumping at yttrium iron garnet/Au interfaces," *Applied Physics Letters* **100**(9), p. 092403, 2012.

[8] C. W. Sandweg, Y. Kajiwara, A. V. Chumak, A. A. Serga, V. I. Vasyuchka, M. B. Jungfleisch, E. Saitoh, and B. Hillebrands, "Spin Pumping by Parametrically Excited Exchange Magnons," *Physical Review Letters* **106**, p. 216601, May 2011.

[9] B. Heinrich, C. Burrowes, E. Montoya, B. Kardasz, E. Girt, Y.-Y. Song, Y. Sun, and M. Wu, "Spin Pumping at the Magnetic Insulator (YIG)/Normal Metal (Au) Interfaces," *Physical Review Letters* **107**, p. 066604, Aug. 2011.

[10] S. M. Rezende, R. L. Rodriguez-Suarez, M. M. Soares, L. H. Vilela-Leao, D. Ley Dominguez, and A. Azevedo, "Enhanced spin pumping damping in yttrium iron garnet/Pt bilayers," *Applied Physics Letters* **102**(1), p. 012402, 2013.

[11] Z. Qiu, Y. Kajiwara, K. Ando, Y. Fujikawa, K. Uchida, T. Tashiro, K. Harii, T. Yoshino, and E. Saitoh, "All-oxide system for spin pumping," *Applied Physics Letters* **100**(2), p. 022402, 2012.

[12] N. Vlietstra, J. Shan, V. Castel, J. Ben Youssef, G. E. W. Bauer, and B. J. van Wees, "Exchange magnetic field torques in YIG/Pt bilayers observed by the spin-Hall magnetoresistance," *Applied Physics Letters* **103**(3), p. 032401, 2013.

[13] J. Flipse, F. K. Dejene, D. Wagenaar, G. E. W. Bauer, J. B. Youssef, and B. J. van Wees, "Observation of the Spin Peltier Effect for Magnetic Insulators," *Physical Review Letters* **113**, p. 027601, Jul 2014.

[14] M. Ishida, A. Kirihara, H. Someya, K. Uchida, S. Kohmoto, E. Saitoh, and T. Murakami, "Observation of Longitudinal Spin Seebeck Effect with Various Transition Metal Films," *ArXiv e-prints* , 2013.

[15] S. Chikazumi, *Physics of ferromagnetism*, Oxford University Press, 1977.

[16] X. Jia, K. Liu, K. Xia, and G. E. W. Bauer, "Spin transfer torque on magnetic insulators," *Europhysics Letters* **96**, p. 17005, Oct. 2011.

[17] J. Xiao, G. E. W. Bauer, K.-c. Uchida, E. Saitoh, and S. Maekawa, "Theory of magnon-driven spin Seebeck effect," *Physical Review B* **81**, p. 214418, June 2010.

[18] H. Adachi, K.-I. Uchida, E. Saitoh, and S. Maekawa, "Theory of the spin Seebeck effect," *Reports on Progress in Physics* **76**(3), p. 036501, 2013.

[19] M. B. Jungfleisch, V. Lauer, R. Neb, A. V. Chumak, and B. Hillebrands, "Improvement of the yttrium iron garnet/platinum interface for spin pumping-based applications," *Applied Physics Letters* **103**(2), p. 022411, 2013.

[20] Z. Qiu, K. Ando, K. Uchida, Y. Kajiwara, R. Takahashi, H. Nakayama, T. An, Y. Fujikawa, and E. Saitoh, "Spin mixing conductance at a well-controlled platinum/yttrium iron garnet interface," *Applied Physics Letters* **103**(9), p. 092404, 2013.

[21] K. Uchida, T. Nonaka, T. Kikkawa, Y. Kajiwara, and E. Saitoh, "Longitudinal spin Seebeck effect in various garnet ferrites," *Physical Review B* **87**, p. 104412, Mar. 2013.

[22] D. J. Craik and P. M. Griffiths, "Domain Configurations on Ferrites," *Proceedings of the Physical Society* **73**, p. 1, 1959.

[23] D. J. Craik and R. S. Tebble, "Magnetic domains," *Reports on Progress in Physics* **24**, p. 116, 1961.

[24] R. V. Coleman, *Solid State Physics*, vol. 11, Academic Press, New York and London, 1974.

[25] I. H. Solt Jr., "Temperature Dependence of YIG Magnetization," *Journal of Applied Physics* **33**(3), p. 1189, 1962.

[26] V. Castel, N. Vlietstra, J. Ben Youssef, and B. J. van Wees, "Platinum thickness dependence of the inverse spin-Hall voltage from spin pumping in a hybrid yttrium iron garnet/platinum system," *Applied Physics Letters* **101**(13), pp. –, 2012.

[27] Y. Saiga, K. Mizunuma, Y. Kono, J. C. Ryu, H. Ono, M. Kohda, and E. Okuno, "Platinum thickness dependence and annealing effect of the spin-Seebeck voltage in platinum/yttrium iron garnet structures," *Applied Physics Express* **7**(9), p. 093001, 2014.

[28] H. Nakayama, K. Ando, K. Harii, T. Yoshino, R. Takahashi, Y. Kajiwara, K. Uchida, Y. Fujikawa, and E. Saitoh, "Geometry dependence on inverse spin Hall effect induced by spin pumping in $Ni_{81}Fe_{19}$/Pt films," *Physical Review B* **85**, p. 144408, Apr 2012.

3

Published as: A. Aqeel, N. Vlietstra, J. A. Heuver, G. E. W. Bauer, B. Noheda, B. J. van Wees, and T. T. M. Palstra – *"Spin-Hall magnetoresistance and spin Seebeck effect in spin-spiral and paramagnetic phases of multiferroic $CoCr_2O_4$ films,"* Phys. Rev. B **92**, 224410 (2015).

Chapter 4

Spin-Hall magnetoresistance and spin Seebeck effect in multiferroic $CoCr_2O_4$ films

Abstract

We report on the spin Hall magnetoresistance (SMR) and spin Seebeck effect (SSE) in multiferroic $CoCr_2O_4$ (CCO) spinel thin films with Pt contacts. We observe a large enhancement of both signals below the spin-spiral ($T_s = 28\,\mathrm{K}$) and the spin lock-in ($T_{\mathrm{lock-in}} = 14\,\mathrm{K}$) transitions. The SMR and SSE responses in the spin lock-in phase are one order of magnitude larger than those observed at the ferrimagnetic transition temperature ($T_c = 94\,\mathrm{K}$), which indicates that the interaction between spins at the Pt|CCO interface is more efficient in the non-collinear magnetic state. At $T > T_c$, magnetic field-induced SMR and SSE signals are observed, which can be explained by a high interface susceptibility. Our results show that the spin transport at the Pt|CCO interface is sensitive to the magnetic phases but cannot be explained solely by the bulk magnetization.

4.1 Introduction

Ferro (ferri) magnetic insulators (FMI) with normal metallic (NM) contacts that support the spin Hall effect (SHE) and its inverse (ISHE) open new functionalities in the field of spintronics. The SHE refers to a charge current that induces a transverse spin current, which can be injected to actuate a metallic or insulating ferromagnet. The ISHE converts a spin current pumped out of a ferromagnet into a transverse charge current in the normal metal. These concepts have been confirmed by many experiments on FMI|NM bilayers of a magnetic insulator (usually yttrium iron garnet) and a heavy normal metal (usually platinum), for example spin-pumping by ferromagnetic resonance [1–4], the spin Seebeck effect (SSE) [5–8], the spin Peltier effect [9] and the spin Hall magnetoresistance (SMR) [10–15]. In the SMR, both SHE and the ISHE act in a concerted manner to allow electrical detection of the FMI magnetization direction. The SSE refers to the conversion of thermal excitations of the magnetic order parameter (spin waves or magnons) into a spin current pumped into NM and detected by the ISHE. The SSE and the SMR have been investigated until now only for a limited number of insulating ferrimagnets (garnets and spinels) with collinear

magnetizations and recently, in an antiferromagnetic insulator [16]. However, magnetic insulators come in a large variety of magnetic orders. Especially fascinating are non-collinear magnets with competing magnetic interactions (spin frustration) induced by competing next-nearest neighbor exchange. Alternatively, the spin-orbit coupling, such as the Moriya-Dzyaloshinskii interaction, favors complex spiral configurations and skyrmion order. While the coupling of non-collinear magnetizations with spin, charge and heat transport is currently one of the hottest subjects in magnetism, its role in the SMR and SSE appears to have not been studied yet.

Non-collinear magnetism emerges when the second-nearest neighbor magnetic interactions are of the same order as the first one, generating geometrical frustration that favors spin canting. Various spin-spiral orders, like proper screw, cycloidal, longitudinal-conical and transverse-conical spiral, have been observed. The cycloidal and the transverse-conical spiral orders break the inversion symmetry and induce a spontaneous electrical polarization, making these spiral magnetic systems multiferroic [17–21]. Here, we focus on non-collinear and multiferroic $CoCr_2O_4$ (CCO) thin films, reporting to the best of our knowledge the first experimental observation of the SMR and the SSE in the Pt|CCO system for a wide range of temperatures including the ferrimagnetic and the spin-spiral phases.

CCO is one of the rare multiferroic materials with linear magnetoelectric coupling [22, 23]. It has a normal spinel structure with three sublattices. The Co^{2+} ions are located exclusively in the tetrahedral sites (forming one sublattice) while Cr^{3+} ions reside in the octahedral sites (in two sublattices). The Cr^{3+} ions form a pyrochlore lattice with magnetic geometrical frustration [24, 25]. Bulk CCO exhibits long-range collinear ferrimagnetic order below $T_c = 93\,K - 95\,K$ [24, 26, 27], with an easy axis of magnetization along the [001] direction, as illustrated in Fig. 4.1(a) and (c). At $T_s = 28\,K$, the ferrimagnetic long-range order adopts an additional short-range spiral order as illustrated in Fig. 4.1(b) and (c), which is known as the spin-spiral phase transition. The conical spiral has 48°, 71° and 28° cone angles with the [001] direction for the Co-, Cr I- and Cr II- sublattices, respectively. Below T_s, magnetic spin-spirals move the oxygen atoms off-center due to the inverse Dzyaloshinskii-Moriya interaction [26, 28], which results in the appearance of a spontaneous electrical polarization. At $T_{\mathrm{lock-in}} = 14\,K$, the spin-spiral becomes commensurate with the lattice by the spin-lattice coupling, which is known as the spin lock-in transition.

Here, we report a systematic study of the SMR and the SSE in the Pt|CCO bilayers from low to room temperature ($T = 5\,\mathrm{K} - 300\,\mathrm{K}$). At each temperature, we record the dependence on the angle of an in-plane applied magnetic field. We observe strong effects of the CCO magnetic order with largest signals in the spin lock-in phase at $T < 14\,\mathrm{K}$.

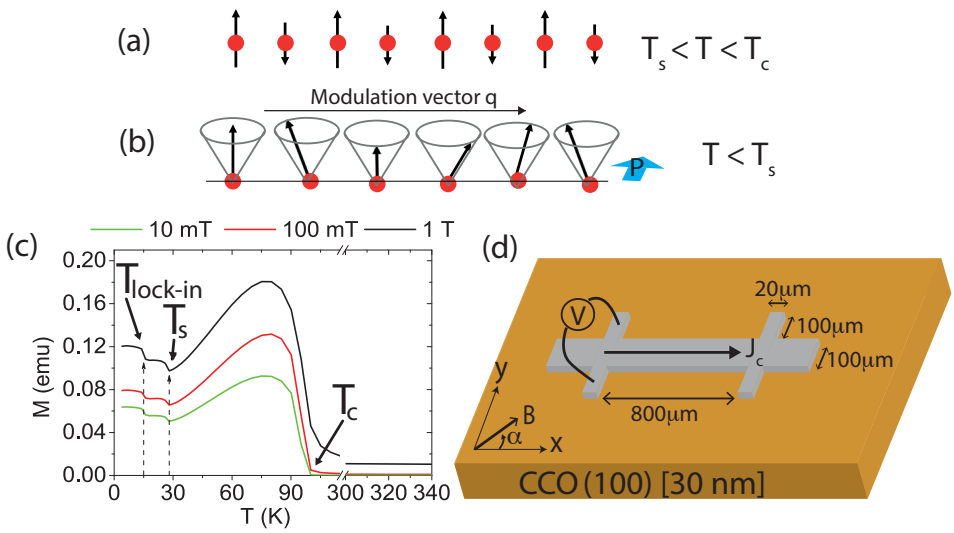

Figure 4.1: *(a,b) Impression of the types of magnetic order in CCO. (a) Ferrimagnetic state for $T_s < T < T_c$ and (b) transverse conical spiral state for $T < T_s$ with an electrical polarization P. Here, T_c and T_s are the Curie transition temperature to a collinear ferrimagnetic phase and that the spin-spiral transition temperature, respectively. (c) The temperature dependence of the zero field cooled magnetization of the CCO target powder used for the film deposition for different applied magnetic fields. $T_{\mathrm{lock-in}}$ is the spin lock-in magnetic transition temperature. (d) Device configuration for the transverse resistance (planar Hall effect) measurement of the Pt film on top of CCO.*

4.2 Sample growth and characteristics

30 nm-thick CCO films were grown on (001) MgO substrates by pulsed laser deposition (PLD). Sintered ceramic CCO targets [29] were ablated with a KrF excimer laser light with a wavelength of 248 nm and a repetition frequency of 0.5 Hz. During the deposition, the MgO substrates were kept at 500 °C in oxygen plasma atmosphere, having a base pressure of 0.01 mbar. Afterwards, the films were cooled down, with 5 °C per minute in 0.5 bar O_2 atmosphere. Before further device fabrication, the films were annealed at 200 °C for 60 min in an O_2 atmosphere. The crystal structure of the CCO films was determined by x-ray diffraction (XRD), where the rocking curves show high crystalline quality with a Full Width at Half Maximum (FWHM) below 0.03°.

The magnetization of the CCO films was measured by a SQUID magnetometer. The films show an in-plane magnetic anisotropy with a coercive field H_c around 2 T. For temperatures below 50 K, the magnetic transitions are hard to detect due to a

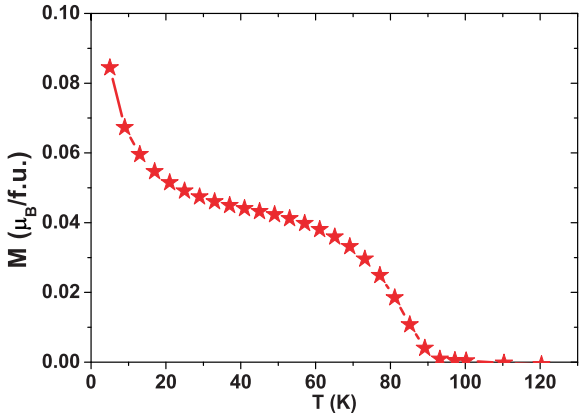

Figure 4.2: *In-plane magnetization of a CCO film on a MgO substrate in a magnetic field of 0.01 T after cooling in 1 T.*

large paramagnetic substrate background compared to the small magnetic moment of the thin film (see section 5.6). Nevertheless, SQUID measurements [30, 31] and x-ray resonance magnetic scattering both indicate the same magnetic transitions in thin films as reported for bulk CCO. In order to demonstrate the magnetic transitions in CCO, we measured the temperature dependence of the magnetization of bulk CCO targets used for the film deposition. Fig. 4.1(c) shows the magnetization of the CCO targets with the same transitions as reported in literature [32]. We carried out transport experiments on Hall-bar structures patterned by electron beam lithography onto which a $4\,\mathrm{nm}$-thick Pt film was deposited by DC sputtering, as shown in Fig. 4.1(d).

4.2.1 $CoCr_2O_4$ film magnetization

The temperature-dependent magnetization of the CCO film in Fig. 4.2 as measured by SQUID magnetometry is evidence for a phase transition at $T_c = 94\,\mathrm{K}$ to collinear ferrimagnet order, but the spin-spiral and spin lock-in transitions are not visible, because of the small magnetization of a thin film as explained above. The apparent increase in the magnetization below 20 K is probably caused by paramagnetic impurities in the substrate.

4.3 Measurement techniques

SMR and SSE have been measured simultaneously by lock-in detection [33]. Using two Stanford SR-830 Lock-in amplifiers, the first and second harmonic voltage response were recorded separately. To minimize the background voltage, we used the transverse instead of the longitudinal configuration, as schematically shown in

Fig.4.1(d), which is also referred to as "planar Hall" voltage. The SMR signal scales linearly with the applied current and therefore it is detected in the first order response of the Pt resistance [33]. The current-induced SSE scales quadratically with the applied current and therefore it is detected in the second order resistance response. The angular dependence of the SMR and the SSE were studied by rotating an external magnetic field in the plane of the film [34] that above T_c induces a magnetization or (if large enough) aligns the direction of the CCO magnetization below T_c. The in-plane angle α of the magnetic field is defined relative to the current direction along the y-axis as indicated in Fig. 4.1(d). All experiments were carried out in a quantum design PPMS system, at magnetic fields $B \geq 2\,\mathrm{T}$ and for temperatures from 5 to $300\,\mathrm{K}$.

4.3.1 Lock-in detection

All measurements shown above, are carried out using a lock-in detection technique [33] with $I \leq 5\,\mathrm{mA}$ AC bias in the Pt film. The generated voltage can be expanded as

$$V(t) = R_1 I(t) + R_2 I^2(t) + R_3 I^3(t) + \cdots , \tag{4.1}$$

where R_n represents the n-th order response. For $I(t) = \sqrt{2} I_o \sin \omega t$, with angular frequency ω and rms value I_0, the harmonic response coefficients R_n are obtained by measuring the different frequency components $(1\omega, 2\omega, \cdots)$ with a lock-in amplifier. The detected n-th harmonic response at a set phase ϕ can be written as

$$V_n(t) = \frac{\sqrt{2}}{T} \int_{t-T}^{t} \sin\left(n\omega s + \phi\right) V(s) ds. \tag{4.2}$$

Focussing on the first and second order response, we define the output voltage of the lock-in amplifier for the first and second harmonic responses by using Eq. (7.2) and Eq. (4.2) as:

$$\begin{array}{c} V_1 = I_0 R_1 \\ V_2 = I_0^2 R_2/\sqrt{2} \end{array} \quad \text{for} \quad \begin{array}{c} \phi = 0^{\mathrm{o}} \\ \phi = -90^{\mathrm{o}} \end{array} \tag{4.3}$$

The SMR and the SSE signals appear in the first and second harmonic responses in Eq. (4.3), respectively.

In the linear response regime at currents $I \leq 2\,\mathrm{mA}$, the SMR scales linearly and the SSE scales quadratically with the applied current as shown in Fig. 4.3(a,b). However, at $I > 2\,\mathrm{mA}$, the SMR (SSE) does no longer depend linearly (quadratically) on the current I. The results for the SMR are gathered in the linear regime. At $T > T_s$ the SSE signal decreases rapidly and we record the SSE also at the high current $I = 5\,\mathrm{mA}$, as shown in Fig. 4.3(c).

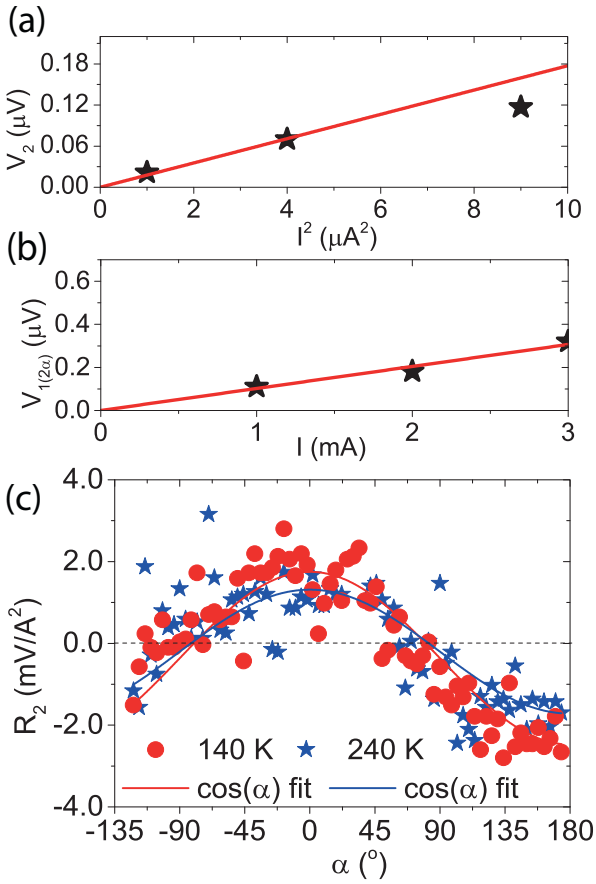

Figure 4.3: *(a) Dependence of the second harmonic response V_2 on I^2 due to the SSE, generated by current induced heating and (b) dependence of first harmonic contribution $V_{1(2\alpha)}$, due to the SMR, by an AC current I sent through the Pt Hall-bar in a magnetic field of 4 T. The SMR scales linearly and the SSE scales quadratically with current I in the linear regime ($I \leq 2\,mA$). (c) The angular dependence of second harmonic response, R_2, for $I = 5\,mA$, $H = 4$ T at $T = 140\,K$ and $240\,K$.*

4.4 Results and discussion

4.4.1 Spin-Hall magnetoresistance in Pt|$CoCr_2O_4$

Owing to the SHE, an AC current through the Pt Hall-bar creates an ac spin accumulation at the Pt|CCO interface that can be partially absorbed or fully reflected, depending on the interface magnetization $\vec{M}$ of the FMI (see Fig. 4.4(a) and (b)). The reflected spin currents generate an extra charge current via the ISHE, thereby reducing the resistance. While the longitudinal resistance establishes the maximum modulation between these two configurations with $\alpha = 0^o$ or 90^o, the planar Hall effect vanishes. In contrast, when $\alpha = 45^o$, the ISHE is maximal [35], as sketched in Fig. 4.4(c). The additional emf (electromotive force) scales with the applied current and is therefore detected by the first harmonic transverse resistance R_1 [33], defined as V_1/I, where V_1 is first harmonic signal of the lock-in amplifier generated by the

applied AC current of amplitude I (see section 4.3.1 for more details).

The α dependence of the first harmonic response R_1 at 5 K in Fig. 4.4(d) shows on top of the expected SMR an ordinary Hall effect (OHE) generated by a magnetic field component normal to the film due to a slight misalignment of the sample by an angle β. The OHE voltage has a $\sin(\alpha + \phi)$ angular dependence, where the phase ϕ is governed by the sample tilt direction. A prefactor of $0.7\,\mu$V at a current of 2 mA in a magnetic field 6 T corresponds to a tilt of $\beta < 2^{\circ}$. The ordinary Hall voltage of Pt|CCO is nearly temperature-independent and scales linearly with the applied current and magnetic field, as expected. After subtracting the OHE from R_1, the anticipated $\sin 2\alpha$ dependence associated to the SMR remains [10], as illustrated in Fig. 4.4(d). The SMR signal, $R^{\mathrm{ampl}}_{1(2\alpha)}$, is defined as the amplitude of the $\sin 2\alpha$ component and plotted in Fig. 4.4(e), (f) and (g) as a function of temperature in magnetic fields of 6 T, 4 T and 2 T, respectively. Exchanging the current and voltage probes in the Hall bar in field of 6 T leads to identical SMR profiles, confirming that the interface magnetization is parallel to the applied field. The SMR of CCO and yttrium iron garnet (YIG) are compared in section 4.4.3.

Below the collinear ferrimagnetic transition temperature $T_c = 94\,\mathrm{K}$, the SMR signal increases with decreasing temperature. The inset of Fig. 4.4(e) recorded at a magnetic field of 6 T shows a distinct change of slope at the spin-spiral transition temperature to a non-collinear magnetic phase, $T_s = 28\,\mathrm{K}$. At $T < T_s$, the SMR signal is more than one order of magnitude larger than the signal observed at T_c. A further decrease in temperature below the spin lock-in transition temperature, $T_{\mathrm{lock-in}} = 14\,\mathrm{K}$, doubles the SMR compared to T_s. This observation indicates that the exchange interaction between metal and magnet in the Pt|CCO system is more efficient in the non-collinear spiral phase than in the collinear ferrimagnetic phase. The maximum SMR signal is observed in the spin lock-in phase, when the period of the spin-spiral becomes commensurate with the lattice. Below T_c, $R_1 = A_1 T^{-1}$ (see Fig. 4.5(a)) gives an excellent fit, where A_1 scales linearly with the applied magnetic field, as shown in Fig. 4.5(b). A_1 should be proportional to the interface spin-mixing conductance that describes the ability of the ferromagnet to absorb or emit transverse polarized spin currents. When the interface magnetization vanishes, therefore, so does A_1. Above T_c, all magnetization is generated by the applied magnetic field and A_1 is a measure of the interface paramagnetic susceptibility. For a magnetic interface, we anticipate a bilinear $A_1(B)$, with a large slope at low magnetic fields that reflects the expulsion of magnetic domain walls. The extrapolation of the high-field data should lead to a finite cut-off at zero magnetic fields (as in studies of the anomalous Hall effect). However, the extrapolation of $A_1(B)$ does not lead to a statistically significant $A_1(0)$. In the present, we therefore cannot confirm whether the observed SMR signals reflect the paramagnetic susceptibility of a non-magnetic interface or a spontaneous interface magnetization texture.

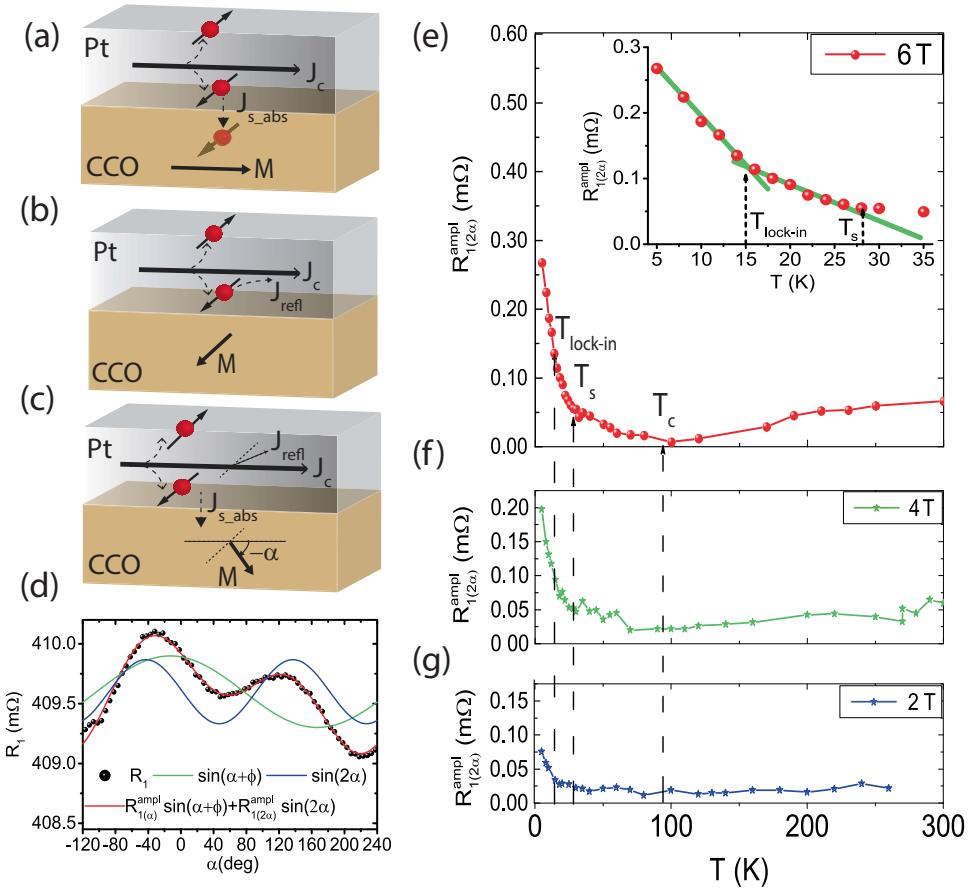

Figure 4.4: *(a-c) Illustration of the SMR in Pt|CCO bilayers. A charge current I induces a spin current and thereby spin accumulation at the Pt|CCO interface by virtue of the SHE. (a) This spin accumulation is absorbed as a spin transfer torque when the magnetization $\vec{M}$ is perpendicular to the current-induced spin polarization in Pt. (b) When $\vec{M}$ is parallel to the spin accumulation, the spin current is reflected back into Pt, where it generates an additional charge current, $J_{\rm refl}$ by the ISHE. (c) When $\vec{M}$ is at an angle α to J_c, the component of the spin accumulation perpendicular to $\vec{M}$ is absorbed and the parallel component is reflected, leading to an extra charge current component normal to J_c that is detected in the Hall configuration. (d) The angular dependence of the 1$^{\rm st}$ harmonic response in the transverse configuration, $R_1 = V_1/I$, for $I = 2$ mA at 5 K in an applied magnetic field of 6 T. The $\sin(\alpha+\phi)$ and $\sin 2\alpha$ curves illustrate the additive contributions from the ordinary Hall effect and the SMR. (e), (f) and (g) show the temperature dependence of the SMR, $R^{\rm ampl}_{1(2\alpha)}$ for $J_c = 2$ mA at 6 T, 4 T and 2 T, respectively. Here, $R^{\rm ampl}_{1(2\alpha)}$ is the amplitude of the $\sin 2\alpha$ component from the SMR. T_c, T_s and $T_{\rm lock-in}$ are the ferrimagnetic, spin-spiral and spin lock-in magnetic transition temperatures, respectively. The inset in (e) is a zoomed-in image of the SMR signal below T_s and $T_{\rm lock-in}$ at 6 T.*

In order to shed more light on the T-dependence for $T < T_c$, we compare the SMR with the bulk magnetization, as shown in Fig. 4.1(c). The T_c, T_s and $T_{\mathrm{lock-in}}$ transition temperatures established from the SMR closely correspond to the transition temperatures observed in the bulk magnetization. In the spin-spiral and spin lock-in phases, the bulk magnetization does not depend much on temperature, as shown in Fig. 4.1(c), in stark contrast to the SMR below T_s (Fig. 4.4(e)). According to present understanding, the SMR does not directly reflect the bulk magnetization. Theoretically, it is generated by the modulation of the spin current at the NM|FMI interface by the magnetization direction [35] and it is roughly proportional to the density of parallel and/or antiparallel-oriented magnetic moments at the interface [36]. The SMR enhancement below T_s thus reflects an increased (anti)ferromagnetic order of the magnetic moments at the interface. The induced interface magnetization can be generated by either Co ions, contributing to the ferrimagnetic component, or Cr ions responsible for the cycloidal component of the spin-spiral. The ferrimagnetic component saturates around $28\,\mathrm{K}$, therefore we cannot explain the enhanced SMR below $28\,\mathrm{K}$. However, neutron scattering experiments show that the spiral component below $T_s = 28\,\mathrm{K}$ strongly depends on temperature [24], similarly to the SMR signal. We therefore venture that the development of the spiral order should be explained by a strongly temperature-dependent ordering of Cr ions that does not contribute to the global magnetization. This implies that by a simple transport experiment we can distinguish ferrimagnetic from cycloidal components of the interface magnetization.

We observe a finite SMR in the paramagnetic phase for $T > T_c$ complementing reports on spin pumping [37] and the spin Seebeck effect[8] in the paramagnetic state. In CCO the magnetic susceptibility, for $T > T_c$, follows a Curie-Weiss law with a negative Curie-Weiss temperature $\theta_{CW} = -550\,\mathrm{K}$, which is evidence for antiferromagnetic correlations. The high ratio $|\theta_{CW}|/T_c \approx 6$ indicates a significant magnetic frustration due to competing sublattice exchange interactions in CCO [32], resulting in short range order above T_c. The SMR signal above T_c increases with temperature until it saturates to a constant value around room temperature, as shown in Fig. 4.4(e-g). The SMR signal for $T > T_c$ provides evidence for an unusual interface magnetic susceptibility of our films. We fitted the SMR signals with the Curie-Weiss law, but a single fitting parameter A_2 does not capture the contributions from the molecular fields. Much unlike the bulk magnetic susceptibility, the SMR signal is suppressed at T_c which can be taken care of by introducing an additional parameter A_3, as shown in Fig. 4.5(a). Both fitting parameters A_2 and A_3 scale linearly with the applied magnetic field, as shown in Fig. 4.5(c) and (d). These results support our conclusion drawn earlier that the SMR signal cannot be solely explained by the bulk magnetization of CCO, even in the paramagnetic phase. The temperature-independent background modelled by A_3 and the negative sign of A_2 remain unex-

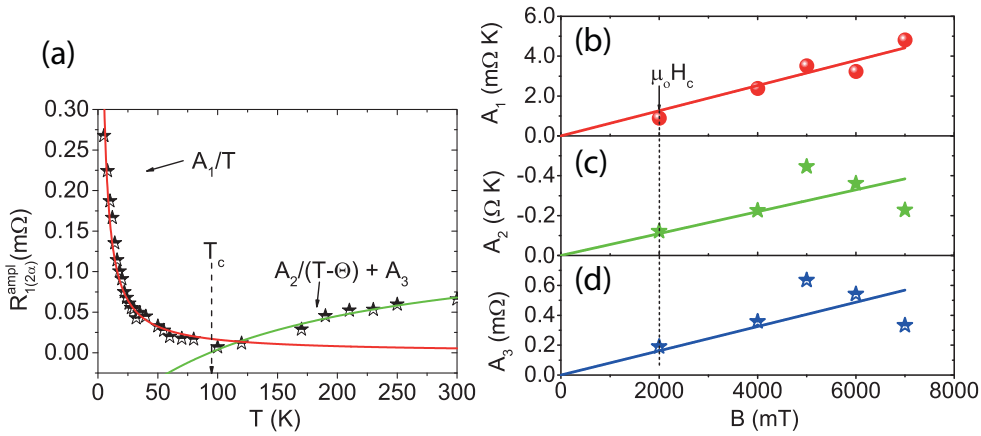

Figure 4.5: *(a) shows the temperature dependence of $R^{ampl}_{1(2\alpha)}$ in a magnetic field of 6 T for $I = 2\,mA$. The red curve shows the fit with the Curie law at low temperatures below T_c and the green curve shows the fit in the high temperature range above T_c with the Curie-Weiss law (for $\theta_{CW} = -550\,K$). (b), (c) and (d) show the field dependence of the fitting parameters A_1, A_2 and A_3, respectively.*

4

plained, but indicate that the short-range order reported for bulk CCO above T_c is importantly modified at the interface with Pt.

4.4.2 Spin Seebeck effect in Pt|$CoCr_2O_4$

We now discuss the SSE signal observed in the second harmonic response with the lock-in detection technique as described in Ref. 33. The SSE is caused by the Joule heating of the Pt Hall-bar, generating a heat current into the ferromagnet which is absorbed by magnons. This heat current is associated with a spin current polarized along the magnetization direction, which can be detected electrically by the ISHE, as sketched in Fig. 4.6(a). The second harmonic response is $R_2 = \sqrt{2}V_2/I^2$, where V_2 is the second harmonic signal of the lock-in amplifier at a phase set at $\phi = -90^o$ [33]. The observed second harmonic response of the transverse resistance obeys the $\sin\alpha$ angular dependence anticipated for the SSE, as shown in Fig. 4.6(b) We define the amplitude of the $R_2^{\rm ampl} = R_2/\cos\alpha$ for each temperature and magnetic field strength. The SSE signal for Pt|CCO has the same sign as for Pt|YIG (see section 4.4.3). Fig. 4.6(c), (d) and (e) show the temperature dependence of $R_2^{\rm ampl}$ in magnetic fields of 6 T, 4 T and 2 T, respectively.

In the collinear ferrimagnetic state at $T < T_c$, the SSE response increases with decreasing temperature. Fig. 4.6(c) gives evidence of a large SSE enhancement below the spin-spiral transition temperature T_s and again below $T_{\rm lock-in}$.

The SSE signal below T_s is five times larger than the signal observed at T_c. The inset of Fig. 4.6(c) illustrates that the SSE at $T < T_{\mathrm{lock-in}}$ increases by an order of magnitude from $T = 80\,\mathrm{K}$. Moreover below $T_s = 28\,\mathrm{K}$, the SSE signal scales linearly with the applied magnetic field. The SSE is too noisy to provide as clear evidence for phase transitions at T_c, T_s and $T_{\mathrm{lock-in}}$ as the SMR signals do.

Conventional thermoelectric effects become small with decreasing temperatures, so what causes the observed remarkable enhancement at low temperatures? We can understand the temperature dependence of the SSE signal by considering the contributions from different magnetic sublattices [38, 39]. CCO is a collinear ferrimagnet above T_s, with three sublattices associated with Co and oppositely polarized Cr I and Cr II ion moments [24], but without any magnetization compensation below T_c. The magnetic sublattices contribute to the SSE by correlated thermal fluctuations. The coupled sublattices have acoustic (ferromagnetic) and optical (antiferromagnetic) modes. The fundamental ferromagnetic modes govern the low energy excitations that are probed by ferromagnetic resonance and Brillouin light scattering. The optical modes are shifted to higher energy by the exchange interaction. In the collinear ferrimagnetic state close to T_c, the magnetic order and exchange interaction is still weak. The ferromagnetic mode then only slightly dominates the optical modes that are still substantially excited. The acoustic and optical modes contribute to the SSE with different sign and close to T_c they cancel to a large extent. By decreasing the temperature, the exchange splitting of the optical modes increases and therefore, they become increasingly depleted. The suppression of the thermal pumping of the optical modes therefore leads to an apparent enhancement of the spin Seebeck effect at lower temperature. This mechanism explains [40] the low temperature sign change of the SSE of the ferrimagnetic insulator $Gd_3Fe_5O_5$ (GdIG) [39] as well as the apparent suppression of the SSE in YIG at temperatures above 300 K [41].

In contrast to collinear magnetic order, the magnetization texture of a spin spiral is sensitively modulated by an external magnetic field [42], which might be reflected in the observed magnetic field dependence of the SSE below T_s, as shown in Fig. 4.6(c-e). The increase of the SSE with applied magnetic field below T_s should persist until the Co^{2+} and Cr^{3+} momenta of $3\mu_B$/ion are fully aligned. No signs of magnetization saturation were observed at magnetic fields up to 30 T [32], so it would be interesting to find out whether also the spin Seebeck effect can be enhanced by applying high magnetic fields.

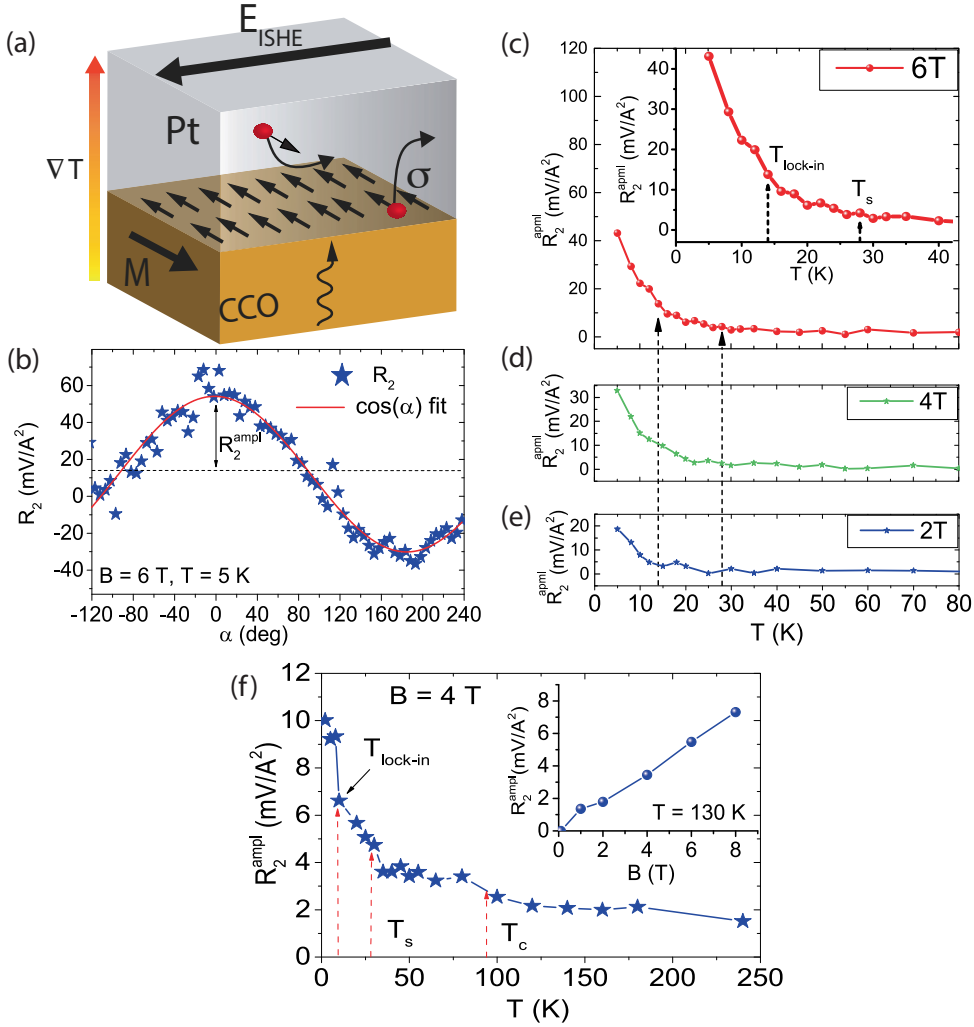

Figure 4.6: *(a) Spin Seebeck effect in Pt|CCO. A thermal gradient creates magnons at the interface by absorption of a spin current from Pt with polarization $\vec{\sigma} \| \vec{M}$, where $\vec{M}$ is the CCO interface magnetization. The spin current generates an electromotive force $\vec{E}_{ISHE}$ by the ISHE. (b) The angular dependence of the second harmonic response, $R_2 = \sqrt{2}V_2/I^2$ at $5\,K$, for $I = 2\,\mathrm{mA}$ in an applied magnetic field of 6 T. (c), (d) and (e) show the temperature dependence of R_2^{ampl} at 6 T, 4 T and 2 T for $I = 2\,\mathrm{mA}$, respectively. The inset of (c) emphasizes the enhancement of the SSE signal below the spin spiral (T_s) and spin lock-in ($T_{\mathrm{lock-in}}$) transition temperatures in a magnetic field of 6 T. (f) Temperature dependence of R_2^{ampl} in the non-linear current regime ($I = 5\,\mathrm{mA}$), with inset showing the magnetic field dependence of R_2^{ampl} at $T = 130\,\mathrm{K}$.*

The observed correlation between the SMR and SSE suggests that the spin-mixing conductance, i.e., the transport measure of the exchange interaction between ferromagnet and normal metal, does play an important role. Other factors, such as the magnetization damping and the magnon transport to the interface that is affected by the magnon-phonon interaction [43], may contribute to the observed enhancement in the SSE below T_s. A quantitative description of the SSE can be approached by atomistic spin simulations that take into account the full spin wave spectrum associated to the three sublattices with different cone angles, chirality, and damping parameters, as well the spin mixing conductances of the interface to Pt [40].

Above T_c the SSE cannot be established at small heating current levels ($I = 2\,\mathrm{mA}$), as shown in Fig. 4.6(c). However, at a larger current ($I = 5\,\mathrm{mA}$) in a magnetic field of 4 T, a finite SSE signal is detected above T_c and up to room temperature, see Fig. 4.6(f). At these current levels, the SSE voltage $\propto I^2$ and $T_{\mathrm{lock-in}}$ is shifted to lower temperature by $4\,\mathrm{K}$ due to sample heating. The SSE still scales linearly with the applied magnetic field as shown for $T = 130\,\mathrm{K}$ in the inset of Fig. 4.6(f). The presence of the SSE above T_c can be explained by the large longitudinal magnetic susceptibility of CCO films that is responsible for the SMR response as well [37].

4.4.3 SMR and the SSE in Pt|$CoCr_2O_4$ vs. Pt|YIG

To compare the SMR and the SSE response in Pt|CCO system to that of Pt|YIG, the angular dependence of Pt|YIG system is also systematically studied at different temperatures. A $4\,\mathrm{nm}$-thick Pt Hall-bar was deposited on a $4\times4\,\mathrm{mm}^2$ YIG film by DC sputtering [33]. The Pt Hall-bar has a length of $500\,\mu\mathrm{m}$ and a width of $50\,\mu\mathrm{m}$, with side contacts of $10\,\mu\mathrm{m}$ width. A $200\,\mathrm{nm}$-thick monocrystalline YIG film is used. The YIG film is grown by liquid phase epitaxy on a (111) $Gd_3Ga_5O_{12}$ (GGG) substrate. We observe the same sign of the SMR signals for Pt|CCO and Pt|YIG, as expected. A change of the sign of SSE has been observed in a compensated ferrimagnet [39] but for both Pt|YIG and Pt|CCO system the sign remains normal for all temperatures ($5 - 300\,\mathrm{K}$).

The temperature dependence of the SMR and SSE is observed to be very different in the Pt|CCO as compared to the Pt|YIG system. In Pt|CCO, both SMR and SSE signals are enhanced at temperatures much lower than T_c, as shown in Fig. 4.4(e) and Fig. 4.6(c) with maximal values around $5\,\mathrm{K}$ in the spin lock-in phase. In contrast, Pt|YIG displays conventional behavior, with both SMR and SSE larger at room temperature than at low temperatures. Fig. 4.7(a) shows the temperature dependence of the SMR signal in the Pt|YIG system at relatively large current levels of $I = 2.5\,\mathrm{mA}$. The SMR signal slightly increases with decreasing temperature until 150 K and decreases again upon cooling even more [44]. The decrease in the SMR signal in Pt|YIG has been ascribed to a decrease in the Pt spin Hall angle with decreasing temperature

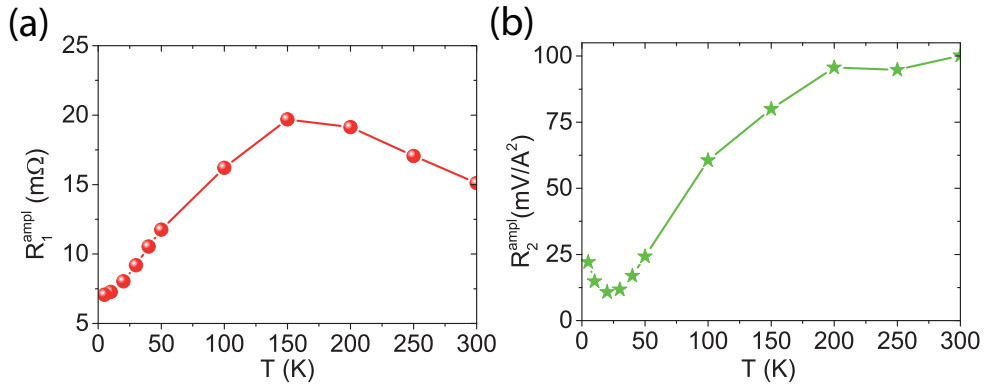

Figure 4.7: *(a) Temperature dependence of the SMR and (b) the SSE in the Pt|YIG system for* $2.5\,mA$ *current through the Pt Hall-bar in a magnetic field of 0.1 T.*

[45]. The SMR signal observed at 5 K is twice smaller than that at room temperature. The SSE in Pt|YIG does not change much until $T = 200\,\mathrm{K}$, while a further decrease in temperature suppresses the SSE as shown in Fig. 4.7(b). A small increase in the SSE is observed for $T < 30\,\mathrm{K}$.

The ordinary Hall effect as observed in the first harmonic response of the transverse resistance (as shown in Fig. 4.4(d)) is almost temperature-independent in the Pt|CCO system and scales linearly with the applied field as expected. The ordinary Hall effect is not observed in the Pt|YIG system because a much weaker field suffices to saturate the YIG magnetization ($H_c < 1\,\mathrm{mT}$). Moreover, the SMR signal observed in the Pt|CCO (shown in Fig. 4.4(e)) is smaller than that in the Pt|YIG system, resulting in a relatively larger contribution of the ordinary Hall effect. The SMR response observed at 5 K in the Pt|CCO is more than one order of magnitude smaller than the signal observed in the Pt|YIG.

4.5 Conclusions

In conclusion, by lock-in detection we simultaneously measured the SMR and SSE in Pt|CCO bilayers. The temperature dependence of the SMR and, though less so, the SSE, exposes distinct anomalies at the magnetic phase transitions. A remarkable enhancement of both SMR and SSE signals is observed at low temperatures ($T < T_s$). The SMR is more than one order of magnitude larger at $T < T_{\mathrm{lock-in}}$ as compared to the signals around T_c. We relate the observed enhancement of the SMR below T_s to contributions from the cycloidal spiral projected onto the spin accumulation at the Pt|CCO interface. The SSE signal also increases by a factor of two when lowering

the temperature below T_s. The temperature dependence of the SSE does not simply reflect the bulk magnetization; instead the intricate magnetization dynamics of coupled sublattices needs to be considered. Our results suggest that the magnons associated with the Cr-sublattice magnetization texture play an essential role in the SSE. We establish that the SMR and SSE are powerful instruments that complement ferromagnetic resonance and neutron scattering techniques to analyze the magnetization dynamics of complex oxides including multiferroics.

Author contributions

A. Aqeel and N. Vlietstra designed the experiments. Thin films were grown by J. A. Heuver and B. Noheda. Device fabrication was done by A. Aqeel and N. Vlietstra. The measurements were carried out by A. Aqeel. A. Aqeel, N. Vlietstra, B. J. van Wees, and T. T. M. Palstra carried out the analysis. Theoretical understanding was developed by G. E. W. Bauer. A. Aqeel wrote the paper, involving all co-authors.

Bibliography

[1] C. W. Sandweg, Y. Kajiwara, A. V. Chumak, A. A. Serga, V. I. Vasyuchka, M. B. Jungfleisch, E. Saitoh, and B. Hillebrands, "Spin Pumping by Parametrically Excited Exchange Magnons," *Physical Review Letters* **106**, p. 216601, May 2011.

[2] V. Castel, N. Vlietstra, B. J. van Wees, and J. Ben Youssef, "Frequency and power dependence of spin-current emission by spin pumping in a thin-film YIG/Pt system," *Physical Review B* **86**, p. 134419, Oct 2012.

[3] C. Hahn, G. de Loubens, M. Viret, O. Klein, V. V. Naletov, and J. Ben Youssef, "Detection of Microwave Spin Pumping Using the Inverse Spin Hall Effect," *Physical Review Letters* **111**, p. 217204, Nov 2013.

[4] K. Harii, T. An, Y. Kajiwara, K. Ando, H. Nakayama, T. Yoshino, and E. Saitoh, "Frequency dependence of spin pumping in $Pt/Y_3Fe_5O_{12}$ film," *Journal of Applied Physics* **109**(11), pp. –, 2011.

[5] K. Uchida, J. Xiao, H. Adachi, J. Ohe, S. Takahashi, J. Ieda, T. Ota, Y. Kajiwara, H. Umezawa, H. Kawai, G. E. W. Bauer, S. Maekawa, and E. Saitoh, "Spin Seebeck insulator," *Nature Materials* **9**, pp. 894–897, Nov. 2010.

[6] M. Schreier, A. Kamra, M. Weiler, J. Xiao, G. E. W. Bauer, R. Gross, and S. T. B. Goennenwein, "Magnon, phonon, and electron temperature profiles and the spin Seebeck effect in magnetic insulator/normal metal hybrid structures," *Physical Review B* **88**, p. 094410, Sep 2013.

[7] A. Aqeel, I. J. Vera-Marun, B. J. van Wees, and T. T. M. Palstra, "Surface sensitivity of the spin Seebeck effect," *Journal of Applied Physics* **116**(15), p. 153705, 2014.

[8] S. M. Wu, J. E. Pearson, and A. Bhattacharya, "Paramagnetic Spin Seebeck Effect," *Physical Review Letters* **114**, p. 186602, May 2015.

[9] J. Flipse, F. K. Dejene, D. Wagenaar, G. E. W. Bauer, J. Ben Youssef, and B. J. van Wees, "Observation of the Spin Peltier Effect for Magnetic Insulators," *Physical Review Letters* **113**, p. 027601, Jul 2014.

[10] M. Althammer, S. Meyer, H. Nakayama, M. Schreier, S. Altmannshofer, M. Weiler, H. Huebl, S. Geprägs, M. Opel, R. Gross, D. Meier, C. Klewe, T. Kuschel, J. Schmalhorst, G. Reiss, L. Shen, A. Gupta, Y.-T. Chen, G. E. W. Bauer, E. Saitoh, and S. T. B. Goennenwein, "Quantitative study of the spin Hall magnetoresistance in ferromagnetic insulator/normal metal hybrids," *Physical Review B* **87**, p. 224401, Jun 2013.

[11] N. Vlietstra, J. Shan, V. Castel, B. J. van Wees, and J. Ben Youssef, "Spin-Hall magnetoresistance in platinum on yttrium iron garnet: Dependence on platinum thickness and in-plane/out-of-plane magnetization," *Physical Review B* **87**, p. 184421, May 2013.

[12] H. Nakayama, M. Althammer, Y.-T. Chen, K. Uchida, Y. Kajiwara, D. Kikuchi, T. Ohtani, S. Geprägs, M. Opel, S. Takahashi, R. Gross, G. E. W. Bauer, S. T. B. Goennenwein, and E. Saitoh, "Spin Hall Magnetoresistance Induced by a Nonequilibrium Proximity Effect," *Physical Review Letters* **110**, p. 206601, May 2013.

[13] N. Vlietstra, J. Shan, V. Castel, J. Ben Youssef, G. E. W. Bauer, and B. J. van Wees, "Exchange magnetic field torques in YIG/Pt bilayers observed by the spin-hall magnetoresistance," *Applied Physics Letters* **103**(3), 2013.

[14] C. Hahn, G. de Loubens, O. Klein, M. Viret, V. V. Naletov, and J. Ben Youssef, "Comparative measurements of inverse spin Hall effects and magnetoresistance in YIG/Pt and YIG/Ta," *Physical Review B* **87**, p. 174417, May 2013.

[15] M. Isasa, A. Bedoya-Pinto, S. Vélez, F. Golmar, F. Sánchez, L. E. Hueso, J. Fontcuberta, and F. Casanova, "Spin Hall magnetoresistance at Pt/$CoFe_2O_4$ interfaces and texture effects," *Applied Physics Letters* **105**(14), p. 142402, 2014.

[16] J. H. Han, C. Song, F. Li, Y. Y. Wang, G. Y. Wang, Q. H. Yang, and F. Pan, "Antiferromagnet-controlled spin current transport in $SrMnO_3$/Pt hybrids," *Physical Review B* **90**, p. 144431, Oct 2014.

[17] M. Fiebig, "Revival of the magnetoelectric effect," *Journal of Physics D: Applied Physics* **38**(8), p. R123, 2005.

[18] S.-W. Cheong and M. Mostovoy, "Multiferroics: a magnetic twist for ferroelectricity," *Nature Materials* **6**(1), pp. 13–20, 2007.

[19] Y. Tokura and S. Seki, "Multiferroics with Spiral Spin Orders," *Advanced Materials* **22**(14), pp. 1554–1565, 2010.

[20] R. Ramesh and N. A. Spaldin, "Multiferroics: progress and prospects in thin films," *Nature Materials* **6**(1), pp. 21–9, 2007.

[21] T. Kimura and Y. Tokura, "Magnetoelectric phase control in a magnetic system showing cycloidal/conical spin order," *Journal of Physics: Condensed Matter* **20**(43), p. 434204, 2008.

[22] Y. Yamasaki, S. Miyasaka, Y. Kaneko, J.-P. He, T. Arima, and Y. Tokura, "Magnetic Reversal of the Ferroelectric Polarization in a Multiferroic Spinel Oxide," *Physical Review Letters* **96**, p. 207204, May 2006.

[23] Y. J. Choi, J. Okamoto, D. J. Huang, K. S. Chao, H. J. Lin, C. T. Chen, M. van Veenendaal, T. A. Kaplan, and S.-W. Cheong, "Thermally or Magnetically Induced Polarization Reversal in the Multiferroic $CoCr_2\mathbf{O}_4$," *Physical Review Letters* **102**, p. 067601, Feb 2009.

[24] K. Tomiyasu, J. Fukunaga, and H. Suzuki, "Magnetic short-range order and reentrant-spin-glass-like behavior in $CoCr_2O_4$ and $MnCr_2O_4$ by means of neutron scattering and magnetization measurements," *Physical Review B* **70**, p. 214434, Dec 2004.

[25] S. Bordács, D. Varjas, I. Kézsmárki, G. Mihály, L. Baldassarre, A. Abouelsayed, C. A. Kuntscher, K. Ohgushi, and Y. Tokura, "Magnetic-Order-Induced Crystal Symmetry Lowering in $A\mathrm{Cr_2O_4}$ Ferrimagnetic Spinels," *Physical Review Letters* **103**, p. 077205, Aug 2009.

[26] S. Yang, H. X. Bao, D. Z. Xue, C. Zhou, J. H. Gao, Y. Wang, J. Q. Wang, X. P. Song, Z. B. Sun, X. B. Ren, and K. Otsuka, "Magnetodielectric effect from the onset of ferrimagnetic transition in $\mathrm{CoCr_2O_4}$," *Journal of Physics D: Applied Physics* **45**(26), p. 265001, 2012.

[27] G. Lawes, B. Melot, K. Page, C. Ederer, M. A. Hayward, T. Proffen, and R. Seshadri, "Dielectric anomalies and spiral magnetic order in $\mathrm{CoCr_2O_4}$," *Physical Review B* **74**, p. 024413, Jul 2006.

[28] K. Singh, A. Maignan, C. Simon, and C. Martin, "$\mathrm{FeCr_2O_4}$ and $\mathrm{CoCr_2O_4}$ spinels: Multiferroicity in the collinear magnetic state?," *Applied Physics Letters* **99**(17), pp. –, 2011.

[29] N. Mufti, A. A. Nugroho, G. R. Blake, and T. T. M. Palstra, "Magnetodielectric coupling in frustrated spin systems: the spinels $\mathrm{MCr_2O_4}$ (M = Mn, Co and Ni)," *Journal of Physics: Condensed Matter* **22**(7), p. 075902, 2010.

[30] K. R. Choi, S. J. Moon, T. Kouh, I. B. Shim, S. J. Kim, and C. S. Kim, "Characterization of $\mathrm{CoCr_2O_4}$ on $\mathrm{Pt(111)}$ Grown by Using Pulsed Laser Deposition," *IEEE Transactions on Magnetics* **45**, pp. 2610–2612, June 2009.

[31] X. Liu, M. Kareev, Y. Cao, J. Liu, S. Middey, D. Meyers, J. W. Freeland, and J. Chakhalian, "Electronic and magnetic properties of (1 1 1)-oriented $\mathrm{CoCr_2O_4}$ epitaxial thin film," *Applied Physics Letters* **105**(4), pp. –, 2014.

[32] V. Tsurkan, S. Zherlitsyn, S. Yasin, V. Felea, Y. Skourski, J. Deisenhofer, H.-A. K. von Nidda, J. Wosnitza, and A. Loidl, "Unconventional Magnetostructural Transition in $\mathrm{CoCr_2O_4}$ at High Magnetic Fields," *Physical Review Letters* **110**, p. 115502, Mar 2013.

[33] N. Vlietstra, J. Shan, B. J. van Wees, M. Isasa, F. Casanova, and J. Ben Youssef, "Simultaneous detection of the spin-Hall magnetoresistance and the spin-Seebeck effect in platinum and tantalum on yttrium iron garnet," *Physical Review B* **90**, p. 174436, Nov 2014.

[34] M. Schreier, N. Roschewsky, E. Dobler, S. Meyer, H. Huebl, R. Gross, and S. T. B. Goennenwein, "Current heating induced spin Seebeck effect," *Applied Physics Letters* **103**(24), pp. –, 2013.

[35] Y.-T. Chen, S. Takahashi, H. Nakayama, M. Althammer, S. T. B. Goennenwein, E. Saitoh, and G. E. W. Bauer, "Theory of spin Hall magnetoresistance," *Physical Review B* **87**, p. 144411, Apr 2013.

[36] X. Jia, K. Liu, K. Xia, and G. E. W. Bauer, "Spin transfer torque on magnetic insulators," *Europhysics Letters* **96**, p. 17005, Oct. 2011.

[37] Y. Shiomi and E. Saitoh, "Paramagnetic Spin Pumping," *Physical Review Letters* **113**, p. 266602, Dec 2014.

[38] Y. Ohnuma, H. Adachi, E. Saitoh, and S. Maekawa, "Spin Seebeck effect in antiferromagnets and compensated ferrimagnets," *Physical Review B* **87**, p. 014423, Jan 2013.

[39] S. Geprägs, A. Kehlberger, F. D. Coletta, Z. Qiu, E.-J. Guo, T. Schulz, C. Mix, S. Meyer, A. Kamra, M. Althammer, H. Huebl, G. Jakob, Y. Ohnuma, H. Adachi, J. Barker, S. Maekawa, G. E. W. Bauer, E. Saitoh, R. Gross, S. T. Goennenwein, and M. Kläui, "Origin of the spin seebeck effect in compensated ferrimagnets," *Nature Communications* **7**, p. 10452, 2016.

[40] J. Barker, "Atomistic spin simulations of the spin Seebeck effect," *Atomistic spin simulations of the spin Seebeck effect, unpublished* , 2015.

[41] K. Uchida, T. Kikkawa, A. Miura, J. Shiomi, and E. Saitoh, "Quantitative Temperature Dependence of Longitudinal Spin Seebeck Effect at High Temperatures," *Physical Review X* **4**, p. 041023, Nov 2014.

[42] D. Kamenskyi, H. Engelkamp, T. Fischer, M. Uhlarz, J. Wosnitza, B. P. Gorshunov, G. A. Komandin, A. S. Prokhorov, M. Dressel, A. A. Bush, V. I. Torgashev, and A. V. Pronin, "Observation of an intersublattice exchange magnon in $CoCr_2O_4$ and analysis of magnetic ordering," *Physical Review B* **87**, p. 134423, Apr 2013.

[43] V. I. Torgashev, A. S. Prokhorov, G. A. Komandin, E. S. Zhukova, V. B. Anzin, V. M. Talanov, L. M. Rabkin, A. A. Bush, M. Dressel, and B. P. Gorshunov, "Magnetic and dielectric response of cobalt-chromium spinel $CoCr_2O_4$ in the terahertz frequency range," *Physics of the Solid State* **54**(2), pp. 350–359, 2012.

[44] S. R. Marmion, M. Ali, M. McLaren, D. A. Williams, and B. J. Hickey, "Temperature dependence of spin Hall magnetoresistance in thin YIG/Pt films," *Physical Review B* **89**, p. 220404, Jun 2014.

[45] S. Meyer, M. Althammer, S. Geprägs, M. Opel, R. Gross, and S. T. B. Goennenwein, "Temperature dependent spin transport properties of platinum inferred from spin hall magnetoresistance measurements," *Applied Physics Letters* **104**(24), pp. –, 2014.

4

To be published as: A. Aqeel, N. Vlietstra, A. Roy, M. Mostovoy, B. J. van Wees, and T. T. M. Palstra – *"Electrical detection of spiral spin structures in Pt|Cu_2OSeO_3 heterostructures,"* Phys. Rev. B **94**, 134418 (2016).

Chapter 5

Electrical detection of spiral spin structures in Pt|Cu_2OSeO_3 heterostructures

Abstract

We study the spin-Hall magnetoresistance (SMR) and spin Seebeck effect (SSE) in a non-collinear insulating magnet-Pt heterostructure. We show that SMR can be used as an all-electric probe of complex spin states exhibited by the chiral magnet, Cu_2OSeO_3, under an applied magnetic field. The slope of the magnetic field dependence of the SMR signal changes sign at the transition between the helical and conical spiral states and shows another discontinuity when the conical spiral turns into a collinear ferromagnetic state. We demonstrate that the amplitude of the SMR signal is controlled by the cone angle, θ, and that it changes sign at $\theta \sim 55^\circ$. The angular dependence of the SMR in the multidomain helical spiral state is markedly different from the simple sinusoidal dependence observed in the monodomain conical spiral and ferromagnetic states. This complex behavior is explained within the framework of the SMR theory initially developed for collinear magnets. The SSE displays unconventional behavior where not only the magnitude but also the phase of the angular dependence of the SSE varies with the applied magnetic field.

5.1 Introduction

The coupling of magnetization to spin, charge, and heat currents in insulating magnet-metal heterostructures is intensively studied in the context of energy-efficient spintronic applications [1–3]. This coupling gives rise to a number of phenomena playing a fundamental role in the field of spintronics, such as spin-transfer torque [2, 4, 5], spin pumping [6, 7], spin-Hall magnetoresistance (SMR) [8–10], and spin Seebeck effect (SSE) [11–13]. These effects, in particular SMR and SSE, can in principle be used to probe the magnetization of an insulating magnetic layer by purely electric measurements [14, 15]. Studies thus far have mainly focused on materials with simple collinear magnetic orders, and the attempts to study non-collinear magnets did not provide detailed information on their magnetic structures [14–16]. Apart from SMR, the SSE also has been recently used to identify the spin-flop transition in antiferromagnets [17, 18]. Magnetic states with non-collinear and even non-coplanar spins,

varying at a length scale of tens of nanometers, are found in chiral magnets, whose crystal lattice lacks inversion symmetry. These complex spin structures are usually studied by sophisticated methods, e.g., spin-polarized neutron scattering [19, 20], muon spectroscopy [21], or Lorentz transmission electron microscopy [22]. The measurements of transport in magnet|metal heterostructures probe the magnetization distribution at the interface and thus provide 'holographic' information about three-dimensional magnetic orders. Here we show that with some prior knowledge about magnetic states, the SMR measurements can be an effective tool for all-electric detection and study of complex spin textures.

In this chapter, we report a systematic study of the excitation and detection of spin currents in the spin spiral magnet Cu_2OSeO_3 using the SMR and SSE. Cu_2OSeO_3 (CSO) belongs to the family of cubic chiral magnets [23], including MnSi, $Fe_{0.5}Co_{0.5}Si$, and FeGe, in which magnetic skyrmions have been found recently [24]. Unlike the itinerant magnet MnSi, CSO is a large band gap Mott insulator [25]. Yet the magnetic phase diagram of CSO, showing a variety of non-collinear spin states (see Fig. 5.1(a)), is similar to those of other cubic chiral magnets. At low applied magnetic fields CSO is in an incommensurate helical spiral state with a long period of $\sim$50 nm [22] stabilized by the relativistic Dzyaloshinskii-Moriya interaction [26]. In this multidomain state the spiral wave vector $\boldsymbol{Q}$ can be oriented along any of the three equivalent directions: [100], [010] or [001] [20]. Above the critical field, H_{c1}, a transition into a conical spiral state occurs, in which $\boldsymbol{Q} \parallel \boldsymbol{H}$. As the field increases, the cone angle θ becomes smaller. Eventually, θ becomes zero at the second critical field, H_{c2}, which marks the transition to the field-induced collinear ferrimagnetic (FM) state. The evolution of the magnetic structure of CSO under an increasing magnetic field is depicted in Figs. 5.1(b-g). Here, we investigated these magnetic structures of CSO electrically by using the SMR and SSE.

The underlying physics of the SMR and SSE phenomena hinges on the conversion between charge and transverse spin currents – the spin Hall effect (SHE) and its inverse (ISHE) [27–29]. In the SMR, both the SHE and ISHE play a concerted role, whereas in the SSE, thermal gradients across an interface result in a magnonic spin current, detected electrically by the ISHE. The SMR is an interface effect [14, 30, 31], whereas the SSE is explained as a bulk effect in which thermal magnons play an important role [32–34]. These effects are used here as a pathway for the electrical detection of non-collinear nanomagnetic spin textures like spirals and helices in a CSO magnet.

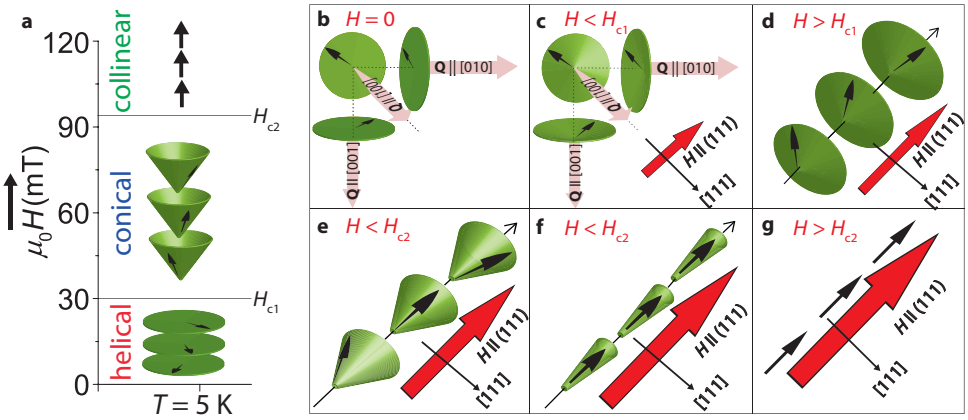

Figure 5.1: *(a) A schematic illustration of the magnetic phase diagram of CSO as a function of applied magnetic field at 5 K. Here H_{c1} and H_{c2} represent the fields at which the magnetic transitions occur. At H_{c1}, the helical state with three magnetic domains converts to a single-domain conical state oriented along $\boldsymbol{H}$. At H_{c2}, conical to collinear ferrimagnetic transition occurs. (b-g) Transformation of different magnetic spin structures present in CSO under an increasing applied magnetic field. The transformation is from (b,c) helical to (d-f) conical and then to (g) the FM state. Here, round brackets ( ) and square brackets [ ] indicate the planes and directions of the unit cell, respectively.*

5.2 Experimental procedure

High quality CSO single crystals were grown by a chemical vapor transport method [35] with typical sizes of 20-50 mm^3. The crystal structure was characterized by a Bruker D8 Venture single crystal x-ray diffractometer. The magnetization of the crystals was measured by a SQUID magnetometer. Before device fabrication, the crystal surfaces were oriented along the (111) surface and polished to obtain the smallest surface roughness (see Appendix 5.5.1).

Two devices (S1 and S2) on two individually polished (111) crystal surfaces (dimensions $\approx$ 4mm $\times$ 4mm $\times$ 2mm) were prepared. The Hall-bar device patterns were defined using three e-beam lithography steps, each followed by a standard deposition and a lift-off procedure. The first step produces a Ti/Au (5/40 nm) marker pattern, used to align the subsequent steps. The second step defines the platinum Hall-bar structure (5 nm), deposited by DC sputtering. The third step defines Ti/Au (5/80 nm) leads and bonding pads also deposited by DC sputtering in an Ar^+ plasma at an argon pressure of 3.3 $\times$ 10^3 mbar, and the thickness in each step

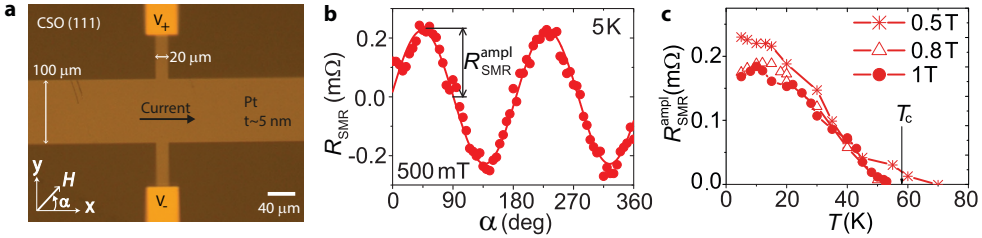

Figure 5.2: *(a) Optical image showing the Hall-bar structure with 5 nm-thick Pt deposited on a CSO crystal. (b) Angular dependence of the SMR signal, R_{SMR}, measured by contacting the Hall-bar structure as marked in (a). The solid line shows a $\sin(2\alpha)$ fit. In this plot the signals caused by the ordinary Hall effect have been subtracted. (c) Temperature dependence of the SMR signal $R_{\mathrm{SMR}}^{\mathrm{ampl}}$ at several magnetic field strengths. Data are acquired for device S1.*

is measured by atomic force microscopy.

All measurements were carried out in the transverse configuration, as marked in Fig. 5.2(a), by using two Stanford SR-830 lock-in amplifiers set at a reference frequency of 17 Hz (see Appendix 5.5.1). The lock-in amplifiers are used to measure the first and second harmonic signals. The same lock-in amplifiers are used to check third and fourth harmonic signals, at selected field and temperature regions. The current (ranged from 1 to 4 mA) was sent to the sample using a custom-built current source, and the response signal was recorded using a custom-built pre-amplifier (gain 10^2-10^3), before sending it back to the lock-in amplifier. All measurements were performed in a quantum design Physical Properties Measurement System (PPMS). The sample was rotated in the superconducting magnet of the PPMS with the stepper motor, such that the magnetic field varies in the plane of the sample as shown in Fig 5.2(a) with an optical microscope image of the device.

5.3 Results and discussion

5.3.1 Spin-Hall magnetoresistance

When a charge current I is sent through a Pt strip, the SHE generates a transverse spin current. This spin current results in a spin accumulation $\boldsymbol{\mu}_s$ at the Pt|CSO interface. This spin accumulation $\boldsymbol{\mu}_s$ can be absorbed or reflected at the interface depending on the direction of the magnetization $\boldsymbol{M}$ of CSO. When $\boldsymbol{\mu}_s \perp \boldsymbol{M}$, the electron spins arriving at the Pt|CSO interface will be partially absorbed, and when $\boldsymbol{\mu}_s \parallel \boldsymbol{M}$, spins will be fully reflected. The reflected spins generate an additional charge current by the ISHE. When $\boldsymbol{M}$ makes an angle with $\boldsymbol{\mu}_s$, this additionally generated charge current also has a component pointing in the transverse direction resulting in

the transverse SMR response. Therefore, we expect to observe a dependence of the transverse Pt resistance on α, the angle between the applied current and the in-plane external magnetic field $\boldsymbol{H}$ that orients $\boldsymbol{M}$. We perform all transport measurements as a function of α, by rotating the device in a fixed field $\boldsymbol{H}$. Because the change in the SMR voltage scales linearly with I, it can be detected by the first harmonic voltage response of the lock-in amplifier. Here, the SMR signal is shown after subtraction of an additional signal due to the ordinary Hall effect (see Appendix 5.5.2 for details). The result of such a measurement is shown in Figs. 5.2(b) and 5.3(a). It clearly shows the $\sin(2\alpha)$ angular dependence expected for the collinear FM state [30]. We measured the angular dependence of the SMR at different temperatures in the FM state ($H > H_{c2}$) and observed a maximum SMR response around 5 K (see Fig. 5.2(c)). In order to explore the SMR response in different magnetic states of CSO, we set the temperature to 5 K and measured the angular dependence of the SMR for different external magnetic field strengths.

The angular dependence of the SMR in the conical spiral state is close to the $\sin(2\alpha)$ dependence observed at high fields and shows the presence of higher harmonics close to the transition to the helical state (see Figs. 5.3(b,c)). The most prominent feature is the change of the sign of the amplitude of the SMR, $R_{\mathrm{SMR}}^{\mathrm{ampl}}$, in the conical spiral phase (cf. Fig. 5.3(a) with Figs. 5.3(b,c)): $R_{\mathrm{SMR}}^{\mathrm{ampl}}$ increases with field from a negative value at H_{c1} to a positive value at H_{c2}. It changes sign at $\mu_0 H \sim 60$ mT (see Fig. 5.3(e)). In the helical state, amplitude $R_{\mathrm{SMR}}^{\mathrm{ampl}}$ is negative: it equals zero in zero field and decreases with applied field. The angular dependence of the SMR in the helical state has sharp discontinuities and deviates strongly from the sinusoidal dependence (see Fig. 5.3(d)).

This observed behavior can be understood as follows. For collinear magnets [30], $R_{\mathrm{SMR}} \propto m_x\, m_y$, where m_x and m_y are the in-plane components of the magnetization unit vector $\boldsymbol{m}$, parallel and orthogonal to the current direction, respectively. Since the spin relaxation length $\lambda \sim 2$ nm in Pt is much smaller than the spiral period ~ 50 nm in CSO, this expression is valid *locally* for CSO. The SMR for the non-collinear magnet is obtained by averaging $m_x m_y$ over the interface:

$$R_{\mathrm{SMR}} \propto \langle m_x m_y \rangle \tag{5.1}$$

In the conical spiral phase

$$\boldsymbol{m} = \cos\theta \boldsymbol{e}_3 + \sin\theta(\boldsymbol{e}_1 \cos \boldsymbol{Q}\cdot\boldsymbol{x} + \boldsymbol{e}_2 \sin \boldsymbol{Q}\cdot\boldsymbol{x}) \tag{5.2}$$

where $\boldsymbol{e}_1, \boldsymbol{e}_2$ and $\boldsymbol{e}_3$ are three mutually orthogonal unit vectors and θ is the cone angle. In the conical spiral state, both $\boldsymbol{e}_3$ and $\boldsymbol{Q}$ are parallel to the applied magnetic field, $\boldsymbol{H}$. Using equation (5.2), we obtain

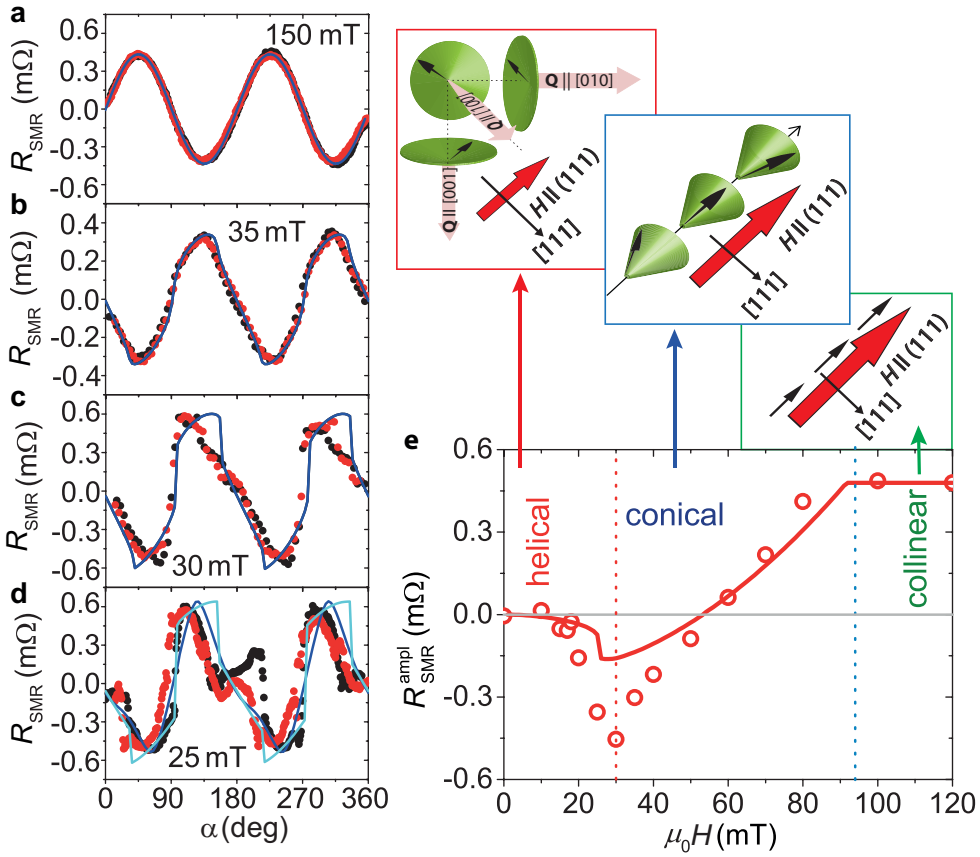

Figure 5.3: *(a-d) Angular dependence of the SMR (R_{SMR}) at 5 K in different magnetic states of CSO. R_{SMR} in (a) the collinear ferrimagnetic, (b,c) conical, and (d) helical magnetic states of CSO. The black and red data points show the trace and retrace measurements, respectively, showing hysteresis at low applied magnetic fields. The solid curves fit to the data using the conical spiral ansatz (equation 5.2) (see Appendix 5.5.3 for details). The data are centered around zero and acquired for device S2. A more detailed evolution of the SMR signal can be found in Fig. 5.8. (e) Field dependence of the SMR signal, $R_{\mathrm{SMR}}^{\mathrm{ampl}}$ for the various magnetic orders which develop in CSO with increasing magnetic field. Here, **Q** represents the propagation wave vector, and the magnetic field **H** is applied in the (111) plane parallel to the Pt|CSO interface. The transition between the different magnetic states of the CSO crystal is marked by vertical lines. The red line is the calculated amplitude of the SMR.*

$$\langle m_x m_y \rangle = \frac{1}{4} \sin 2\alpha (3\cos^2\theta - 1) \tag{5.3}$$

which explains the (nearly) sinusoidal α dependence of SMR in the conical spiral state. In addition, $\cos\theta = \frac{H}{H_{c2}}$ (see Appendix 5.5.3), so that $R_{\mathrm{SMR}}^{\mathrm{ampl}} \propto 3\left(\frac{H}{H_{c2}}\right)^2 - 1$ increases with the magnetic field and changes sign at $H = \frac{H_{c2}}{\sqrt{3}}$, in good agreement with the experimental observations. The negative R_{SMR} close to H_{c1} follows from the fact that for $\theta \sim 90^\circ$ spins in the conical spiral are nearly orthogonal to the magnetic field direction. Furthermore R_{SMR} remains constant for $H > H_{c2}$, as in the collinear phase $\theta = 0$, regardless of the applied field strength.

The spin structure of the helical spiral state is more complex because of the deformation of the helix in an applied magnetic field and the presence of domains with different orientations of $\boldsymbol{Q}$. The angular and field dependence of the observed SMR can be qualitatively understood using equation (5.2), in which $\boldsymbol{e}_3$ and $\boldsymbol{Q}$ are not necessarily parallel to the field direction. Their orientations and the angle θ in each domain are found by numerical minimization of energy for a given applied field H (see Appendix 5.5.3). We then added the contributions of the three domains. The result (blue line in Fig. 5.3), fits well the angular dependence of the observed SMR. Also the magnetic field dependence of the SMR in the helical state is qualitatively similar to our experimental observations: $R_{\mathrm{SMR}} = 0$ at zero field due to cancellation of the contributions of the three domains (see Fig. 5.8(i)). It is negative at nonzero fields because θ is close to 90°, and it decreases with the applied magnetic field because of the reorientation of $\boldsymbol{e}_3$ and $\boldsymbol{Q}$.

5.3.2 Spin Seebeck effect

In addition to the linear response of the SMR, the SSE due to Joule heating (for which $\Delta T \propto I^2$) is also observed in the second harmonic response. In the SSE, thermally excited magnons spin polarize the electrons close to the interface, which is detected electrically by the ISHE (shown schematically in Fig. 5.4(c). As the generated spin accumulation is polarized along $\boldsymbol{M}$, the SSE/ISHE signal shows a $\cos(\alpha)$ dependence by rotating $\boldsymbol{M}$, with a full 360° period. The SSE signal is shown in Fig. 5.4(a) in which an additional nonzero phase φ appears resulting in a $\cos(\alpha + \varphi)$ periodicity with an amplitude $R_{\mathrm{SSE}}^{\mathrm{ampl}}$. Both the amplitude $R_{\mathrm{SSE}}^{\mathrm{ampl}}$ and phase φ vary with H (see Fig. 5.4(b)).

The appearance of a nonzero φ in the angular dependence of the SSE signal suggests that the bulk magnetization of CSO is not fully aligned along $\boldsymbol{H}$. When the magnetization is fully aligned along $\boldsymbol{H}$ (which ideally would be the case for the collinear ferrimagnetic state), we expect $\varphi = 0^\circ$. Fig. 5.4(d) shows that $R_{\mathrm{SSE}}^{\mathrm{ampl}}$ increases with decreasing temperature and is observed to have maximum around 5 K (see Appendix 5.5.4 for a plausible explanation). Fig. 5.4(e) shows the field dependence of $R_{\mathrm{SSE}}^{\mathrm{ampl}}$ at 5 K. The amplitude $R_{\mathrm{SSE}}^{\mathrm{ampl}}$ is zero for $\mu_0 H = 0$ T due to the absence

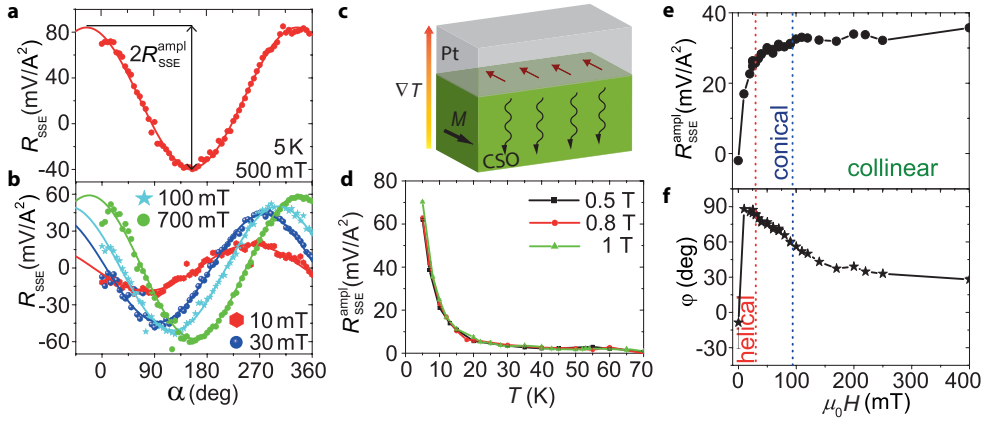

Figure 5.4: *(a,b) Angular dependence of the SSE signal (R_{SSE}) in the Pt|CSO in different applied magnetic field strengths. The solid lines show the* $\cos(\alpha + \varphi)$ *fits. (c) A schematic illustration of the SSE measured in the second harmonic response. The SSE is created by a current-induced thermal gradient* ∇T *across the Pt|CSO interface, generating magnons into the CSO crystal. The magnons create a spin accumulation close to the interface along the magnetization* $\boldsymbol{M}$ *of CSO. This spin accumulation is detected electrically by ISHE, resulting the SSE signal. (d) Temperature dependence of the SSE signal,* $R_{\mathrm{SSE}}^{\mathrm{ampl}}$ *for different applied magnetic field strengths. (e) Amplitude* $R_{\mathrm{SSE}}^{\mathrm{ampl}}$ *and (f) phase* φ *of the SSE signal as a function of applied magnetic field at 5 K, respectively. The shown data are acquired for device S1 and for device S2 summarized in Fig. 5.10.*

of net magnetization in the helical spiral state. $R_{\mathrm{SSE}}^{\mathrm{ampl}}$ grows much faster with the applied field in the helical phase than in the conical phase (see Fig. 5.4(e)), which may be attributed to the fact that the wave vector of the helical spiral has a component normal to the interface (along the [111] direction), resulting in cancellation of the SSE signal sensitive to the in-plane component of the magnetization. $R_{\mathrm{SSE}}^{\mathrm{ampl}}$ continues to grow with the field in the ferrimagnetic state, reaching the saturation at $\mu_0 H = 4$ T and has the same sign as reported in the literature [15] (see Appendix 5.5.4 for details). Still, the weak field dependence of $R_{\mathrm{SSE}}^{\mathrm{ampl}}$ in the conical spiral phase is puzzling in view of the nearly linear dependence of the average magnetization on H. Another puzzle is the field dependence of the phase φ, which is $\sim 90°$ at low fields, decreases with increasing field and $\sim 5°$ in the field of 1 T (see Fig. 5.4(f)).

5.4 Conclusion

In conclusion, we demonstrated that the SMR can be used for electric detection of transitions between complex spin states, such as the helical spiral and conical spi-

ral phases of CSO. This technique was proved to be sensitive to the orientation of the spiral wave vector and to the magnitude of the cone angle. Our observation of the nonsinusoidal angular dependence of the SMR in the multidomain helical spiral state and of the sign reversal of the SMR amplitude in the conical spiral state opens opportunities for developing novel spintronic devices based on this magnetoresistance effect. The observed complex angular and magnetic field dependence of the SMR is described remarkably well by our simple model of CSO. The SSE also shows strong sensitivity to changes in magnetic ordering of CSO, although its origin remains unclear. It will be interesting to apply these techniques to the detection of even more complex spin textures, such as the skyrmion crystal. Since the skyrmion crystal phase in bulk materials only appears at elevated temperatures, the SMR detection of the skyrmion crystal requires a substantial lowering of the noise level. A technique, with which one can observe nanosized objects by measuring electric currents, would be indispensable for utilizing skyrmions and other topological defects as information carriers in next generation spintronics devices.

5.5 Appendix

5.5.1 Sample characteristics and measurement technique

In this section we provide additional information on the material properties and the device fabrication of the Pt|CSO heterostructure. Firstly, the crystals were oriented with a single crystal x-ray diffractometer by focusing the x-ray beam on one corner. The Bruker Apex II software was used to rotate the goniometer such that the crystals were aligned along the [111] direction by using the orientation matrix obtained by collecting a dataset over a limited angular range. Some part of the crystals along the (111) plane was lapped away and then the (111) surfaces were polished in the following manner.

The crystals were first slightly grinded with abrasive grinding papers (SiC P1200 - SiC P4000) by hand. After grinding, diamond particles were used with a sequence of 9 μm, 3 μm and 1 μm at 200 rpm (starting from slower speed of 100 rpm) for 15 minutes, respectively. After each polishing step the crystals were cleaned with ethanol and acetone. As a final polishing step, the surfaces were polished with colloidal silica OPS (oxide polishing suspension) with a particle size of 40 nm for 15 min. After polishing with silica particles, the crystals were quickly rinsed in water before drying. Then the crystals were cleaned with acetone and ethanol in an ultrasonic bath. We investigated two devices, S1 and S2, fabricated in the same way but on two individually polished crystal surfaces.

To measure the SMR and SSE simultaneously, we used a lock-in detection tech-

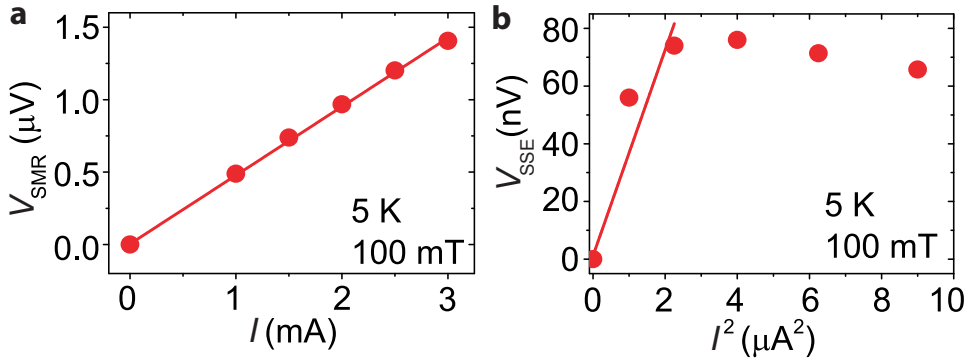

Figure 5.5: *(a) Current dependence of the first harmonic contribution V_{SMR} due to spin-Hall magnetoresistance, where I is the AC current sent through the Pt Hall-bar. (b) Second harmonic signal V_{SSE} due to the spin Seebeck effect as a function of I^2, generated by current induced heating. Here, the solid lines indicate the linear fits.*

nique [8]. By using this technique, we measured the SMR as first and the SSE as second order responses of the Pt|CSO system by sending an applied AC current ($I \leq 4$ mA) through the Pt Hall-bar. The output voltage signal can be written as the sum of the first, second and higher order responses of I as follows:

$$V(t) = R_1 I(t) + R_2 I^2(t) + R_3 I^3(t) + R_4 I^4(t) + \cdots , \tag{5.4}$$

To measure the first and second order resistance response, we measured the individual harmonic voltages by using lock-in amplifiers. When considering only first and second harmonic voltage signals, the first and second order resistance responses are defined as follows:

$$\begin{array}{c} R_1 = \frac{V_1}{I_0} \\ R_2 = \sqrt{2}\frac{V_2}{I_0^2} \end{array} \quad \text{for} \quad \begin{array}{c} \phi = 0^{\mathrm{o}} \\ \phi = -90^{\mathrm{o}} \end{array} \tag{5.5}$$

As the SSE is measured as second order resistance response, we defined here $V_2 = V_{\mathrm{SSE}}$ and $R_2 = R_{\mathrm{SSE}}$. To check the contribution from the higher harmonic responses, we also measured third and fourth harmonic signals at $I = 4$ mA in different applied magnetic fields. We observed these signals to be negligible compared to the detected first and second harmonic signals. Therefore these higher harmonic signals do not have to be taken into account for the calculation of the first and second order response of the system [8]. In the linear response regime $I < 2$ mA, the SMR scales linearly and the SSE scales quadratically with the applied current as shown in Fig. 5.5(a,b). However, at $I \geq 2$ mA, the SSE no longer follows the expected quadratic trend. Nevertheless, we measured the SMR and SSE also by sending higher currents

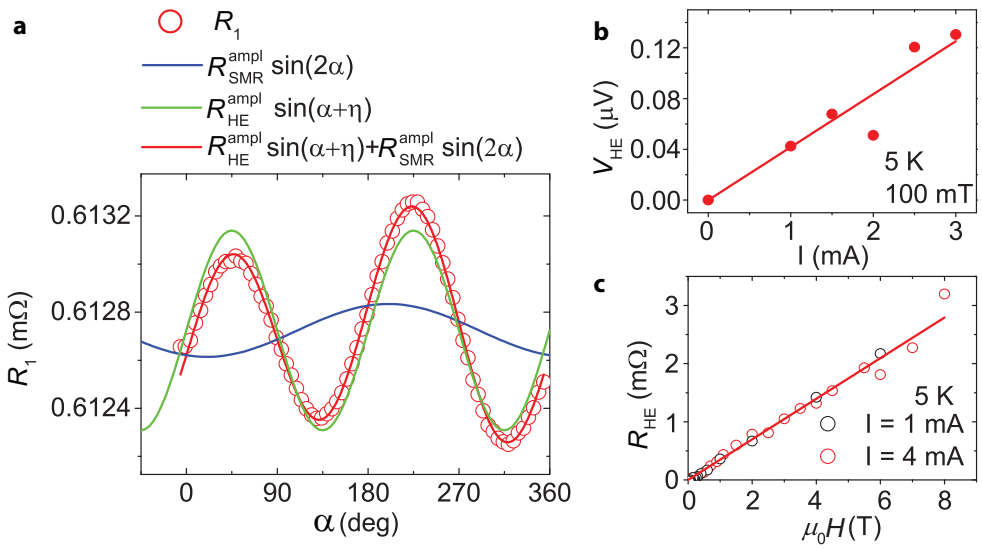

Figure 5.6: *(a) The angular dependence of the first order resistance response in the transverse configuration, $R_1 = V_1/I$, for $I = 4$ mA at 5 K in an applied magnetic field of 400 mT. The $R^{\mathrm{ampl}}_{\mathrm{SMR}} \sin(2\alpha)$ and $R^{\mathrm{ampl}}_{\mathrm{HE}} \sin(\alpha + \eta)$ curves illustrate the additive contributions from the expected SMR and an additional ordinary Hall effect signals. (b) The additional contribution in the first order resistance response R_{H} due to ordinary Hall effect scales linearly with the applied current. (c) R_{H}, as expected for the Hall effect, scales linearly with the applied magnetic field.*

till $I = 4$ mA. We observed a similar trend in the magnitude and phase change of the SSE at different currents (see Fig. 5.10(g,h)).

The angular dependence of the SMR and the SSE were studied by rotating an externally applied magnetic field in the xy plane of the CSO crystal [36]. The in-plane angle α of the magnetic field is defined relative to the applied current direction (x-axis) through the Pt Hall-bar, as indicated in Fig. 5.2(a).

5.5.2 First harmonic response in Pt on the Cu_2OSeO_3 crystal

Here we discuss on the identification of different contributions in the first harmonic response and the method adopted to separate the desired SMR contribution. We also discuss the influence of the applied magnetic field on the magnitude and the line shape of the angular dependence of the SMR signal, as an addition to the first part of the main text. The first order resistance response is determined by measuring the first harmonic voltage transverse to the applied current direction on the Hall-bar

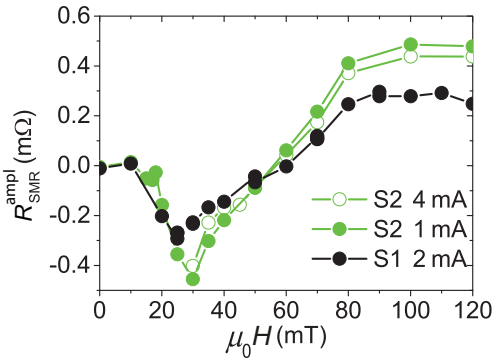

Figure 5.7: *The SMR signal as a function of external magnetic field for devices S1 ($I = 2$ mA) and S2 ($I = 1$ mA, 4 mA).*

structure, as described above. An example of such a measurement is shown by the red circles in Fig. 5.6(a).

For the SMR the measured Pt resistance depends on the direction of average magnetization M of CSO, as explained in the main text. Apart from the expected SMR, an additional signal due to the ordinary Hall effect (HE) is obserevd in R_1, which is generated by a magnetic field component normal to the (111) plane of the CSO crystal due to a slight misalignment of the sample by an angle estimated to be $\sim 2°$ and $\sim 4°$ for S1 and S2, respectively. The HE voltage has a $\sin(\alpha + \eta)$ angular dependence, where the phase η is governed by the sample tilt direction. The ordinary Hall voltage of Pt|CSO scales linearly with the applied current and magnetic field strength, as expected (see Fig. 5.6(b,c)).

Our results for both devices S1 and S2 are reconcilable, despite the fact that the magnitude of the signals for device S2 is almost twice higher (see Fig. 5.7), indicating that by optimizing the contact properties the signals could be enhanced further. Fig. 5.8 shows the summarized data of the SMR as a function of angle α acquired for device S2 at 5 K. As explained in the main text, the SMR signal in the ferrimagnetic phase ($\mu_0 H = 120$ mT) has a $\sin(2\alpha)$ dependence (see Fig. 5.8(a)). When the field is reduced below the ferrimagnetic transition, the amplitude of the SMR signal decreases (see Fig. 5.8(b,c)) with the same sign. At $\mu_0 H < 60$ mT, the SMR signal reverses its sign in the conical magnetic state of CSO (see Fig. 5.8(d)), a further decrease in magnetic field results in an increase of the amplitude of the SMR signal (see Fig. 5.8(e,f)). At the magnetic transition from the conical to the helical state of CSO, the line shape of the SMR signal starts to deviate from a $\sin(2\alpha)$ function (see Fig. 5.8(f,g)) and does not follow $\sin(2\alpha)$ dependence in the helical phase (see Fig. 5.8(h)). The SMR signal fully disappears at $\mu_0 H = 0$ T (see Fig. 5.8(i)).

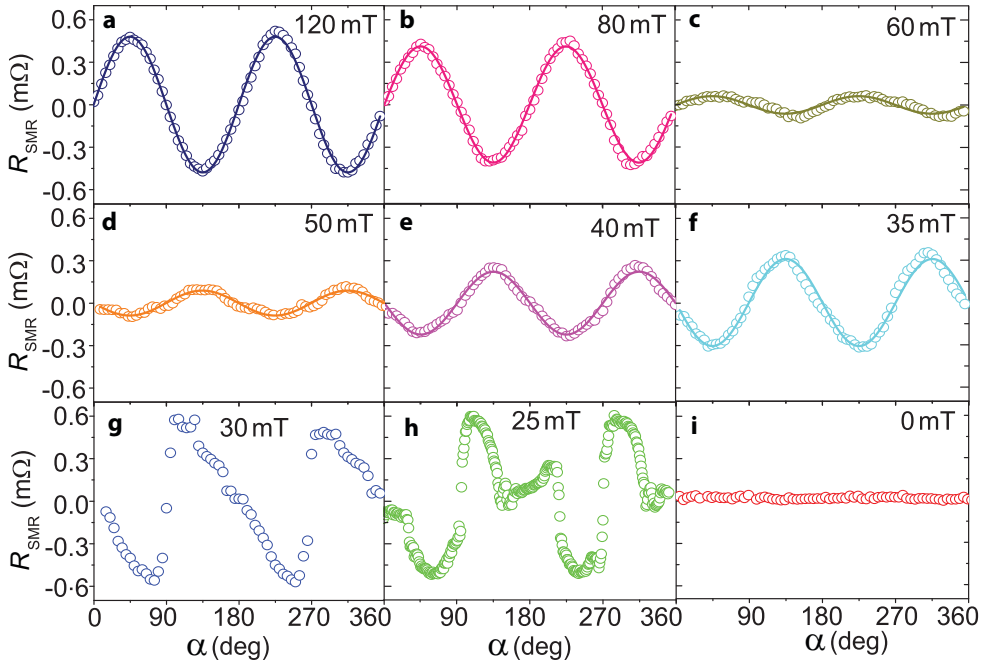

Figure 5.8: *(a-i) Change in the SMR signal R_{SMR} in Pt|CSO system by decreasing the applied magnetic field at current $I = 1$ mA, through the Pt Hall-bar at 5 K. The SMR signal (a) in the ferrimagnetic state of CSO, (b-f) in the conical magnetic state of CSO and (g-i) in the helical magnetic state of CSO. The data shown here are centered around zero and acquired for device S2.*

5.5.3 Continuum model for the SMR effect in Pt|Cu_2OSeO_3

We describe magnetic states of Cu_2OSeO_3 by the continuum model [26],

$$\varepsilon = \frac{J}{2a}\sum_i \partial_i \boldsymbol{m}\cdot\partial_i\boldsymbol{m} + \frac{D}{a^2}\boldsymbol{m}\cdot\boldsymbol{\nabla}\times\boldsymbol{m} - \mu_0\mu\boldsymbol{m}\cdot\boldsymbol{H} + \frac{K_1}{a^3}\sum_i m_i^4 + K_2 a\sum_i \partial_i^2\boldsymbol{m}\cdot\partial_i^2\boldsymbol{m}, \quad (5.6)$$

where the first term describes the FM exchange interaction, the second term is the Lifshitz invariant resulting from the Dzyaloshinskii-Moriya interaction and the third term is the Zeeman energy. The last two terms are the magnetic and spatial anisotropies allowed by the $P2_13$ symmetry of the crystal lattice, a is the lattice constant and

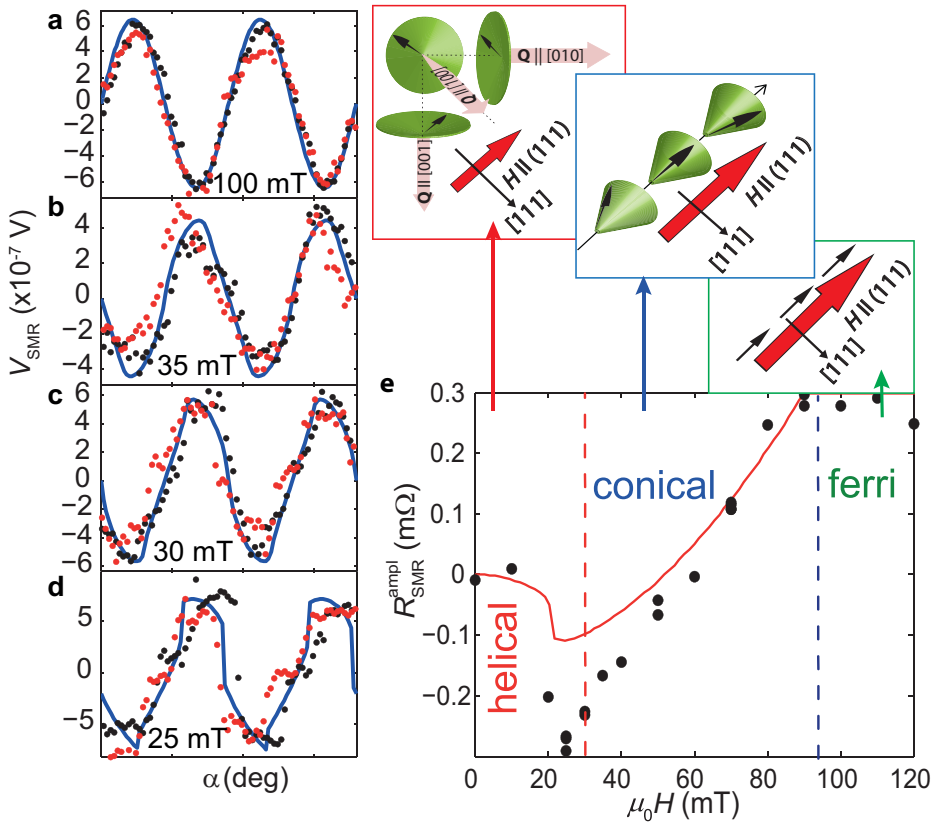

Figure 5.9: *(a-d) Angular dependence of the SMR (R_{SMR}) at 5 K in different magnetic states of CSO. R_{SMR} in (a) the collinear ferrimagnetic, (b) conical and (c,d) helical magnetic states of CSO. The black and red data points show the trace and retrace measurements, respectively, showing hysteresis at low applied magnetic fields. The data are centred around zero and acquired for device S1. The solid curves are model fits to the data. (e) Field dependence of the SMR signal, R^{ampl}_{SMR} for the various magnetic orders which develop in CSO with increasing magnetic field. Here, $\boldsymbol{Q}$ represents the propagation wave vector and the magnetic field $\boldsymbol{H}$ is applied in the (111) plane parallel to the Pt|CSO interface. The transition between the different magnetic states of the CSO crystal is marked by vertical lines. The data acquired for device S2 are presented in Fig. 5.3.*

$\partial_i = \frac{\partial}{\partial r_i}, i = x, y, z.$

Substituting equation 5.2 into the expression for the energy density equation (5.6),

we obtain

$$\begin{aligned}\varepsilon &= \left(\frac{JQ^2}{2a}+\frac{D}{a^2}\boldsymbol{e}_3\cdot\boldsymbol{Q}\right)\sin^2\theta-\mu_0\mu\cos\theta\boldsymbol{e}_3\cdot\boldsymbol{H}+\frac{K_1}{a^3}\\ &\left(A(\theta)+B(\theta)\sum_i e_{3i}^4\right)+\frac{1}{2}K_2a\sin^2\theta Q^2\\ &\sum_i\left(Q^2-e_{3i}^2Q_i^2\right)\end{aligned} \tag{5.7}$$

where $A(\theta)=3\sin^2\theta\left(\frac{1}{8}\sin^2\theta+\cos^2\theta\right)$ and $B(\theta)=\frac{3}{8}\sin^4\theta-3\sin^2\theta\cos^2\theta+\cos^4\theta$. We neglect the exchange anisotropy, $\frac{K_3}{a}\sum_i(\partial_i m_i)^2$, in equation (5.6), which reduces to $\frac{K_3}{2}\sin^2\theta\left(Q^2-(\boldsymbol{Q}\cdot\boldsymbol{e}_3)^2\right)$. Since $\boldsymbol{e}_3$ is (nearly) parallel to $\boldsymbol{Q}$ at all applied fields, this term has little effect on the magnetic state.

We first discuss the conical spiral state, in which $\boldsymbol{e}_3\parallel\boldsymbol{Q}\parallel\boldsymbol{H}$. Neglecting the relatively small anisotropy terms, we obtain $Qa=\frac{D}{J}$ by minimizing ε with respect to Q, while the minimization with respect to θ gives $\cos\theta=\frac{H}{H_{c2}}$, where $\mu_0\mu H_{c2}=\frac{D^2}{J}$.

The anisotropy terms are crucial for stabilization of the helical state. Due to the second term in equation (S3), $\boldsymbol{e}_3$ and $\boldsymbol{Q}$ are nearly parallel in the helical state. Then both anisotropic terms are, essentially, equivalent to $K'a\sum_i Q_i^4$, which for $K'<0$ favors the $[100],[010]$ and $[001]$ directions of the spiral wave vector. In an applied magnetic field the wave vector $\boldsymbol{Q}$, minimizing the energy of each domain, deviates from the corresponding crystallographic axis. K' determines the critical field, H_{c1}, at which the transition from the helical to conical spiral state occurs.

The observed vanishing of the SMR signal in zero field is explained as follows. In the domain α ($\alpha=1,2,3$), $\langle m_x m_y\rangle=\frac{1}{2}(\boldsymbol{e}_3^{(\alpha)}\cdot\hat{x})(\boldsymbol{e}_3^{(\alpha)}\cdot\hat{y})(3\cos^2\theta^{(\alpha)}-1)$, where $\hat{x}$ and $\hat{y}$ are the unit vectors in the x and y directions. In zero field, $\cos\theta^{(\alpha)}=0$ in all domains and $e_3^{(1)}=(1,0,0)$, $e_3^{(2)}=(0,1,0)$ and $e_3^{(3)}=(0,0,1)$. Adding the contributions of all three domains and assuming that they have the same volume, we obtain :
$-\frac{1}{6}\sum_\alpha(\boldsymbol{e}_3^{(\alpha)}\cdot\hat{x})(\boldsymbol{e}_3^{(\alpha)}\cdot\hat{y})=-\frac{1}{6}(\hat{x}\cdot\hat{y})=0$.

Blue lines in figures 3a-d are the angular dependence of the SMR in different magnetic states of CSO obtained by numerical minimization of the energy (S3) with respect to $\boldsymbol{Q}$ and $\boldsymbol{e}_3$, for $K_1=0$ and $K_2=0.07J$. To reproduce the angular dependence of the multidomain helical state (Fig. 5.3(d)), we used two assumptions: (1) the three domains with different orientations of the spiral wave vector $\boldsymbol{Q}$ have the same volume (dark blue line) and (2) the domain with the lowest energy for a given $\boldsymbol{H}$ occupies the whole sample (light blue line). Red line Fig. 5.3(e) shows the magnetic field dependence calculated for the same set of parameters. The model captures nicely all the essence of the data and correctly gives the value of the field at which the amplitude of the SMR changes sign. The calculated amplitude of the SMR at low fields is, however, smaller than that observed in our experiment.

5.5.4 Second harmonic response in Pt|Cu_2OSeO_3

As shown in Fig. 5.4(d), the SSE increases by decreasing the temperature below T_c, with a maximum signal observed at 5 K. The temperature dependence of the SSE resembles closely the temperature dependence observed in a frustrated magnetic system [15] and therefore can be explained in a similar way, by considering different sublattices. The associated acoustic (ferromagnetic) and optical (antiferromagnetic) modes of different sublattices do not contribute to the SSE with the same sign and cancel to a large extent for temperatures close to T_c. By decreasing temperature below T_c, the exchange splitting of the optical modes increases and they become increasingly depleted. The suppression of the thermal pumping of the optical modes in the Pt|CSO sample thus leads to an apparent enhancement of the SSE at lower temperatures. This mechanism explains the low-temperature sign change of the SSE of the ferrimagnetic insulator $Gd_3Fe_5O_{12}$ (GdIG) [37]. It also accounts for the apparent suppression of the SSE in YIG at temperatures above 300 K [38] and the enhancement in the SSE at low temperatures $T < T_c$ in a non-collinear magnetic insulator, $CoCr_2O_4$ [15]. A full theoretical modeling and interpretation is possible by considering the atomistic spin models although this is beyond the scope of this work.

As shown in Fig. 5.4(b,f) for device S1 and in Fig. 5.10 for device S2, the SSE detected as the second harmonic response changes phase as well as magnitude upon decreasing the applied magnetic field (see Fig. 5.10) and at $\mu_0 H = 1$ T the phase φ is observed to be around 5°. When the magnetic field is reduced further, the phase φ significantly increases and reaches a value around 75° at the transition to the helical phase for $\mu_0 H = 30$ mT (see Fig. 5.10(e,h)). V_{SSE} fully disappears in a magnetic field of 0 T as shown in Fig. 5.10(f). For both devices S1 and S2, a similar value of phase φ is observed in the angular dependence of V_{SSE} in different magnetic fields. Fig. 5.10(g,h) shows the amplitude and phase of the angular dependence of the SSE, acquired from device S2 as a function of field H at $I = 1$ mA (in the linear regime, where V_{SSE} scales linearly with I^2) and at $I = 4$ mA (in the nonlinear regime). For both current values, a similar trend in the amplitude $R_{\mathrm{SSE}}^{\mathrm{ampl}}$ and phase φ is observed. The amplitude $R_{\mathrm{SSE}}^{\mathrm{ampl}}$ increases by increasing H and starts to saturate around $\mu_0 H = 4$ T (see Fig. 5.10(g)). $R_{\mathrm{SSE}}^{\mathrm{ampl}}$ is more than four times larger at 4 T field than the signal observed at the conical to ferrimagnetic transition ($\mu_0 H = 94$ mT). The phase φ decreases by increasing the magnetic field and $\varphi \approx 0$ for $\mu_0 H > 1$ T (see Fig. 5.10(h)). It would be of great interest to develop a theoretical model and interpretation of the observed SSE signal. However, this is outside the scope of this work, where we provide a detailed summary of our experimental findings of the SSE in the Pt|CSO.

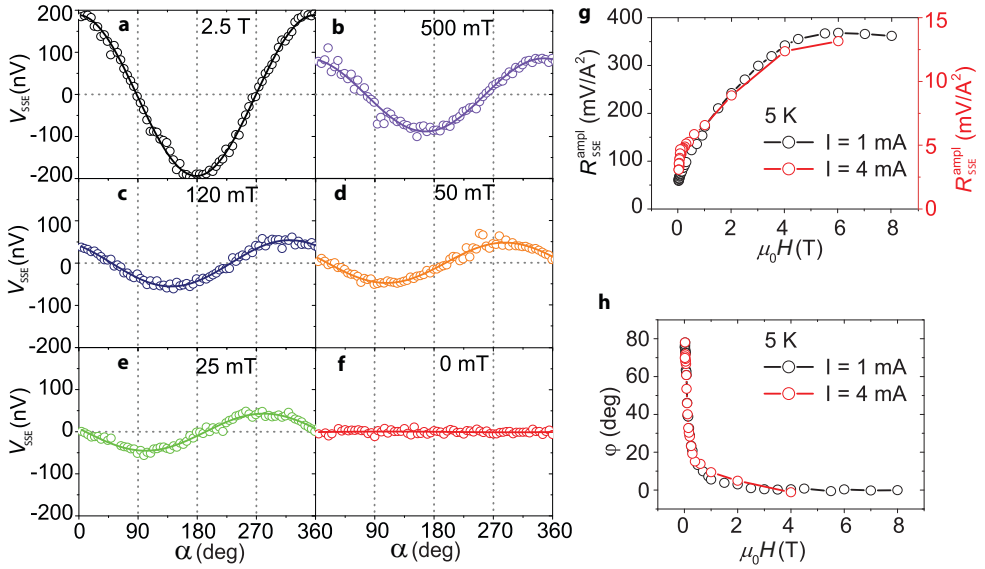

Figure 5.10: *(a-f) Angular dependence of the SSE response V_{SSE} in the Pt|CSO sample, due to current-induced heating, in different magnetic states of CSO. V_{SSE} in (a-c) the ferrimagnetic, (d) conical, and (e,f) in helical magnetic states of CSO. The data are centered around zero (g) Magnetic field dependence of the amplitude of second harmonic response R^{ampl}_{SSE}. (h) Magnetic field dependence of the phase φ appearing in the angular dependence of V_{SSE} for different applied currents. The presented data are acquired from device S2.*

5

Author contributions

A. Aqeel, B. J. van Wees and T. T. M. Palstra conceived the experiments. A. Aqeel and N. Vlietstra designed the experiments. The crystals were grown by A. Aqeel and T. T. M. Palstra. A. Aqeel fabricated devices and carried out the measurements. A. Aqeel and N. Vlietstra elaborated the obtained data. A. Aqeel, B. J. van Wees, M. Mostovoy, and T. T. M. Palstra carried out the analysis. Theoretical modelling was done by M. Mostovoy and A. Roy. A. Aqeel and M. Mostovoy wrote the paper, involving all co-authors.

Bibliography

[1] R. A. Duine, A. Brataas, S. A. Bender, and Y. Tserkovnyak, "Spintronics and Magnon Bose-Einstein Condensation," *ArXiv e-prints* , 2015.

[2] A. V. Chumak, V. I. Vasyuchka, A. A. Serga, and B. Hillebrands, "Magnon spintronics," *Nature Physics* **11**, pp. 453–461, 2015.

[3] G. E. W. Bauer, E. Saitoh, and B. J. van Wees, "Spin caloritronics," *Nature Materials* **11**, pp. 391–399, Apr. 2012.

[4] V. Lauer, D. A. Bozhko, T. Brcher, P. Pirro, V. I. Vasyuchka, A. A. Serga, M. B. Jungfleisch, M. Agrawal, Y. V. Kobljanskyj, G. A. Melkov, C. Dubs, B. Hillebrands, and A. V. Chumak, "Spin-transfer torque based damping control of parametrically excited spin waves in a magnetic insulator," *Applied Physics Letters* **108**(1), 2016.

[5] M. Schreier, T. Chiba, A. Niedermayr, J. Lotze, H. Huebl, S. Geprägs, S. Takahashi, G. E. W. Bauer, R. Gross, and S. T. B. Goennenwein, "Current-induced spin torque resonance of a magnetic insulator," *Physical Review B* **92**, p. 144411, Oct 2015.

[6] S. A. Manuilov, C. H. Du, R. Adur, H. L. Wang, V. P. Bhallamudi, F. Y. Yang, and P. C. Hammel, "Spin pumping from spinwaves in thin film YIG," *Applied Physics Letters* **107**(4), 2015.

[7] M. Haertinger, C. H. Back, J. Lotze, M. Weiler, S. Geprägs, H. Huebl, S. T. B. Goennenwein, and G. Woltersdorf, "Spin pumping in YIG/Pt bilayers as a function of layer thickness," *Physical Review B* **92**, p. 054437, Aug 2015.

[8] N. Vlietstra, J. Shan, B. J. van Wees, M. Isasa, F. Casanova, and J. Ben Youssef, "Simultaneous detection of the spin-Hall magnetoresistance and the spin-Seebeck effect in platinum and tantalum on yttrium iron garnet," *Physical Review B* **90**, p. 174436, Nov 2014.

[9] N. Vlietstra, J. Shan, V. Castel, B. J. van Wees, and J. Ben Youssef, "Spin-Hall magnetoresistance in platinum on yttrium iron garnet: Dependence on platinum thickness and in-plane/out-of-plane magnetization," *Physical Review B* **87**, p. 184421, May 2013.

[10] N. Vlietstra, J. Shan, V. Castel, J. Ben Youssef, G. E. W. Bauer, and B. J. van Wees, "Exchange magnetic field torques in YIG/Pt bilayers observed by the spin-Hall magnetoresistance," *Applied Physics Letters* **103**(3), 2013.

[11] K.-i. Uchida, H. Adachi, T. Ota, H. Nakayama, S. Maekawa, and E. Saitoh, "Observation of longitudinal spin-Seebeck effect in magnetic insulators," *Applied Physics Letters* **97**(17), 2010.

[12] K. Uchida, T. Ota, H. Adachi, J. Xiao, T. Nonaka, Y. Kajiwara, G. E. W. Bauer, S. Maekawa, and E. Saitoh, "Thermal spin pumping and magnon-phonon-mediated spin-Seebeck effect," *Journal of Applied Physics* **111**(10), 2012.

[13] A. Aqeel, I. J. Vera-Marun, B. J. van Wees, and T. T. M. Palstra, "Surface sensitivity of the spin Seebeck effect," *Journal of Applied Physics* **116**(15), p. 153705, 2014.

[14] M. Isasa, A. Bedoya-Pinto, and S. Vélez

[15] A. Aqeel, N. Vlietstra, J. A. Heuver, G. E. W. Bauer, B. Noheda, B. J. van Wees, and T. T. M. Palstra, "Spin-Hall magnetoresistance and spin Seebeck effect in spin-spiral and paramagnetic phases of multiferroic $CoCr_2O_4$ films," *Physical Review B* **92**, p. 224410, Dec 2015.

[16] K. Ganzhorn, J. Barker, R. Schlitz, B. A. Piot, K. Ollefs, F. Guillou, F. Wilhelm, A. Rogalev, M. Opel, M. Althammer, S. Geprägs, H. Huebl, R. Gross, G. E. W. Bauer, and S. T. B. Goennenwein, "Spin Hall magnetoresistance in a canted ferrimagnet," *Physical Review B* **94**, p. 094401, Sep 2016.

[17] S. M. Wu, W. Zhang, A. KC, P. Borisov, J. E. Pearson, J. S. Jiang, D. Lederman, A. Hoffmann, and A. Bhattacharya, "Antiferromagnetic Spin Seebeck Effect," *Physical Review Letters* **116**, p. 097204, Mar 2016.

[18] S. Seki, T. Ideue, M. Kubota, Y. Kozuka, R. Takagi, M. Nakamura, Y. Kaneko, M. Kawasaki, and Y. Tokura, "Thermal Generation of Spin Current in an Antiferromagnet," *Physical Review Letters* **115**, p. 266601, Dec 2015.

[19] J. S. White, I. Levatić, A. A. Omrani, N. Egetenmeyer, K. Prša, I. Živković, J. L. Gavilano, J. Kohlbrecher, M. Bartkowiak, H. Berger, and H. M. Rønnow, "Electric field control of the skyrmion lattice in Cu_2OSeO_3," *Journal of Physics: Condensed Matter* **24**(43), p. 432201, 2012.

[20] T. Adams, A. Chacon, M. Wagner, A. Bauer, G. Brandl, B. Pedersen, H. Berger, P. Lemmens, and C. Pfleiderer, "Long-Wavelength Helimagnetic Order and Skyrmion Lattice Phase in Cu_2OSeO_3," *Physical Review Letters* **108**, p. 237204, Jun 2012.

[21] T. Lancaster, R. C. Williams, I. O. Thomas, F. Xiao, F. L. Pratt, S. J. Blundell, J. C. Loudon, T. Hesjedal, S. J. Clark, P. D. Hatton, M. Ciomaga Hatnean, D. S. Keeble, and G. Balakrishnan, "Transverse field muon-spin rotation signature of the skyrmion-lattice phase in Cu_2OSeO_3," *Physical Review B* **91**, p. 224408, Jun 2015.

[22] S. Seki, X. Z. Yu, S. Ishiwata, and Y. Tokura, "Observation of Skyrmions in a Multiferroic Material," *Science* **336**(6078), pp. 198–201, 2012.

[23] J.-W. G. Bos, C. V. Colin, and T. T. M. Palstra, "Magnetoelectric coupling in the cubic ferrimagnet Cu_2OSeO_3," *Physical Review B* **78**, p. 094416, Sep 2008.

[24] N. Nagaosa and Y. Tokura, "Topological properties and dynamics of magnetic skyrmions," *Nature Nanotechnology* **8**, pp. 899–911, Dec. 2013.

[25] O. Janson, I. Rousochatzakis, A. A. Tsirlin, M. Belesi, A. A. Leonov, U. K. Rößler, J. van den Brink, and H. Rosner, "The quantum nature of skyrmions and half-skyrmions in Cu_2OSeO_3," *Nature Communications* **5**, p. 5376, Nov 2014.

[26] P. Bak and M. H. Jensen, "Theory of helical magnetic structures and phase transitions in MnSi and FeGe," *Journal of Physics C: Solid State Physics* **13**(31), p. L881, 1980.

[27] Y. K. Kato, R. C. Myers, A. C. Gossard, and D. D. Awschalom, "Observation of the Spin Hall Effect in Semiconductors," *Science* **306**(5703), pp. 1910–1913, 2004.

[28] J. Wunderlich, B. Kaestner, J. Sinova, and T. Jungwirth, "Experimental Observation of the Spin-Hall Effect in a Two-Dimensional Spin-Orbit Coupled Semiconductor System," *Physical Review Letters* **94**, p. 047204, Feb 2005.

[29] J. Sinova, S. O. Valenzuela, J. Wunderlich, C. H. Back, and T. Jungwirth, "Spin Hall effects," *Reviews of Modern Physics* **87**, pp. 1213–1260, Oct 2015.

[30] Y.-T. Chen, S. Takahashi, H. Nakayama, M. Althammer, S. T. B. Goennenwein, E. Saitoh, and G. E. W. Bauer, "Theory of spin Hall magnetoresistance," *Physical Review B* **87**, p. 144411, Apr 2013.

[31] X. Jia, K. Liu, K. Xia, and G. E. W. Bauer, "Spin transfer torque on magnetic insulators," *Europhysics Letters* **96**, p. 17005, Oct. 2011.

[32] M. Agrawal, V. I. Vasyuchka, A. A. Serga, A. Kirihara, P. Pirro, T. Langner, M. B. Jungfleisch, A. V. Chumak, E. T. Papaioannou, and B. Hillebrands, "Role of bulk-magnon transport in the temporal evolution of the longitudinal spin-Seebeck effect," *Physical Review B* **89**, p. 224414, Jun 2014.

[33] A. Kehlberger, U. Ritzmann, D. Hinzke, E.-J. Guo, J. Cramer, G. Jakob, M. C. Onbasli, D. H. Kim, C. A. Ross, M. B. Jungfleisch, B. Hillebrands, U. Nowak, and M. Kläui, "Length Scale of the Spin Seebeck Effect," *Physical Review Letters* **115**, p. 096602, Aug 2015.

[34] S. M. Rezende, R. L. Rodrìguez-Suàrez, R. O. Cunha, J. C. L. Ortiz, and A. Azevedo, "Bulk magnon spin current theory for the longitudinal spin Seebeck effect," *Journal of Magnetism and Magnetic Materials* **400**, pp. 171 – 177, 2016.

[35] M. Belesi, I. Rousochatzakis, H. C. Wu, H. Berger, I. V. Shvets, F. Mila, and J. P. Ansermet, "Ferrimagnetism of the magnetoelectric compound Cu_2OSeO_3 probed by ^{77}Se NMR," *Physical Review B* **82**, p. 094422, Sep 2010.

[36] M. Schreier, N. Roschewsky, E. Dobler, S. Meyer, H. Huebl, R. Gross, and S. T. B. Goennenwein, "Current heating induced spin Seebeck effect," *Applied Physics Letters* **103**(24), p. 242404, 2013.

[37] S. Geprägs, A. Kehlberger, F. D. Coletta, Z. Qiu, E.-J. Guo, T. Schulz, C. Mix, S. Meyer, A. Kamra, M. Althammer, H. Huebl, G. Jakob, Y. Ohnuma, H. Adachi, J. Barker, S. Maekawa, G. E. W. Bauer, E. Saitoh, R. Gross, S. T. Goennenwein, and M. Kläui, "Origin of the spin seebeck effect in compensated ferrimagnets," *Nature Communications* **7**, p. 10452, 2016.

[38] K.-i. Uchida, T. Kikkawa, A. Miura, J. Shiomi, and E. Saitoh, "Quantitative Temperature Dependence of Longitudinal Spin Seebeck Effect at High Temperatures," *Physical Review X* **4**, p. 041023, Nov 2014.

5

To be published as: A. Aqeel, I. J. Vera-Marun, Z. Salman, T. Prokscha, A. Suter, B. J. van Wees, and T. T. M. Palstra – *"Probing current-induced magnetic fields in Au|YIG heterostructure with low-energy muon spectroscopy,"* accepted in Appl. Phys. Lett. (2017).

Chapter 6

Probing current-induced magnetic fields in Au|YIG heterostructures with LEμSR

Abstract

We investigated the depth dependence of current-induced magnetic fields in a bilayer of a normal metal (Au) and a ferrimagnetic insulator (Yttrium Iron Garnet - YIG) by using low energy muon spin spectroscopy (LE-μSR). This allows us to explore how these fields vary from the Au surface down to the buried Au|YIG interface, which is relevant to study physics like the spin-Hall effect. We observed a maximum shift of 0.4 G in the internal field of muons at the surface of Au film which is in close agreement with the value expected for Oersted fields. As muons are implanted closer to the Au|YIG interface the shift is strongly suppressed, which we attribute to the dipolar fields present at the Au|YIG interface. Combining our measurements with modeling, we show that dipolar fields caused by the finite roughness of the Au|YIG interface consistently explains our observations. Our results, therefore, gauge the limits on the spatial resolution and the sensitivity of LE-μSR to the roughness of the buried magnetic interfaces, a prerequisite for future studies addressing current induced fields caused by the spin accumulations due to the spin-Hall effect.

6.1 Introduction

Recently the exciting field of spintronics has been transformed by new concepts to manipulate the spin transport taking place at the interfaces between magnetic and non-magnetic materials [1, 2]. Therefore, it is important to understand the spatial distribution of spin accumulation in different devices. The spin accumulations at these interfaces have been mostly created electrically by the spin-Hall effect (SHE) by sending a charge current through normal metal (NM) with strong spin-orbit coupling [3–5] on top of the magnetic insulators like YIG. These electrically created spin accumulations are usually detected by an indirect method called spin-Hall magnetoresistance effect in which the resistance of the NM changes with the magnetization of the underlying YIG [6]. In these electrical measurements used to probe SHE, the ever-present background contributions like Oersted fields (the magnetic fields generated by current flowing through a metal) and dipolar fields (the inhomogeneous

magnetic fields arising from the roughness of a magnetic surface) cannot be disentangled. Any technique that would aim to estimate these background contributions needs to be spin and magnetic field sensitive along with spatial resolution.

Muon spin spectroscopy is widely used as a magnetic spin microprobe to investigate superconductivity[7, 8], magnetism [9, 10] and many other fields [11]. In addition, low-energy muon spin rotation spectroscopy (LE-μSR) provides an opportunity to tune the energy of the muons (1 - 30 keV) to perform depth resolved internal field measurements in range of 1 - 200 nm [11–13]. Due to the combination of sensitivity [10] and the spatial resolution [11], LE-μSR has been applied successfully to obtain the depth-resolved profile of the local magnetization in various thin films and heterostructures [14, 15].

All these successful applications of LE-μSR motivate the study of its limits and capabilities in order to gauge the possibility of using such a technique for other sources of current-induced fields, e.g., due to the spin accumulation by SHE, Oersted fields or magnetization induced via proximity at buried interfaces. To explore this, we considered here a Au|YIG test structure. In this structure, due to the small spin-Hall angle of Au we expect negligible contribution from SHE, which allows us to quantify other current-induced contributions, such as ever-present Oersted fields and dipolar fields due to finite interface roughness. We report here the quantitative study of the depth distribution of magnetic fields in the Au|YIG system with LE-μSR [16, 17].

6.2 Device fabrication and measurement technique

Fig. 6.1(a) shows the device configuration used to quantify the current-induced magnetic field distribution at different depths in the Au|YIG heterostructure. The YIG has a thickness of 240 nm grown by liquid phase epitaxy on 0.5 mm-thick (111) Gadolinium Gallium Garnet (GGG) monocrystalline substrate. In any NM|YIG system, there would be two main contributions to a current-induced magnetic fields: one would be the spin accumulation due to SHE (see Fig. 6.1(b)) and other due to Oersted fields (see Fig. 6.1(c)). Note that for the Au metal (used here) we expect a spin diffusion length of 35 nm [18] which would make it compatible with depth-resolved studies of spin accumulation using LE-μSR. Nevertheless, for the specific case of SHE, the small spin-Hall angle makes the expected signals two orders of magnitude smaller than the Oersted fields, therefore in the current study we focus on quantifying the latter.

All measurements were performed at the LE-μSR spectrometers at the Paul Scherrer Institute, Villigen, Switzerland. The measurements were done at pressure $\leq 10^{-9}$ mbar in a cold finger cryostat. In these measurements, 100% spin polarized positive muons are implanted into the Au|YIG sample, with their spin polarization direction at an

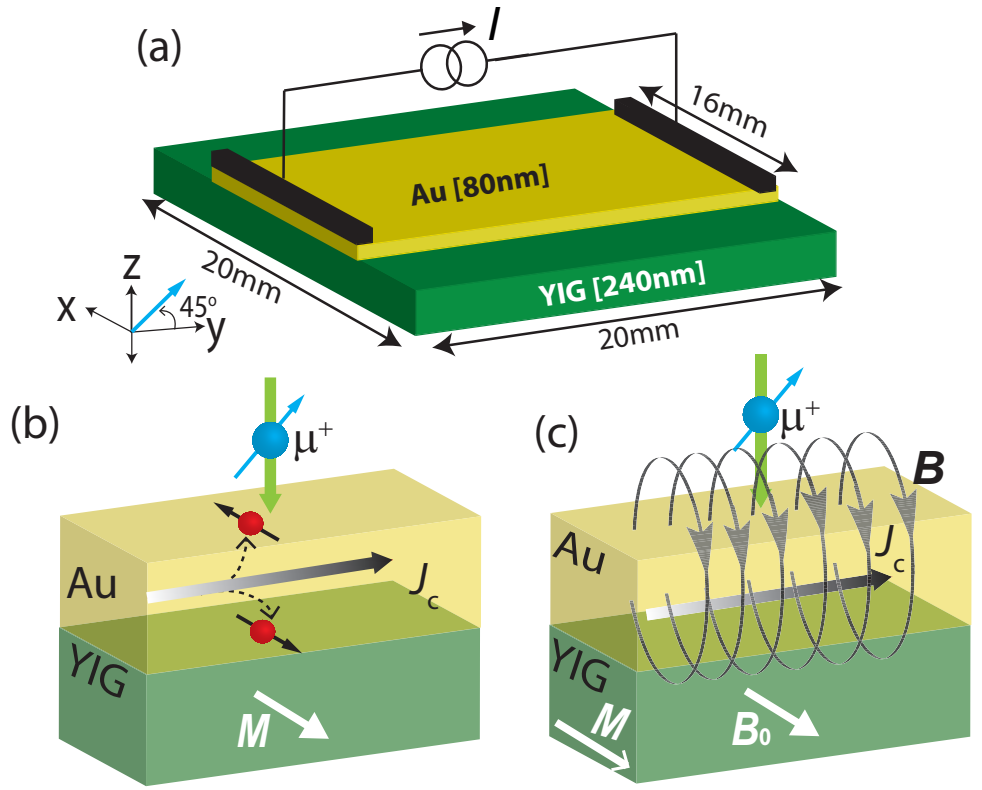

Figure 6.1: *(a) Device configuration for probing current-induced magnetic fields at Au|YIG interface with muons. (b) Schematic illustration of spatial directions of electrically created spin accumulation created by spin-Hall effect and (c) Oersted magnetic fields $\boldsymbol{B}$ with respect to muon beam μ^+. Here, J_c, $\boldsymbol{M}$ and $\boldsymbol{B}_0$ represent the applied dc-current, magnetization of the YIG film and the applied magnetic field.*

angle of 45° in the yz-plane (see Fig. 6.1). The implanted muons have a short lifetime of 2.2 μs after which they decay by emitting a positron, preferentially in the direction of the muon spin at the time of decay. The reference measurements at different temperatures show no significant temperature dependent spin depolarization of muons. The measurements reported here are done using the transverse field geometry, where the applied magnetic field ($B_0 = 100$ G) is perpendicular to the initial spin direction of the implanted muons (shown in Fig. 6.1). The decay positrons are detected using appropriately positioned detectors, to the left and right of the sample, relative to the incoming muons. The asymmetry, $A(t)$, the difference of the detected positrons in the left and right detectors normalized by their sum is proportional to

the time evolution of the muon spin polarization, which provides information regarding the local magnetic properties at the muon stopping site.

The measurements are performed at different implantation energies and applied currents. By varying the energy of the muons, they can be implanted at different depths in the Au metal. The obtained μSR spectra were analysed using the MUSRFIT software [19]. We find that the collected spectra at all implantation energies and applied currents fit best to Eq. 6.1.

$$A(t) = A_0 e^{-\lambda t} \cos(\omega t + \phi). \tag{6.1}$$

Here $\omega = \gamma B$, γ being the muon gyromagnetic ratio, which reflects that the muons experience a Lorentzian field distribution with an average field B and width λ and ϕ is the angle between the direction of the initial spin polarisation of the muon (at t=0) and the direction of positron emission. The Larmor frequency ω provides the information about the internal field at the muon site and the damping λ gives information about the inhomogeneity of the internal field at the muon site.

6.3 Results

The results of the fit parameters from Eq. 6.1 are shown in Fig. 6.2. For the damping λ we do not observe any trend versus current therefore in Fig. 6.2(a) we show λ only for zero current. Contrary to λ, there is a clear current dependence of the field shift ΔB. This dependence of ΔB is clearly larger at lower energies and gradually decreases until it fully disappears at higher energies ($E \approx 12$ keV), as shown in Fig. 6.2(b). When muons are implanted closer to the interface, ΔB almost disappears. The internal field at the muon site is also measured at zero current density to rule out other magnetic field induced effects like proximity effects consistent with current understanding of the NM|YIG films [20]. A clearer observation of the current dependence of ΔB for different energies is shown in Fig. 6.2(c): ΔB varies linearly with the applied current closer to the surface of the Au film at $E = 6.4$ keV and almost vanishes closer to the interface at $E = 17.5$ keV.

To interpret the data, we can model the expected field shifts due to current-induced fields as:

$$\Delta B_{\lambda'}(E) = \frac{1}{\int_{z=0}^{z=d} \frac{P(E,z)}{\lambda'(z)} dz} \int_{z=0}^{z=d} \frac{P(E,z)}{\lambda'(z)} B(z) dz. \tag{6.2}$$

where $B(z)$, $P(E,z)$ and $\lambda'(z)$ represent the current-induced Oersted fields, muon stopping profile and damping due to inhomogeneous fields close to Au|YIG interface. The Oersted fields for a uniform current density J through Au film can be calculated using $B = -\mu_0 J z' \hat{x}$ for $z' = z - t_{\mathrm{Au}}/2$, where t_{Au} and z are the thickness

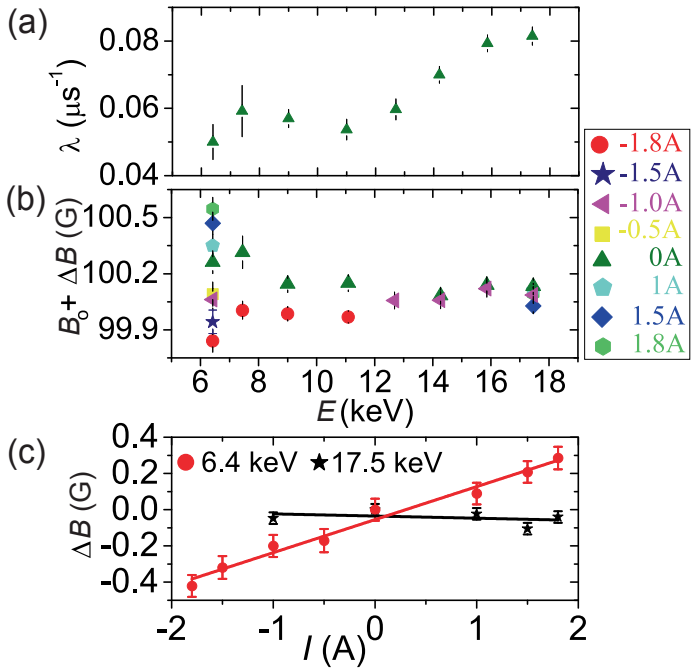

Figure 6.2: *(a) and (b) shows the observed damping λ and field $B_0 + \Delta B$ as a function of the implantation energy E of muons at different values of applied current (I = -1.8 A to 1.8 A) in the Au|YIG bilayer system, respectively. Here, B_0 represents the applied field. (c) Shift in the internal field ΔB at muon site as a function of the applied current I through the Au film at energies $E = 6.4$ keV, 17.5 keV*

of the Au film and the distance from the surface of Au towards the Au|YIG interface, respectively. We simulated the muon stopping profiles $P(E, z)$ by using the Trim.SP Monte Carlo program [19], as shown in Fig. 6.3(a). To get a clear relation between the muon implantation energy and the depth, we relate each energy to the peak position $z^{\max}$ of the muon distribution profile, as shown in the inset of Fig. 6.3(a).

The presence of any additional inhomogeneous field at the muon site can lead to the precession of muon spins at different frequencies and gives rise to the damping of the muon signal which we include in Eq. 6.2 by a parameter $\lambda'(z)$. This damping which we include as $\lambda'(z)$ can prevent us from observing expected field shift ΔB. The observed damping $\lambda(E)$ (shown in Fig. 6.2(a)) increases by a factor of two closer to the Au|YIG interface, also suggests the presence of these inhomogeneous fields $B_{\lambda'}$ closer to the interface. This inhomogeniety in the field $B_{\lambda'}$ is given by the expression $B_{\lambda'} = \lambda'(z)/2\pi\gamma$.

There are several mechanisms that can cause these inhomogeneous magnetic fields (therefore $\lambda'(z)$) close to the interface which can influence the expected magnetic field shifts including nuclear hyperfine fields [21–23], the dipolar fields from magnetic domains [24] or the interface roughness [25, 26]. The nuclear hyperfine fields are not relevant here as they are too small in Au, typically 0.02 μs^{-1}. We remark that the magnetic domains can be formed by anisotropy but for these films the

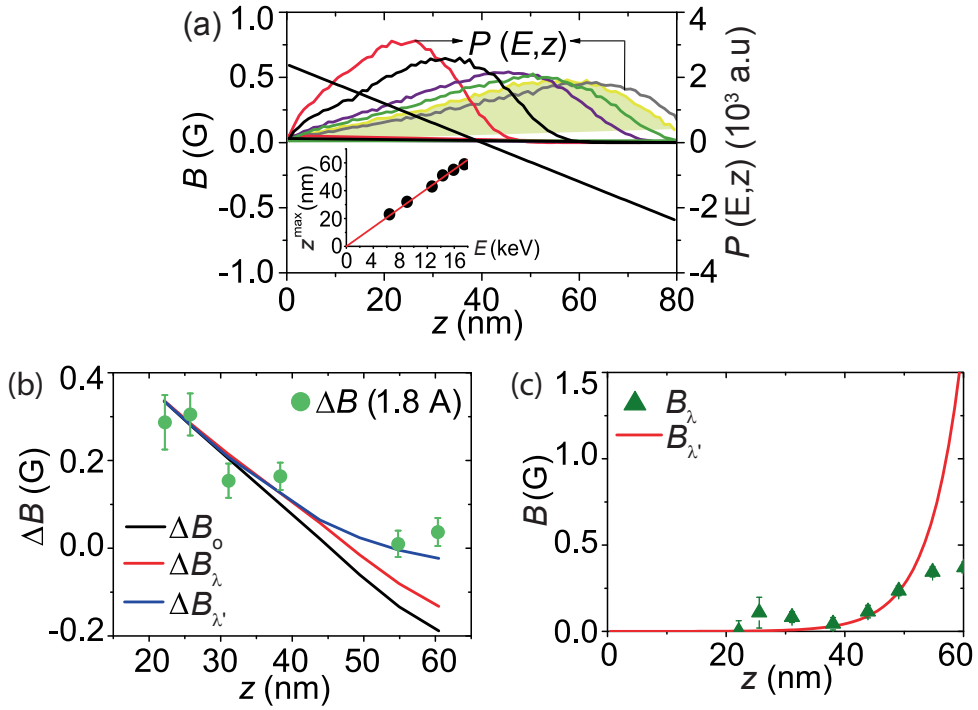

Figure 6.3: *(a) The current-induced magnetic field as a function of depth z, where z is the distance from the surface of Au towards the interface. $P(E, z)$ shows the probability distribution of the stopping depth of muons as a function of z at different implantation energies E varying from 6 keV to 18 keV. The inset of (a) shows the depth $z^{\max}$ of the peak maxima for each probability distribution $P(E, z)$ shown in (a) versus E. It provides a scale ($z^{\max} = 3.455 \times E$) to translate from E to depth z for (b) and (c), where $z = z^{\max}$. (b) Comparison of observed field shifts ΔB with the calculated shifts ΔB_o, ΔB_λ and $\Delta B_{\lambda'}$ at different implantation energies of muons. Here, ΔB_o, ΔB_λ and $\Delta B_{\lambda'}$ represent the field shifts including only the muon depth distribution profiles, the effect of observed damping λ shown in Fig. 2(a) and the effect of estimated damping λ' due to the dipolar fields, respectively. (c) Comparison between the field B_λ calculated by considering the observed λ and the dipolar field $B_{\lambda'}$ (using Eq. 6.3) as a function of distance z.*

anisotropy is not relevant and the thickness of YIG film is still small enough to neglect also the interfacial anisotropy, recently reported in thicker YIG films [27]. Moreover, the coercivity of the YIG film is around 2 G, therefore in these experiments the film is fully saturated and we can ignore the effect of magnetic domain boundaries. However, the inhomogeneous magnetic fields arising from finite interface roughness can dramatically influence the dynamics of expected magnetic fields at the magnetic

interface of multilayer systems [26]. The magnitude of these inhomogeneous dipolar fields scales with the roughness amplitude h and decays with distance z from the interface on a length scale of the lateral roughness η [26, 28]. Fig. 6.4(c) shows the sketch of the dipolar fields near the Au|YIG interface with a finite roughness. The dipolar fields [26] can be estimated as follows:

$$B_{\lambda'}(z) = \mu_0 M_s \frac{h}{2} \sum_{n=1}^{\infty} q_n \frac{\sin(\frac{1}{4}q_n\eta)}{\frac{1}{4}\eta q_n} \frac{\sin(\frac{1}{2}q_n h)}{\frac{1}{2}q_n h} \exp(-q_n z). \tag{6.3}$$

Here $q_n = \frac{2\pi n}{\eta}$ and M_s is the saturation magnetization of YIG. For this model of the sinusoidal interface profile, lateral period $\eta = 20$ nm and roughness amplitude $h = 1$ nm are estimated from the atomic force microscope image of the YIG surface shown in Fig. 6.4(a,b). Fig. 6.3(c) shows the dipolar fields $B_{\lambda'}$ estimated by Eq.6.3.

To find the effect of these dipolar fields on the observed field shifts ΔB, we calculated damping λ' associated with the dipolar fields $B_{\lambda'}$ and used it in Eq. 6.2. Fig. 6.3(b) shows a good agreement between the field shifts $\Delta B_{\lambda'}$ estimated by including dipolar fields and the measured field shifts ΔB, both vanishing closer to the Au|YIG interface. Therefore, we achieved a consistent picture by taking into account the damping λ' due to the dipolar fields resulting from the finite surface roughness.

To check whether the assumption of presence of the inhomogeneous fields $\Delta B_{\lambda'}$ close to the interface is correct, we can estimate these fields by using the observed damping $\lambda(E)$ (Fig. 6.2(a)). The estimated B_λ is around 0.3 G, which is in the same order as expected current-induced fields at the interface (cf. Fig. 6.2(c) to 6.2(c)). However, these B_λ fields are much smaller than the inhomogeneous fields $B_{\lambda'}$ estimated for the dipolar fields at the interface, which can be understood from the fact that B_λ are also convoluted from the muon profile $P(E, z)$, in reality the dipolar fields can be much larger than these estimated values. Fig. 6.3(b) shows that the estimated inhomogeneous fields ΔB_λ by using $\lambda(E)$ result in preferential reduction of the shift around 30% close to the interface. To further confirm if the assumption of the inhomogeneous fields $B_{\lambda'}$ at the interface is correct, we can calculate the field shifts without the damping λ' by considering it to be depth independent (i.e. $\lambda'(z) = 1$). Fig. 6.3(b) shows that the field shifts (ΔB_o) without considering the effect of damping is around 0.2 G at the interface, much larger than the value around 0 G observed close to the interface. Therefore, it confirms that the assumption of dipolar fields at the interface is in good agreement with experimental observations, as shown in Fig. 6.3(b).

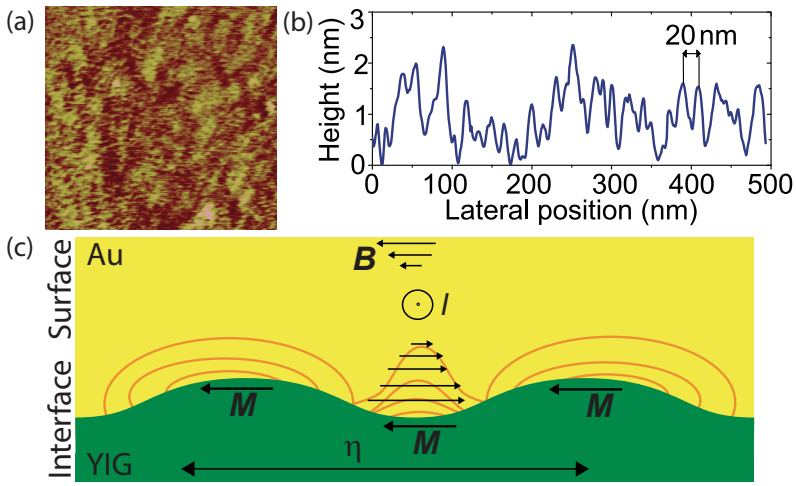

Figure 6.4: *(a) Atomic force microscope image (500×500 nm^2) and (b) a representative cross-sectional height profile of the YIG surface, prior to the Au metal deposition. (c) Illustration of inhomogeneous dipolar fields near the Au|YIG interface with finite roughness, sketched for a sinusoidal interface profile with a lateral period η. Here **M** and **B** represent the magnetization of YIG and the current-induced field, respectively.*

6.4 Conclusions

In conclusion we have established that LE-μSR can indeed work for resolving the background signals present due to interface roughness and Oersted fields which are a universal feature in experiments done to probe SHE, with proper magnitude, distance dependence and sign. In the current measurements, we obtained a field resolution below 0.1 G. We have to gauge the viability of the SHE by making sure that the induced spin-accumulations creates the magnetic field of this order which now would depend on the specific parameters of the material. Moreover, the depth variation in the local magnetic field from SHE is on the scale of 10 nm which is compatible to the resolution of LE-μSR, confirming the suitability of the technique to these measurements. Hence, our results establish a point of reference and a guide for future experiments aiming to probe SHE with muons.

Author contributions

A. Aqeel, I. J. Vera-Marun and T. T. M. Palstra conceived the experiments. A. Aqeel and I. J. Vera-Marun designed the experiments. Z. Salman, T. Prokscha and A. Suter designed the LE-muon spectrometer. A. Aqeel fabricated the devices. A. Aqeel, Z. Salman and T. T. M. Palstra carried out the measurements. A. Aqeel and I. J. Vera-

Marun elaborated the obtained data. A. Aqeel, I. J. Vera-Marun, Z. Salman, B. J. van Wees and T. T. M. Palstra carried out the analysis. A. Aqeel wrote the paper, involving all co-authors.

Bibliography

[1] N. Vlietstra, J. Shan, B. J. van Wees, M. Isasa, F. Casanova, and J. Ben Youssef, "Simultaneous detection of the spin-Hall magnetoresistance and the spin-Seebeck effect in platinum and tantalum on yttrium iron garnet," *Phys. Rev. B* **90**, p. 174436, Nov 2014.

[2] G. E. W. Bauer, E. Saitoh, and B. J. van Wees, "Spin caloritronics," *Nature Mater.* **11**, pp. 391–399, Apr. 2012.

[3] Y. K. Kato, R. C. Myers, A. C. Gossard, and D. D. Awschalom, "Observation of the Spin Hall Effect in Semiconductors," *Science* **306**(5703), pp. 1910–1913, 2004.

[4] J. Wunderlich, B. Kaestner, J. Sinova, and T. Jungwirth, "Experimental Observation of the Spin-Hall Effect in a Two-Dimensional Spin-Orbit Coupled Semiconductor System," *Phys. Rev. Lett.* **94**, p. 047204, Feb 2005.

[5] J. Sinova, S. O. Valenzuela, J. Wunderlich, C. H. Back, and T. Jungwirth, "Spin Hall effects," *Rev. Mod. Phys.* **87**, pp. 1213–1260, Oct 2015.

[6] N. Vlietstra, J. Shan, V. Castel, B. J. van Wees, and J. Ben Youssef, "Spin-Hall magnetoresistance in platinum on yttrium iron garnet: Dependence on platinum thickness and in-plane/out-of-plane magnetization," *Phys. Rev. B* **87**, p. 184421, May 2013.

[7] J. E. Sonier, J. H. Brewer, and R. F. Kiefl, "μSR studies of the vortex state in type-II superconductors," *Rev. Mod. Phys.* **72**, pp. 769–811, Jul 2000.

[8] R. F. Kiefl, M. D. Hossain, B. M. Wojek, S. R. Dunsiger, G. D. Morris, T. Prokscha, Z. Salman, J. Baglo, D. A. Bonn, R. Liang, W. N. Hardy, A. Suter, and E. Morenzoni, "Direct measurement of the London penetration depth in $YBa_2Cu_3O_{6.92}$ using low-energy μSR," *Phys. Rev. B* **81**, p. 180502, May 2010.

[9] P. Dalmas de Réotier, A. Maisuradze, A. Yaouanc, B. Roessli, A. Amato, D. Andreica, and G. Lapertot, "Determination of the zero-field magnetic structure of the helimagnet MnSi at low temperature," *Phys. Rev. B* **93**, p. 144419, Apr 2016.

[10] Z. Guguchia, H. Keller, R. K. Kremer, J. Köhler, H. Luetkens, T. Goko, A. Amato, and A. Bussmann-Holder, "Spin-lattice coupling induced weak dynamical magnetism in $EuTiO_3$ at high temperatures," *Phys. Rev. B* **90**, p. 064413, Aug 2014.

[11] Z. Salman, T. Prokscha, A. Amato, E. Morenzoni, R. Scheuermann, K. Sedlak, and A. Suter, "Direct Spectroscopic Observation of a Shallow Hydrogenlike Donor State in Insulating $SrTiO_3$," *Phys. Rev. Lett.* **113**, p. 156801, Oct 2014.

[12] E. Morenzoni, R. Khasanov, H. Luetkens, T. Prokscha, A. Suter, N. Garifianov, H. Glckler, M. Birke, E. Forgan, H. Keller, J. Litterst, C. Niedermayer, and G. Nieuwenhuys, "Low energy muons as probes of thin films and near surface regions," *Physica B* **326**(14), pp. 196 – 204, 2003.

[13] T. Prokscha, E. Morenzoni, K. Deiters, F. Foroughi, D. George, R. Kobler, A. Suter, and V. Vrankovic, "The new μE4 beam at PSI: A hybrid-type large acceptance channel for the generation of a high intensity surface-muon beam," *Nucl. Instrum. Methods Phys. Res., Sect. A* **595**(2), pp. 317 – 331, 2008.

[14] A. Suter, E. Morenzoni, R. Khasanov, H. Luetkens, T. Prokscha, and N. Garifianov, "Direct Observation of Nonlocal Effects in a Superconductor," *Phys. Rev. Lett.* **92**, p. 087001, Feb 2004.

[15] A. J. Drew, S. L. Lee, D. Charalambous, A. Potenza, C. Marrows, H. Luetkens, A. Suter, T. Prokscha, R. Khasanov, E. Morenzoni, D. Ucko, and E. M. Forgan, "Coexistence and Coupling of Superconductivity and Magnetism in Thin Film Structures," *Phys. Rev. Lett.* **95**, p. 197201, Nov 2005.

[16] T. Prokscha, E. Morenzoni, K. Deiters, F. Foroughi, D. George, R. Kobler, A. Suter, and V. Vrankovic, "The new high-intensity surface muon beam μE4 for the generation of low-energy muons at PSI," *Physica B* **374375**(0), pp. 460 – 463, 2006.

[17] P. Bakule and E. Morenzoni, "Generation and applications of slow polarized muons," *Contemp. Phys.* **45**(3), pp. 203–225, 2004.

[18] O. Mosendz, V. Vlaminck, J. E. Pearson, F. Y. Fradin, G. E. W. Bauer, S. D. Bader, and A. Hoffmann, "Detection and quantification of inverse spin Hall effect from spin pumping in permalloy/normal metal bilayers," *Phys. Rev. B* **82**, p. 214403, Dec 2010.

[19] E. Morenzoni, H. Glckler, T. Prokscha, R. Khasanov, H. Luetkens, M. Birke, E. Forgan, C. Niedermayer, and M. Pleines, "Implantation studies of keV positive muons in thin metallic layers," *Nucl. Instrum. Methods Phys. Res., Sect. B* **192**(3), pp. 254 – 266, 2002.

[20] H. Nakayama, M. Althammer, Y.-T. Chen, K. Uchida, Y. Kajiwara, D. Kikuchi, T. Ohtani, S. Geprägs, M. Opel, S. Takahashi, R. Gross, G. E. W. Bauer, S. T. B. Goennenwein, and E. Saitoh, "Spin Hall Magnetoresistance Induced by a Nonequilibrium Proximity Effect," *Phys. Rev. Lett.* **110**, p. 206601, May 2013.

[21] I. A. Merkulov, A. L. Efros, and M. Rosen, "Electron spin relaxation by nuclei in semiconductor quantum dots," *Phys. Rev. B* **65**, p. 205309, Apr 2002.

[22] R. I. Dzhioev, V. L. Korenev, I. A. Merkulov, B. P. Zakharchenya, D. Gammon, A. L. Efros, and D. S. Katzer, "Manipulation of the Spin Memory of Electrons in n-GaAs," *Phys. Rev. Lett.* **88**, p. 256801, Jun 2002.

[23] J. Strand, B. D. Schultz, A. F. Isakovic, C. J. Palmstrøm, and P. A. Crowell, "Dynamic Nuclear Polarization by Electrical Spin Injection in Ferromagnet-Semiconductor Heterostructures," *Phys. Rev. Lett.* **91**, p. 036602, Jul 2003.

[24] V. L. Korenev, "Optical orientation in ferromagnet/semiconductor hybrids," *Semicond. Sci. Technol.* **23**(11), p. 114012, 2008.

[25] A. Aqeel, I. J. Vera-Marun, B. J. van Wees, and T. T. M. Palstra, "Surface sensitivity of the spin Seebeck effect," *J. Appl. Phys.* **116**(15), pp. –, 2014.

[26] S. P. Dash, S. Sharma, J. C. Le Breton, J. Peiro, H. Jaffrès, J.-M. George, A. Lemaître, and R. Jansen, "Spin precession and inverted Hanle effect in a semiconductor near a finite-roughness ferromagnetic interface," *Phys. Rev. B* **84**, p. 054410, Aug 2011.

[27] K.-i. Uchida, J.-i. Ohe, T. Kikkawa, S. Daimon, D. Hou, Z. Qiu, and E. Saitoh, "Intrinsic surface magnetic anisotropy in $Y_3Fe_5O_{12}$ as the origin of low-magnetic-field behavior of the spin Seebeck effect," *Phys. Rev. B* **92**, p. 014415, Jul 2015.

[28] S. Demokritov, E. Tsymbal, P. Grünberg, W. Zinn, and I. K. Schuller, "Magnetic-dipole mechanism for biquadratic interlayer coupling," *Phys. Rev. B* **49**, pp. 720–723, Jan 1994.

To be published as: A. Aqeel, J. Baas, G. R. Blake, & T. T. M. Palstra – *"Growth and helicity of non-centrosymmetric Cu_2OSeO_3 crystals,"* in Crystal Growth & Design.

Chapter 7

Growth of non-centrosymmetric Cu_2OSeO_3 single crystals

Abstract

We have grown Cu_2OSeO_3 single crystals with a new vapor transport technique using $SeCl_4$ as a transport agent. We are able to grow Cu_2OSeO_3 crystals of maximum size 8 mm × 7 mm × 4 mm with a transport duration of around three weeks. We found this new technique more efficient and simple compared to the commonly used growth technique reported in literature. The Cu_2OSeO_3 crystals have a very high quality and the absolute structures can be fully determined by simple single crystal x-ray diffraction. We observe crystals with both left-handed and right-handed chiralities.

7.1 Introduction

Noncentrosymmetric magnetic materials have attracted considerable attention recently in the field of magnetoelectric materials (ME). In these materials the absence of an inversion center can lead to novel behavior such as multiferroics or novel magnetic textures like skyrmions. The most well studied chiral systems are MnSi [1, 2], $Mn_{1-x}Fe_xGe$ [3], FeGe [4] and a semiconducting $Fe_{1-x}Co_xSi$ [5]. In these chiral magnets, the principal magnetic phases are a helical phase, a single domain conical phase and a skyrmion state (known as the A-phase) which appears in a small magnetic field-temperature (B-T) pocket close to transition temperature T_N. In the chiral atomic framework of this crystal family, the orbital motion of localized electrons also takes helical paths. The neighboring spins of localized electrons are coupled by the relativistic spin-orbit interaction called the Dzyaloshinskii-Moriya (DM) interaction [6, 7]. As the sign of the DM interaction is determined by the chemical composition, it emphasizes that the magnetic chirality is intrinsically dependent on the lattice handedness. It has been shown experimentally in $Mn_{1-x}Fe_xGe$ crystals that the skyrmion helicity is directly correlated with the crystal helicity [3].

Cu_2OSeO_3 is one of the most important members of the chiral group with the $P2_13$ chiral cubic crystal structure. It is the first insulator in which the skyrmion lattice has been observed [8, 9] with a very similar B-T phase diagram to those of

other related members of this chiral group. The insulating behavior of Cu_2OSeO_3 makes the study of the decisive role of crystal helicity especially more interesting by excluding other contributions caused by conduction electrons. To understand the unique magnetic structure of Cu_2OSeO_3, several different techniques have been employed including muon spin rotation spectroscopy [10], Lorentz transmission electron microscopy [9], AC susceptibility measurements [11], Terahertz Electron Spin Resonance [12] and time-resolved magneto-optics [13]. Recently, generation of spin currents has been studied in Cu_2OSeO_3 by a spin-pumping experiment [14].

Considering the large interest in the magnetic properties of Cu_2OSeO_3, it is important to look for new, efficient and fast growth techniques. Conventionally, Cu_2OSeO_3 is grown by the vapor transport method with HCl gas as transport agent. With this growth method only one helicity has been reported [15], but the other helicity has not been reported yet to the best of our knowledge. It is known that the structural and magnetic chiralities for Cu_2OSeO_3 crystals are directly correlated [15]. Therefore, to obtain both magnetic chiralities, it is needed to improve the growth techniques not only to increase the growth rate but also to get crystals with both chiralities. Here, we report a new and efficient way for the growth of Cu_2OSeO_3 single crystals with $SeCl_4$ as transport agent. We observe very high quality crystal growth having both chiralities with this new transport agent. The crystal structure of Cu_2OSeO_3 crystals has been studied before [16–18] with different diffraction techniques. Here, we use single crystal x-ray diffraction (XRD) to establish the absolute structures for both handednesses. This confirms the good quality of the crystals.

7.2 Synthesis and experimental methods

Single crystals of Cu_2OSeO_3 were grown by the standard chemical vapor transport method. The novelty of our growth method is the use of selenium tetrachloride ($SeCl_4$) as a transport agent. Previously, $SeCl_4$ was mainly used to grow molybdenum and tungsten diselenides. In the literature Cu_2OSeO_3 is usually grown with HCl gas [19]. Here, we report the growth of chiral magnets with $SeCl_4$ as transport agent which is new and different from those used in the literature [20]. For growth, transparent quartz ampoules (30 mm inside diameter, 30 cm length) were used. They were first carefully cleaned with ethanol, acetone, 10% HF, and demi water and dried overnight at 200 °C before the charge was introduced. $SeCl_4$ is very hygroscopic; therefore, it was weighed and introduced into the transport tubes in a glove box under a nitrogen atmosphere. Mixtures of high-purity CuO (Alfa-Aldrich, 99.995 %) and SeO_2 (Alfa-Aldrich, 99.999%) powders in a molar ratio of 2:1 were sealed in an evacuated quartz ampoule with 0.54 g of $SeCl_4$ (Alfa-Aldrich, 99.5%). After a few minutes of degassing, the part of the ampoule containing the chemi-

cals was immersed into liquid nitrogen, subsequently evacuated and sealed after the chemicals had cooled below their evaporation temperatures. The ampoule was then placed horizontally into a tubular three-zone furnace having 18 cm - long zones separated by a distance of 3 cm. The temperature of the furnace was raised gradually by 50 °C/h to 600 °C. To get rid of unwanted nucleation centers, a reverse temperature gradient was applied by adjusting the temperature of the source zone (T_{hot}) to 610 °C and the deposition zone (T_{cold}) to 660 °C for 24h. Afterwards, T_{hot} and T_{cold} were adjusted to 610 °C and 570 °C, respectively, for growth. These furnaces were regulated by a PID electronic regulator (SHINKO) with $\pm$0.5 °C temperature stability at 500-650 °C. After two weeks, shiny crystals could be seen at the deposition zone. After four weeks, the ampoules were quenched at the source zone so that all gas vapors quickly condensed at the source zone. The extreme hygroscopic nature of $SeCl_4$

Table 7.1: *Growth conditions for Cu_2OSeO_3 with CVT growth method for different transport agents (TA).*

TA	T_{hot} (°C)	T_{cold} (°C)	growth duration (d)	max. size of crystals (mm^3)
HCl [19]	620	580	49	130-150
$SeCl_4$	610	570	23	210-224

resulted in the presence of water in the ampoules, in spite of all precautions taken. The presence of water can create the vapor phase of hydrogen chloride (HCl) and a chalcogen oxichloride (SeOCl), thus making the analysis of the transport mechanism more complex. However, we observed that the presence of moisture slows down the transport process. This transport method with $SeCl_4$ resulted in reasonably big and thick crystals. To compare the efficiency of the growth method, we also synthesized the crystals with HCl gas as transport agent as reported in the literature [19]. The growth conditions are summarized in Table 7.1. The crystal structure of Cu_2OSeO_3 crystals is investigated with a D8 Venture single crystal x-ray diffractometer (XRD). The crystal quality is checked with precision scans of XRD for full sphere approximation.

7.3 Results

Table 7.2 shows the parameters used to establish the absolute structure of Cu_2OSeO_3 single crystals. Cu_2OSeO_3 crystals display the $P2_13$ space group and the ions occupy the Wyckoff positions that are summarized in Table 7.3. The precision scans of XRD for full sphere approximation show the high quality of Cu_2OSeO_3 single crystals without any twinning.

Table 7.2: *Crystallographic data and structure refinement for Cu_2OSeO_3 single crystals.*

Temperature	100 K
crystal system	cubic
space group	$P2_13$
wavelength	0.7107 A°
unit cell dimension a	8.9446 A°
θ range for data collection	3.147° - 32.25°
Limiting indices	-13 $\leq$ h $\leq$ 13
	-11 $\leq$ k $\leq$ 11
	-13 $\leq$ l $\leq$ 13
Reflections collected / unique	0.0367
Final R indices [I $> 2\sigma$(I)]	0.0312
Absolute structure parameter	-0.01(2)

The chirality of the crystals was characterized with the Flack parameter analysis. The Flack parameter is defined as the ratio between two opposite-handed domains for non-centrosymmetric crystals giving rise to a resonant contribution in the x-ray scattering amplitudes. A Flack parameter equal to zero corresponds to a single domain of the chiral structure (enantiopure) and a Flack parameter equal to 1 represents a single domain structure but with opposite chirality. The absolute structures are solved by calculating the atomic coordinates during refinement of the Flack parameter x by using the twin model for intensities of hkl reflections as follows:

$$\mathrm{I}_{\mathrm{hkl}}^{\mathrm{calc}} = (1\text{-x}) \mid \mathrm{F}_{\mathrm{hkl}} \mid^2 + \mathrm{x} \mid \mathrm{F}_{\text{-h-k-l}} \mid^2 \tag{7.1}$$

Here, $\mid \mathrm{F}_{\mathrm{hkl}} \mid$ and $\mid \mathrm{F}_{\text{-h-k-l}} \mid$ represent the structure factors. The dual-space SHELXL method was used for the structure determination. The full sphere of Bragg reflections was used for refinement. Results of least square refinement give a Flack x of 0.013(17) indicating two absolute structures having opposite chirality. The deviation factor is defined as:

$$R_1 = \Sigma \mid \mathrm{F}_{\mathrm{obs}} - \mathrm{F}_{\mathrm{calc}} \mid / \Sigma \mathrm{F}_{\mathrm{obs}} \tag{7.2}$$

The standard deviation R_1 was found to be 0.0217, which shows that the scattering strictly follows the Flack conditions. We measured eleven crystals to resolve the absolute structure, in which we found seven right-handed and four left-handed enantiomers. The atomic coordinates for absolute structures for left-handed and right-handed enantiomers of Cu_2OSeO_3 are summarized in Table 7.3.

Table 7.3: *Atomic coordinates and Wyckoff positions (WF) for Cu_2OSeO_3 for both handedness.*

		Right-handed			Left-handed		
	WP	x	y	z	x	y	z
Cu (1)	4a	0.88589(3)	0.88589(3)	0.88589(3)	0.11404(4)	0.11404(4)	0.11404(4)
Cu (2)	12b	0.13439(3)	0.12108(3)	0.87247(3)	0.86549(4)	0.87895(4)	0.12754(4)
Se (1)	4a	0.45963(3)	0.45963(3)	0.45963(3)	0.54031(4)	0.54031(4)	0.54031(4)
Se (2)	4a	0.21201(3)	0.21201(3)	0.21201(3)	0.78802(4)	0.78802(4)	0.78802(4)
O (1)	4a	0.01031(3)	0.01031(3)	0.01031(3)	0.98974(3)	0.98974(4)	0.98974(3)
O (2)	12b	0.76232(2)	0.76232(2)	0.76232(2)	0.23730(3)	0.23730(4)	0.23730(3)
O (3)	4a	0.27029(2)	0.48318(2)	0.46954(2)	0.72971(3)	0.51663(4)	0.53014(3)
O (4)	12b	0.27257(2)	0.18681(2)	0.03276(2)	0.72786(3)	0.81329(4)	0.96738(3)

7.4 Discussion

7.4.1 Chemical vapor transport

The vapor transport technique [19] commonly used for the growth of Cu_2OSeO_3 single crystals is relatively slow and complex due to the use of HCl gas as transport agent. However, the method reported in this paper is very simple and easy due to the use of a solid transport agent $SeCl_4$, and it was also found to be relatively fast. A disadvantage of $SeCl_4$ as a transport agent could be the strong silica attack and its strong hygroscopic nature which can be easily settled by using the transport agent in an inert and dry atmosphere. $SeCl_4$ has been frequently used in the past as an efficient transport agent for the growth of diselenides such as WSe_2 and $MoSe_2$ [20–22]. Like $SeCl_4$, $TeCl_4$ can also be an efficient transport agent. $TeCl_4$ is more stable and less hygroscopic than $SeCl_4$ which makes it a more suitable transport agent than $SeCl_4$ for vapor transport growth. However, $TeCl_4$ can dope the crystals and, therefore, $SeCl_4$ is more suitable for growth of undoped Cu_2OSeO_3 crystals. The decomposition of $SeCl_4$ will give a mixture of selenium and dichlorine that can result in possible gaseous oxygen compounds during transport for $SeCl_4$ can be SeO_2, $SeOCl_2$ and SeO. Chlorine resulting from the decomposition of $SeCl_4$ is probably playing the efficient role in the transport but the role of the selenium is not very clear in the transport. In case of presence of water, the transport would be more complicated by also involving HCl vapors for the transport. We observed a clear decrease in the deposition rate by exposing the $SeCl_4$ transport agent to air.

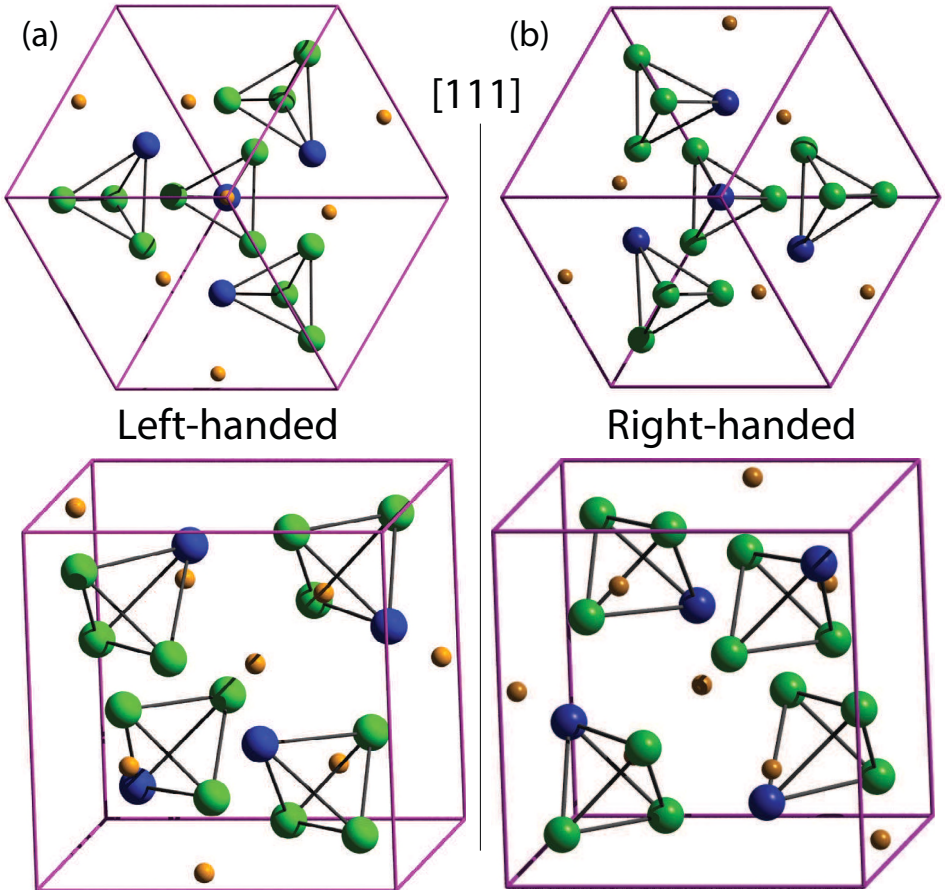

Figure 7.1: *The two chiral crystal structures of Cu_2OSeO_3 where blue (green) spheres represent Cu1 (Cu2) atoms and orange spheres represent non-magnetic Se atoms. The non-magnetic Se atoms are represented by orange spheres. The top views are along the body diagonal of the cube (along [111] axis). (a) left-handed and (b) right-handed crystals.*

7.4.2 Absolute structure determination

The absolute structures were solved for eleven crystals, grown with $SeCl_4$ as transport agent. During refinement the Goodness of Fit (GooF) was found to be 0.9-1.03, the scale factor K was 0.95-1.0 and the standard deviation R1 was found to be 0.2-0.5, which confirmed the high quality of those crystals. Seven out of eleven analyzed crystals showed the same helicity and the other four crystals showed the opposite.

The helicity can be defined from the Wyckoff position of magnetic ions. In the case of Cu_2OSeO_3, Cu(1) and Cu(2) ions are located at 4a and 12b Wyckoff position as shown in Table 7.3. The 4a Wyckoff positions of Cu(1) in Cu_2OSeO_3 are (x,x,x), (0.5+x,0.5x,x), (x,0.5+x,0.5x) and (0.5x,x,0.5+x) where x ≈ 0.136 or x ≈ 1 - 0.136 = 0.863 corresponding to two enantiomers. The crystals having Cu(1) at x = 0.863 are defined as the right-handed enantiomer and others with x = 0.136 as the left-handed enantiomer as shown in Table 7.3. The structure of Cu_2OSeO_3 with the same set of coordinates for the right-handed crystals shown in Table 7.3 is also defined as right-handed in Ref. [15]. There, the crystals are defined as right-handed on the basis of similarity of the 4a Wyckoff position of Cu(1) ion in Cu_2OSeO_3 and Mn in MnSi (right-handed).

The crystal helicity can also be defined by considering the closeness of the structural symmetry of the $P2_13$ space group with the absolute structure of $P4_132$ as proposed by Ref. [23]. The $P4_132$ space group contains only right-handed screw axes 4_1. Therefore, the right-handed crystals of the $P2_13$ space group can be easily distinguished by comparison. The same approach is also mentioned for B20 structures [24]. The set of coordinates determined with this definition for right-handed crystals is found to be consistent with the obtained absolute structure for the right-handed crystals as shown in Table 7.3.

7.4.3 Broadband helimagnon resonance measurements

Experimental investigation of magnetic resonances[1] confirmed the high quality of the Cu_2OSeO_3 single crystals grown by the method described above. The measurements were performed at 5 K using a broadband spectroscopy technique based on vector network analysis (VNA).

The magnon resonances were excited and detected in different magnetic phases of Cu_2OSeO_3 by measuring the complex transmission S_{21} with a VNA between two ports, as a function of frequency f. To remove the background contributions, the normalized transmission is defined as

$$\delta S_{21}(f, H_0) = \frac{S_{21}(f, H_0 + \delta H_0) - S_{21}(f, H_0 - \delta H_0)}{S_{21}(f, H_0)} \tag{7.3}$$

where H_0 is the external static applied magnetic field and δH_0 is the sweeping increment. Such a measurement is shown in Fig. 7.2. Fig. 7.2 shows the real part of the complex transmission $\mathrm{Re}(\delta S_{21})$ defined in equation 7.3 as a function of frequency f and H_0 at 5 K. The contrast in $\mathrm{Re}(\delta S_{21})$ is attributed to the excitation and detection of magnetic resonances at a certain frequency. Three distinctive sets of helimagnon resonances are identified (indicated in Fig. 7.2). In addition to the previously observed

[1] For detailed information see *Experimental observation of quantized helimagnon resonances in the chiral magnetic insulator Cu_2OSeO_3* by M. Weiler, A. Aqeel, M. Mostovoy, A. O. Leonov, S. Geprägs, R. Gross, H. Huebl, T. T. M. Palstra, & S. T. B. Goennenwein, to be submitted.

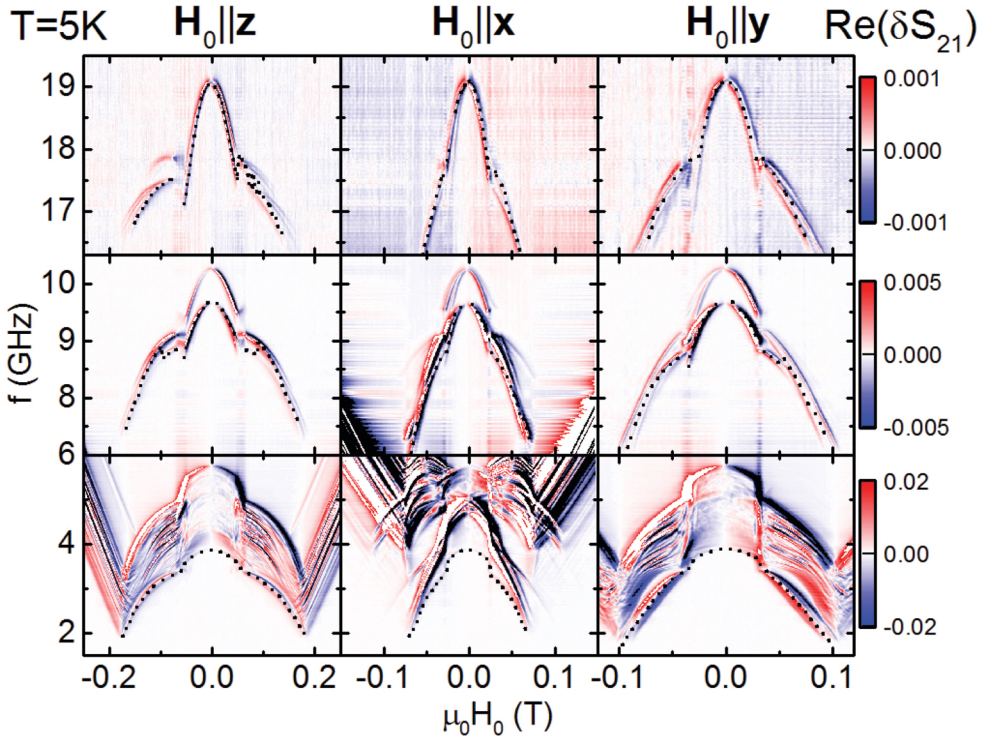

Figure 7.2: *Colorcoded* $\mathrm{Re}\delta S_{21}$ *(as defined in equation 7.3) spectra recorded as a function of f and* H_0 *at T = 5 K for three different orientations of the external magnetic field* H_0*, swept from positive to negative values. Contrast in* δS_{21} *corresponds to the detection of magnon resonances and the dotted lines correspond to the resonance frequencies.*

resonances in the literature [25, 26] at frequencies f $<$ 6 GHz, helimagnon resonances were also detected at higher frequencies (middle and top row in Fig 7.2) in grown Cu_2OSeO_3 crystals. Linewidth analysis suggests a magnetic damping $\alpha \leq 0.003$ which is substantially larger than the damping of yttrium iron garnet. Nevertheless, the damping of Cu_2OSeO_3 is comparable to the record value recently reported in a metallic ferromagnetic CoFe alloy at room temperature [27]. The low damping in high quality single crystals of Cu_2OSeO_3 in different magnetic phases opens the possibility to excite quantized helimagnons with exciting perspectives for spintronics in chiral magnets.

7.5 Conclusions

In conclusion, we have demonstrated a simple route that allows the growth of Cu_2OSeO_3 single crystals in a relatively short duration. The XRD analysis shows high quality single crystals. We observed both right-handed and left-handed enantiomers of Cu_2OSeO_3 and the absolute structure was fully determined by the Flack parameter analysis of the refined XRD pattern. The growth of crystals with both left- and right-handed structural chiralities can be useful to understand the coupling between structural and magnetic chiralities. The understanding of the coupling is important to control the magnetic textures such as skyrmions for spintronics applications.

Author contributions

A. Aqeel and J. Baas designed the experiments. Crystal growth and physical properties characterizations were done by A. Aqeel. A. Aqeel and G. R. Blake carried out the helicity analysis. A. Aqeel wrote the paper, involving all co-authors.

Bibliography

[1] S. Mühlbauer, B. Binz, F. Jonietz, C. Pfleiderer, A. Rosch, A. Neubauer, R. Georgii, and P. Bni, "Skyrmion Lattice in a Chiral Magnet," *Science* **323**(5916), pp. 915–919, 2009.

[2] F. Jonietz, S. Mühlbauer, C. Pfleiderer, A. Neubauer, W. Münzer, A. Bauer, T. Adams, R. Georgii, P. Bni, R. A. Duine, K. Everschor, M. Garst, and A. Rosch, "Spin Transfer Torques in MnSi at Ultralow Current Densities," *Science* **330**(6011), pp. 1648–1651, 2010.

[3] K. Shibata, X. Z. Yu, T. Hara, D. Morikawa, N. Kanazawa, K. Kimoto, S. Ishiwata, Y. Matsui, and Y. Tokura, "Towards control of the size and helicity of skyrmions in helimagnetic alloys by spin-orbit coupling," *Nature Nanotechnology* **8**(10), pp. 723–8, 2013-10.

[4] X. Z. Yu, N. Kanazawa, Y. Onose, K. Kimoto, W. Z. Zhang, S. Ishiwata, Y. Matsui, and Y. Tokura, "Near room-temperature formation of a skyrmion crystal in thin-films of the helimagnet fege.," *Nature Materials* **10**(2), pp. 106–109, 2011.

[5] W. Münzer, A. Neubauer, T. Adams, S. Mühlbauer, C. Franz, F. Jonietz, R. Georgii, P. Böni, B. Pedersen, M. Schmidt, A. Rosch, and C. Pfleiderer, "Skyrmion lattice in the doped semiconductor $Fe_{1-x}Co_xSi$," *Physical Review B* **81**, p. 041203, Jan 2010.

[6] I. Dzyaloshinsky, "A thermodynamic theory of "weak" ferromagnetism of antiferromagnetics," *Journal of Physics and Chemistry of Solids* **4**(4), pp. 241 – 255, 1958.

[7] T. Moriya, "Anisotropic Superexchange Interaction and Weak Ferromagnetism," *Physical Review* **120**, pp. 91–98, Oct 1960.

[8] T. Adams, A. Chacon, M. Wagner, A. Bauer, G. Brandl, B. Pedersen, H. Berger, P. Lemmens, and C. Pfleiderer, "Long-Wavelength Helimagnetic Order and Skyrmion Lattice Phase in Cu_2OSeO_3," *Physical Review Letters* **108**, p. 237204, Jun 2012.

[9] S. Seki, X. Z. Yu, S. Ishiwata, and Y. Tokura, "Observation of Skyrmions in a Multiferroic Material," *Science* **336**(6078), pp. 198–201, 2012.

[10] A. Maisuradze, Z. Guguchia, B. Graneli, H. M. Rønnow, H. Berger, and H. Keller, "μSR investigation of magnetism and magnetoelectric coupling in Cu_2OSeO_3," *Physical Review B* **84**, p. 064433, Aug 2011.

[11] I. Levatić, V. Šurija, H. Berger, and I. Živković, "Dissipation processes in the insulating skyrmion compound Cu_2OSeO_3," *Physical Review B* **90**, p. 224412, Dec 2014.

[12] M. Ozerov, J. Romhányi, M. Belesi, H. Berger, J.-P. Ansermet, J. van den Brink, J. Wosnitza, S. A. Zvyagin, and I. Rousochatzakis, "Establishing the Fundamental Magnetic Interactions in the Chiral Skyrmionic Mott Insulator Cu_2OSeO_3 by Terahertz Electron Spin Resonance," *Physical Review Letters* **113**, p. 157205, Oct 2014.

[13] N. Ogawa, S. Seki, and Y. Tokura, "Ultrafast optical excitation of magnetic skyrmions," *Scientific Reports* **5**, Apr. 2015.

[14] D. Hirobe, Y. Shiomi, Y. Shimada, J.-i. Ohe, and E. Saitoh, "Generation of spin currents in the skyrmion phase of a helimagnetic insulator Cu_2OSeO_3," *Journal of Applied Physics* **117**(5), pp. –, 2015.

[15] V. Dyadkin, K. Prša, S. V. Grigoriev, J. S. White, P. Huang, H. M. Rønnow, A. Magrez, C. D. Dewhurst, and D. Chernyshov, "Chirality of structure and magnetism in the magnetoelectric compound Cu_2OSeO_3," *Physical Review B* **89**, p. 140409, Apr 2014.

[16] G. Meunier and M. Bertaud, "Constantes cristallographiques de $CuSe_2O_5$, $CuSeO_3$ et Cu_2SeO_4," *Journal of Applied Crystallography* **9**, pp. 364–366, Aug 1976.

[17] H. Effenberger and F. Pertlik, "Die Kristallstrukturen der Kupfer(II)-oxo-selenite $Cu_2O(SeO_3)$ (kubisch und monoklin) und $Cu_4O(SeO_3)_3$ (monoklin und triklin)," *Monatshefte für Chemie / Chemical Monthly* **117**(8-9), pp. 887–896, 1986.

[18] J.-W. G. Bos, C. V. Colin, and T. T. M. Palstra, "Magnetoelectric coupling in the cubic ferrimagnet Cu_2OSeO_3," *Physical Review B* **78**, p. 094416, Sep 2008.

[19] M. Belesi, I. Rousochatzakis, H. C. Wu, H. Berger, I. V. Shvets, F. Mila, and J. P. Ansermet, "Ferrimagnetism of the magnetoelectric compound Cu_2OSeO_3 probed by ^{77}Se NMR," *Physical Review B* **82**, p. 094422, Sep 2010.

[20] J. B. Legma, G. Vacquier, and A. Casalot, "Chemical vapour transport of molybdenum and tungsten diselenides by various transport agents," *Journal of Crystal Growth* **130**(12), pp. 253 – 258, 1993.

[21] A. Klein, Y. Tomm, R. Schlaf, C. Pettenkofer, W. Jaegermann, M. Lux-Steiner, and E. Bucher, "Photovoltaic properties of WSe_2 single-crystals studied by photoelectron spectroscopy," *Solar Energy Materials and Solar Cells* **51**(2), pp. 181 – 191, 1998.

[22] G. Prasad and O. N. Srivastava, "The high-efficiency (17.1%) WSe_2 photo-electrochemical solar cell," *Journal of Physics D: Applied Physics* **21**(6), p. 1028, 1988.

[23] V. A. Chizhikov and V. E. Dmitrienko, "Microscopic description of twisted magnet Cu_2OSeO_3," *Journal of Magnetism and Magnetic Materials* **382**(0), pp. 142 – 151, 2015.

[24] V. Dmitriev, D. Chernyshov, S. Grigoriev, and V. Dyadkin, "A chiral link between structure and magnetism in MnSi," *Journal of Physics: Condensed Matter* **24**(36), p. 366005, 2012.

[25] Y. Onose, Y. Okamura, S. Seki, S. Ishiwata, and Y. Tokura, "Observation of magnetic excitations of skyrmion crystal in a helimagnetic insulator cu_2oseo_3," *Phys. Rev. Lett.* **109**, p. 037603, Jul 2012.

[26] T. Schwarze, J. Waizner, M. Garst, A. Bauer, I. Stasinopoulos, H. Berger, C. Pfleiderer, and D. Grundler, "Universal helimagnon and skyrmion excitations inmetallic, semiconducting and insulating chiralmagnets," *Nature Mater.* **14**(6078), pp. 478–483, 2015.

[27] M. A. W. Schoen, , D. Thonig, M. L. Schneider, T. J. Silva, H. T. Nembach, O. Eriksson, O. Karis, and J. M. Shaw, "Ultra-low magnetic damping of a metallic ferromagnet," *Nature Phys.* **12**(6078), pp. 839–842, 2016.

Summary

Controlling the generation, propagation and detection of pure spin currents carried by magnons is the essence of the field of magnon spintronics. In this thesis, I investigate pure spin currents generated in a normal metal and the spin currents carried by thermally generated magnons in magnetic insulators. I investigate these spintronic phenomena in the prototype yttrium iron garnet (YIG)|platinum (Pt) bilayer system (chapter 3) and in different non-collinear magnetic insulator|Pt bilayer systems (chapters 4, 5). The spin currents are driven by both charge currents and temperature gradients. I also study the growth of non-collinear magnetic insulators (chapter 7). Moreover, I investigate the role of ever-present background contributions in these spintronic experiments by a magnetic probe based on a muon spectroscopy technique (chapter 6).

The electron can be considered as a particle, with charge and magnetic character "spin". It behaves as a tiny magnet with an intrinsic magnetic moment. The motion of an electron (charge current) is thus automatically accompanied with the flow of angular momentum, i.e., a spin current. In paramagnetic metals, the number of electrons with spin pointing in one direction, "spin-up" electrons, is equal to the number of electrons with spins pointing in the opposite direction, "spin-down" electrons. Hence, these charge currents do not carry a net spin current. However, in ferromagnetic (ferrimagnetic) materials, the majority of electron spins point in one direction making the material magnetic. Therefore, a charge current in a magnetic material effectively transports a spin current. This spin current can be injected into an adjacent non-magnetic metal in close proximity. The main complexity of working with spin currents is that these injected spin currents can decay over short distances of the order of hundreds of nanometers due to interactions with their environment. The relation between charge and spin current transport has led to spin-based electronics - known as spintronics. The recent developments in the field of spintronics

have shown that pure spin currents can be generated transverse to a charge current. This effect is known as the spin-Hall effect (SHE). In the SHE, a moving electron in a paramagnetic metal is deflected from its initial trajectory (along the charge current flow direction) due to the spin-orbit interaction (an interaction of a particle's spin momentum with its orbital momentum). The deflection direction is opposite for spin-up electrons and spin-down electrons. Therefore, when a charge current flows in materials with strong spin-orbit coupling (heavy metals like Pt) the electrons with opposite spins deflect in different directions, resulting in a spin current transverse to the charge current direction. The inverse of this effect (ISHE) also exists in which a spin current converts to a transverse charge current.

Spin currents can also flow in magnetic insulators carried by magnetic excitations known as magnons. The relation between spin currents in metals and spin currents carried by magnons in insulators has led to a new research field - known as "magnon spintronics". In this thesis, the transfer of spin currents across the metal|magnetic interfaces is investigated by two effects: spin-Hall magnetoresistance (SMR) and spin-Seebeck effect (SSE). In the SSE, a temperature gradient is applied over a non-magnetic NM|ferromagnetic FM stack which generates thermal magnons (magnetic excitations) in the FM layer. These magnons carry a spin current with spin polarization along the average magnetization direction of the FM layer. This spin current carried by thermal magnons transfers into the adjacent NM layer and converts into a charge current by the ISHE - known as the SSE signal. As the spin current goes from the FM to NM layer through the interface, the quality of the interface plays an important role.

The first experiment (chapter 3) investigates the role of the interface quality in the SSE. In this experiment, a collinear magnetic insulator yttrium iron garnet (YIG) is investigated. In this system all magnetic moments can be easily aligned along the applied magnetic field direction (with magnetic field strength of few millitesla). Before sputtering the Pt layers on top of YIG films, different YIG surfaces are prepared by polishing with coarse or soft polishing particles of different sizes. The creation of a temperature gradient over these Pt|YIG stacks is achieved by using external heaters. Interestingly, the SSE signal observed in the NM layer depends on the surface roughness of the YIG layer and the type of polishing (i.e, coarse or soft polishing particles). A second experiment is the simultaneous detection of the SMR and SSE in the NM|FM stacks. In the SMR, the resistance of the NM layer changes depending on the magnetization direction of the FM layer underneath. In this effect, the SHE and ISHE both play a concerted role. This effect is measured by rotating the NM|FM stack in a magnetic field and measuring the resistance of the NM layer along (or transverse to) the applied current direction. Importantly, this effect is sensitive to the surface magnetization of the magnetic layer and provides the possibility to electrically detect the magnetization direction of this insulating layer. The charge current

sent through the NM layer creates a thermal gradient across the NM|FM stack due to Joule heating. This thermal gradient will create the SSE which can be separated from the SMR signal by a technique called lock-in detection. The principle is that the SMR scales linearly with the applied current while the SSE scales quadratically. By simultaneously, but separately, measuring the SMR and SSE in a single measurement, detailed information about the surface and bulk magnetization of the magnetic layer can be determined. This experiment is performed on the Pt|YIG stack (chapter 4) by measuring the SMR and SSE simultaneously. In the literature, mostly the prototype YIG collinear magnet has been investigated. However, magnetic insulators exhibit a large variety of magnetic orders, varying from collinear magnetic states in which all magnetic moments align along one axis to non-collinear states with magnetic moments aligned in complex spin arrangements. In non-collinear magnetic insulators, usually a large magnetic field of several Tesla is needed to align all magnetic moments along the applied field. In such magnetic systems, the competing magnetic interactions (spin frustration) do not favor a parallel arrangement of magnetic moments, resulting a complex arrangement, such as triangles or spirals. An example of such a system is $CoCr_2O_4$ (CCO) (discussed in chapter 4) in which at low temperatures the spin frustration leads to a conical spiral arrangement of magnetic moments. Even a magnetic field of 30 T is not sufficient to fully align all magnetic moments along the applied field direction. To study the sensitivity of the SMR and SSE towards the surface and bulk magnetization of a magnetic insulator, I performed experiments on the Pt|CCO bilayer system (chapter 4). I observe that the SMR and SSE both show large anomalies at the magnetic transitions where the collinear magnetization of the CCO films transforms to the conical spiral state. The large changes in the SMR and SSE signals are related to the non-collinear magnetization of the insulating CCO magnetic layer. This experiment establishes that both the SMR and SSE are powerful tools that complement ferromagnetic resonance and neutron scattering techniques to analyze the magnetization dynamics of complex oxides like CCO.

The third investigation in my thesis is similar to the second one in which the SMR and SSE are simultaneously detected. In this study a chiral non-collinear magnetic insulator is used. In chiral magnets the Dzyaloshinskii-Moriya (DM) interaction can lead to a non-collinear magnetic order. In these magnetic systems, the DM interactions twist an initially collinear arrangement of magnetic moments to a certain handedness. This leads to the formation of chiral spin arrangements. The advantage of using such magnetic systems is their rich phase diagrams in which different magnetic states like helical, conical, skyrmions and collinear magnetic states (co-)exist at different temperatures and applied magnetic fields. For this purpose, we investigate the chiral magnetic insulator Cu_2OSeO_3 (CSO)|Pt bilayer system (chapter 5). I observe that the SMR can be used as an all-electric detection tool for different magnetic transitions of CSO, such as the helical and conical spiral magnetic states. The results

show the SMR to be sensitive to the orientation of the spiral wave vector and to the magnitude of the cone angle between the applied magnetic field direction and the magnetic moments in the spiral. Large discontinuities and anomalies in the SMR are observed when the magnetic order of the CSO changes from a single magnetic domain state to a multidomain state. The SSE generated due to Joule heating also shows strong sensitivity to changes in magnetic ordering of CSO. In the future perspective, it would be interesting to apply these techniques (SMR and SSE) to the detection of even more complex spin textures, such as the skyrmion crystal in these chiral magnets.

The fourth investigation described in this thesis (chapter 6) deals with the determination of the ever-present background contributions in these spintronic experiments. I used a muon spectroscopy technique (LEμSR) for this purpose. The LEμSR is a magnetic probe and is sensitive to small magnetic fields of the order of 0.1 mT. This technique can be used to detect the current-induced fields, e.g., due to the spins created by the SHE, Oersted fields or due to proximity effects at buried interfaces. In this experiment, a Au|YIG bilayer system is used to study the depth resolved magnetic fields in this system. I observe that the LEμSR can be used to resolve the small magnetic fields of the order of 0.04 mT associated with background signals present due to the interface roughness and Oersted fields.

In the last chapter of this thesis (chapter 7) a new method for growth of large single crystals of the chiral magnetic insulator CSO is demonstrated. I find that with this method both left- and right-handed crystals of CSO can be grown. The crystals have excellent quality gauged by single crystal x-ray diffraction and verified by observing the presence of higher harmonic modes in ferromagnetic resonance data. The same crystals have been used in this thesis for the spintronic experiments described in chapter 5.

Considerable experimental efforts have been made already on magnon spintronic effects in collinear magnetic insulators. The experiments in this thesis provide understanding of spintronic phenomena related to the generation and detection of spin currents in non-collinear magnetic insulators with complex magnetic spin structures, like helices and skyrmions. Additionally, a new route to grow high quality single crystals of non-collinear magnets is described along with the spin transport experiments on these crystals. These investigations lead to new insights regarding the sensitivity of the SMR towards the surface magnetization and the cone angle of the spiral spin structures. The combination of these results and the improved understanding of the physics involved in spin transport in non-collinear spin structures leads to new possibilities to electrically detect and manipulate nanomagnetic structures, such as domain walls and skyrmions. A technique like SMR, with which one can observe nanosized objects by measuring electric currents, would be indispensable for utilizing skyrmions and other topological defects as information carriers in

the next generation spintronics devices.

Samenvatting

Het beheersen van de generatie, de verspreiding en de detectie van pure spinstromen is de essentie van het onderzoeksgebied van magnonspintronica. In dit proefschrift onderzoek ik pure spinstromen die worden opgewekt in een normaal metaal en spinstromen die getransporteerd worden door thermisch gegenereerde magnonen in magnetische isolatoren. Ik onderzoek deze spintronische fenomenen in verschillende systemen: een tweelaags systeem bestaande uit een laag yttriumijzergranaat (YIG) en een laag platina (Pt) (Hoofdstuk 3) en verschillende noncollineaire magnetische tweelaagse isolator|PT-systemen (Hoofdstuk 4, 5). Spinstromen worden gedreven door zowel de ladingstroom en temperatuurgradinten. Ik bestudeer ook de groei van de niet-collineaire magnetische isolatoren (Hoofdstuk 7). Bovendien onderzoek ik de rol van de altijd aanwezige achtergrondbijdragen in deze spintronische experimenten door gebruik te maken van een magnetische sensor op basis van een muonspectroscopietechniek (Hoofdstuk 6).

Het elektron kan worden beschouwd als een deeltje met lading en de magnetische eigenschap "spin". Het gedraagt zich als een kleine magneet met een intrinsiek magnetisch moment. De stroom elektronen (laadstroom) gaat dus automatisch samen met een stroom van spins, d.w.z. een spinstroom. In paramagnetische metalen is het aantal elektronen met spin in een bepaalde richting (bijvoorbeeld "spin-up" elektronen) gelijk aan het aantal elektronen met spin in de tegengestelde richting ("spin-down" elektronen). Hierdoor transporteren deze laadstromen geen netto spinstroom. In ferromagnetische (ferrimagnetische) materialen wijzen de meeste elektronspins in n richting, wat het materiaal magnetisch maakt. Daardoor draagt een laadstroom in een magnetisch materiaal tegelijkertijd een spinstroom. Deze spinstroom kan worden genjecteerd in een direct aangrenzend niet-magnetisch metaal. Het meest complexe aspect van het werken met spinstromen is dat deze genjecteerde spinstromen door interactie met hun omgeving kunnen vervallen over zeer korte afstanden (in de orde van enkele honderden nanometers). De relatie tussen laad- en

spinstroomtransport heeft geleid tot op spin-gebaseerde elektronica, beter bekend als spintronica. Recente ontwikkelingen op het gebied van de spintronica laten zien dat pure spinstromen loodrecht op een laadstroom kunnen worden gegenereerd.

Dit effect staat bekend als het spin-Hall-effect (SHE). In het SHE wordt een bewegend elektron in een paramagnetisch metaal afgebogen van zijn oorspronkelijke baan (langs de stroomrichting van de laadstroom) door de spin-baaninteractie (een interactie van de spin (intrinsieke impulsmoment) met zijn baanimpulsmoment). De afbuigingsrichting is tegengesteld voor elektronen met spin up en spin down. Wanneer er in materialen met een sterke spin-baankoppeling (zoals zware metalen als Pt) een laadstroom stroomt, buigen hierdoor de elektronen met tegengestelde spins in verschillende richtingen af, wat resulteert een spinstroom loodrecht op de richting van de laadstroom. Het omgekeerde effect bestaat ook (ISHE), waarin een spinstroom wordt omgezet in een laadstroom die er loodrecht op staat.

Spinstromen kunnen ook door magnetische isolatoren stromen, waarin de spinstroom getransporteerd wordt door magnetische excitaties bekend als magnonen. De relatie tussen spinstromen in metalen en spinstromen in isolatoren heeft geleid tot een nieuw onderzoeksgebied, bekend als "magnonspintronica". In dit proefschrift wordt de overdracht van spinstromen over het grensvlak van metaal|magnetische isolator onderzocht door twee effecten: het spin-Hall-magneetweerstandseffect (SMR) en het spin-Seebeckeffect (SSE). In het SSE wordt een temperatuurgradint aangebracht over een niet-magnetisch (NM)- ferromagnetische (FM) stapeling die thermische magnonen genereert in de FM-laag. Deze magnonen dragen een spinstroom met spin die gepolariseerd is langs de gemiddelde magnetisatierichting van de FM-laag. Vervolgens wordt deze spinstroom overgedragen aan de aangrenzende NM-laag en door het ISHE omzet in een laadstroom - bekend als het SSE-signaal. Omdat de spinstroom van de FM-laag naar de NM-laag gaat via het grensvlak, speelt de kwaliteit van het grensvlak een belangrijke rol.

Het eerste experiment (hoofdstuk 3) onderzoekt de rol van de kwaliteit van het grensvlak bij het SSE. In dit experiment werd een collineaire magnetische isolator yttriumijzergranaat (YIG) onderzocht. In dit systeem kunnen alle magnetische momenten gemakkelijk worden uitgelijnd in de richting van een aangebracht magnetisch veld (met magnetische veldsterkte van enkele millitesla).

Voordat de Pt-lagen op de YIG films werden aangebracht, werden verschillende oppervlakken van YIG voorbereid door deze te polijsten met grove of zachte polijstdeeltjes van verschillende grootte. Het aanbrengen van een temperatuurgradint over de Pt|YIG stapelingen wordt gedaan door externe verwarmingselementen. Interessant is dat het SSE-signaal (dat waargenomen wordt in de NM-laag) afhangt van de oppervlakteruwheid van de YIG-laag en het type polijstmateriaal (d.w.z., grove of zachte polijstdeeltjes).

Een tweede experiment omvat het gelijktijdig detecteren van de SMR- en SSE-

signalen in de NM|FM stapelingen. Bij SMR verandert de weerstand van de NM-laag afhankelijk van de magnetisatierichting van de FM-laag eronder. In dit effect spelen het SHE en het ISHE beide een rol. Dit effect wordt gemeten door het NM|FM-systeem te draaien in een magnetisch veld, terwijl de weerstand van de NM-laag parallel aan (of loodrecht op) de aangebrachte stroomrichting gemeten wordt. Belangrijk is dat dit effect gevoelig is voor de oppervlaktemagnetisatie van de magnetische laag, wat het mogelijk maakt om de magnetisatierichting van deze isolerende laag elektrisch te detecteren. Door Jouleopwarming als gevolg van de laadstroom die door de NM-laag gezonden wordt, ontstaat in het NM|FM-systeem een temperatuurgradint. Deze gradint leidt tot een SSE-signaal dat van het SMR-signaal kan worden gescheiden door middel van een techniek genaamd Lock-Indetectie. Dit is mogelijk doordat het SMR-signaal lineair schaalt met de aangelegde stroom, terwijl het SSE-signaal kwadratisch schaalt. Door gelijktijdig (maar los van elkaar) het SMR-signaal en het SSE-signaal te meten, wordt gedetailleerde informatie verkregen over de magnetisatie van het oppervlak en van de bulk van de magnetische laag. Dit experiment werd uitgevoerd op de Pt|YIG stapeling (hoofdstuk 4).

In de literatuur is vooral de collineaire magneet YIG onderzocht. Echter, magnetische isolatoren vertonen een grote verscheidenheid aan magnetische ordeningen, varirend van collineaire magnetische toestanden, waarin alle magnetische momenten uitlijnen langs n as, tot niet-collineaire toestanden, met magnetische momenten in complexe spinordeningen. In niet-collineaire magnetische isolatoren is meestal een groot magnetisch veld van verscheidene Tesla nodig om alle magnetische momenten uit te lijnen langs het aangelegde veld. In zulke magneetsystemen leiden de concurrerende magnetische interacties (spinfrustratie) tot complexe ordeningen, zoals driehoeken of spiralen, omdat een parallelle rangschikking van magnetische momenten energetisch ongunstiger is. Een voorbeeld van een dergelijk systeem is $CoCr_2O_4$ (CCO) (besproken in hoofdstuk 4) waarin bij lage temperaturen de spinfrustratie leidt een conische spiraalordening van magnetische momenten. Zelfs een magnetisch veld van 30T is niet voldoende om alle magnetische momenten volledig in de aangelegde veldrichting te laten wijzen. Om de gevoeligheid van het SMR en het SSE voor de magnetisatie van het oppervlak en de bulk van een magnetische isolator, heb ik experimenten uitgevoerd op het systeem bestaande uit een laag Pt en een laag CCO (hoofdstuk 4). Ik heb waargenomen dat de SMR en SSE beide grote onregelmatigheden tonen bij de magnetische overgangen waar de collineaire magnetisatie van de CCO-laag verandert in de conische spiraaltoestand. De grote veranderingen in de SMR- en SSE-signalen hebben betrekking op de niet-collineaire magnetisatie van de magnetisch isolerende CCO-laag. Dit experiment stelt dat metingen aan zowel het SMR en het SSE krachtige gereedschappen zijn die technieken als ferromagnetische resonantie en neutronenverstrooiing aanvullen om de magnetisatie dynamica van complexe oxides als CCO te analyseren.

Het derde onderzoek in mijn proefschrift is vergelijkbaar met het tweede waarin de SMR en SSE gelijktijdig gedetecteerd worden. In deze studie wordt een chirale niet-collineaire magnetische isolator gebruikt in plaats van een collineaire magneet. In chirale magneten kan de Dzyaloshinskii-Moriya interactie (DM) leiden tot een niet-collineaire magnetische ordering. In zulke magnetische systemen twist de DM-interactie de aanvankelijk collineaire rangschikking van magnetische momenten om een zekere chiraliteit. Dit leidt tot de vorming van chirale rotatieordeningen. Het voordeel van dergelijke magnetische systemen is hun rijke fasediagram, waarin verschillende magnetische toestanden, zoals spiraalvormige, conische, skyrmionische en collineaire toestanden, (soms tegelijkertijd) bestaan bij verschillende temperaturen en aangelegde magnetische velden. Hiertoe onderzoeken we het tweelaagse systeem bestaande uit de chirale magnetische isolator Cu_2OSeO_3 (CSO) en Pt (hoofdstuk 5). Ik neem waar dat het SMR kan worden gebruikt voor de volledig elektrische detectie van verschillende magnetische overgangen van CSO, zoals de spiraalvormige en conische spiraaltoestanden. De resultaten tonen dat het SMR gevoelig is voor de orintatie van de golfvector van de spiraal en de grootte van de kegelhoek tussen de magnetische veldrichting en de magnetische momenten in de spiraal. Grote discontinuteiten en afwijkingen worden waargenomen in het SMR wanneer de magnetische orde van CSO verandert van een toestand met een enkel magnetisch domein naar een multidomeintoestand. De SSE, die gegenereerd wordt door jouleopwarming, toont ook sterke gevoeligheid voor veranderingen in de magnetische ordening van CSO. In de toekomst zou het interessant zijn om deze technieken (SMR en SSE) toe te passen voor detectie van nog complexere rotatietexturen, zoals het skyrmionkristal in deze chirale magneten. Het vierde onderzoek dat in dit proefschrift (hoofdstuk 6) beschreven wordt, houdt zich bezig met de bepaling van de altijd aanwezige achtergrondbijdragen in deze spintronische experimenten. Hier gebruik ik een muonspectroscopietechniek (LEμSR) voor dit doel. De (LEμSR) is een magnetische sonde en gevoelig voor kleine magnetische velden in de orde van 0,1 mT. Deze techniek kan worden gebruikt om door stroom genduceerde velden te detecteren, bijvoorbeeld velden die veroorzaakt worden door de spins in het SHE, Oerstedvelden of velden als gevolg van nabijheidseffecten op verborgen grensvlakken. In dit experiment wordt een Au|YIG dubbellaag gebruikt om hierin de diepteafhankelijke magnetische velden te bestuderen. Ik vond dat de (LEμSR) kan worden gebruikt om de kleine magnetische velden in de orde van 0,04 mT waar te nemen die in verband staan met de achtergrondsignalen die aanwezig zijn vanwege de grensvlakruwheid en Oerstedvelden.

In het laatste hoofdstuk van dit proefschrift (hoofdstuk 7) wordt een nieuwe methode voor de groei van grote eenkristallen van de chirale magnetische isolator CSO gedemonstreerd. Ik heb ontdekt dat met deze methode zowel links- als rechtshandige kristallen van CSO verkregen kunnen worden. De kristallen hebben

een uitstekende kwaliteit, gemeten door eenkristalrntgendiffractie en geverifieerd door het waarnemen van de aanwezigheid van hogere harmonische modi in de ferromagnetische resonantiedata. Diezelfde kristallen zijn in dit proefschrift gebruikt voor de spintronische experimenten beschreven in hoofdstuk 5. Uitgebreid onderzoek naar de magnonspintronische effecten van collineaire magnetische isolatoren is reeds gepubliceerd. De experimenten in dit proefschrift bieden begrip van spintronische verschijnselen die in verband staan met de opwekking en detectie van spinstromen in niet-collineaire magnetische isolatoren met complexe magnetische spinstructuren, zoals helices en skyrmions. Daarnaast is er een nieuwe route naar het groeien van hoogwaardige eenkristallen van niet-collineaire magneten beschreven samen met spintransportexperimenten in deze kristallen. Dit onderzoek leidt tot nieuwe inzichten met betrekking tot de gevoeligheid van het SMR voor de magnetisatie van het oppervlak en de kegelhoek van spinspiralen. De combinatie van deze resultaten en het verbeterde begrip van de gerelateerde natuurkunde van spintransport in niet-collineare spinstructuren leidt tot nieuwe mogelijkheden om nanomagnetische structuren, zoals domeinwanden en skyrmionen, elektrisch te detecteren en te manipuleren. Een techniek zoals SMR, waarmee men nano-objecten kan waarnemen door het meten van elektrische stromen, zou onmisbaar zijn voor het gebruik van skyrmionen en andere topologische defecten als informatiedragers in de volgende generatie van spintronica.

Acknowledgments

Here comes the part of the thesis that will be most read: the acknowledgements! It is a great pleasure to express my deepest appreciation to people who made my six years in Groningen most memorable and productive.

Firstly, I would like to thank Professor Thomas (Thom) Palstra and Professor Bart van Wees. Thom, five years ago I joined your group Solid State Materials for Electronics (SSME) for a master research project. I really enjoyed the degree of creative freedom you gave me during my master project. Thanks for trusting me and giving me further the opportunity to do a joint PhD research project on "spintronics" with you and with professor Bart van Wees in the group of Physics of nanodevices (FND). Thom, you are a great scientist and a true leader. I am very inspired by your scientific approach and by your friendly and motivating way of discussion. I am very thankful for your supervision and great patience. You always asked excellent inspiring and motivating questions. At rough times, I always felt secure in your guidance and trust. Thom, you gave me many world-wide collaboration opportunities, which build a good international perspective for my future. I really appreciate that you joined for a full week at the beam-time Switzerland, regardless of your very busy schedule. I would never be able to thank you enough for your help and support. Bart, first, I want to thank you for very warm welcome in your group and giving me the opportunity to work with many smart people during my PhD. I truly admire your analytical skills, deep understanding of physics and your ability to quickly pinpoint mistakes. It was a luxury to have the weekly metallic spintronics meetings. Bart you are an outstanding physicist with an impressive research group. I am very thankful for your guidance and support throughout my PhD.

Dear Professors Christian Back, Bert Koopmans and Justin Ye, thank you for being part of the reading committee and for valuable comments and suggestions to improve my thesis. I hope, in the near future, to get the opportunity to thank you in person. Here I also want to thank my two paranymphs, Arjan Burema and Machteld Kamminga for taking this responsible task so seriously (right?).

I would like to thank now Dr. Ivan Vera-Marun at UMAN Manchester. Ivan, I am

greatly indebted to you. You were always amazingly kind to spend several hours of your valuable time with me at RuG or via Skype to discuss our experiments. Your involvement with many PhD projects in Netherlands and outside (also the beam facility, Switzerland) signifies the desire you have to explain and understand the physics involved. You are a talented physicist with a great enthusiasm and a broad vision. In turbulent times, you were the most encouraging person for me to continue our projects. I always felt motivated after talking to you. You were the first one who collaborated with me and guided me in several aspects including the FND setups, when I was just starting. I learned a lot from you. Thank you!

I would like to thank all my collaborators and colleagues whom I have provided with various samples to broaden my scientific perspective: to Prof. Sebastian Goennenwein at TU Dresden, Prof. Rudolf Gross, Dr. Mathias Weiler, Dr. Hans Hübl and Dr. Stephan Geprägs at TUM Munich for the project on the FMR measurements, to Prof. Paul H.M. van Loosdrecht, Rolf Versteeg at UOC Cologne for the spectroscopic ellipsometry measurements, to Prof. Catherine Pappas and Fengjiao Qian at TU Delft for AC susceptibility measurements. Sebastian, I want to express special my gratitude to you for inviting me to TUM and very insightful discussions. I am really thankful to Zaher Salman at PSI, Switzerland, who spend several weeks of his valuable time in helping me to get twice the beam-time at LEμSR facility, in performing the experiments and analysing the data which resulted into chapter 6 of this dissertation. My special thanks goes to Prof. Alexandre Revcolevschi and Dr. Romuald Saint-Martin at ICMMO Paris for sending me several $SrCuO_2$ crystals for the project on low-dimensional magnetic insulators and for a very kind hospitality at the institute. Thank you!

I benefited a lot from my collaborators, Prof. Gerrit Bauer and Prof. Maxim Mosotvoy. Maxim, I am greatly indebted to you. Without your deep understanding of magnetism, we would not be able to interpret the experimental findings in chiral magnets. You were always amazingly kind to spend several hours to discuss and simulate my data. You are one of the most important reasons that I am still in the topic of noncollinear magnetism. My special thank to Gerrit, you actually motivated me to continue my work on complex magnetic insulators, I always enjoyed our scientific discussions. Your positive and brilliant input enormously improved my work.

I am very thankful to our professors Caspar, Tamalika, Beatriz and Graeme for their useful inputs during our weekly group meetings. Caspar, thank you so much for always being very kind. I really appreciate your guidance and support as the Top master programme coordinator in making a right choice for my PhD. Tamalika, I want to thank you specially for always being very kind, motivating and friendly. I cordially appreciate all your useful inputs during my master and PhD. Beatriz, I want to express my gratitude to you. You were always willing to help us in all sci-

entific problems and lab issues, regardless of your very busy schedule. Graeme, I cannot think of resolving enantiomers of chiral magnets without your help. I would not be able to thank you enough for helping me in XRD and spending several hours from your valuable time with me in the XRD room in determining absolute structures. You are a very kind, humble and brilliant scientist, I really enjoyed our crystal growth project discussions.

I was lucky to work with many smart and supportive colleagues in the SSME group whom I would like to thank: Mart, Yingfen, Hong, Laaya, Guowei, Anil, Phu, Jordi, Silng, Machteld, Arnoud and Monica. Arnoud, I owe you a very special thanks as my Top master colleague, my office mate and my first secret collaborator in PhD. We shared the same spot in building 18 for almost six years and I really enjoyed it. We had a lot of healthy arguments and funny fights. It was a pity that due to a particular reason your name was not in the author list in my first publication and I really admire that you never blamed me for this. All your efforts in making Labview programmes for me, your kindness, enthusiam, patience and positive attitude were very helpful for me through out my PhD. You are not only a good scientist but also a very trust-worthy colleague. I wish you a lot of success and a very happy life with Jolanda. Special thanks to my roomie Laaya. You are truly amazing person, calm, happy and peaceful. I really enjoyed our discussions with Iranian snacks. Your presence not only made our office lively but also green (due to your plants)! Guowei, you are one of my best colleagues. How I can possibly thank you enough for your endless support, care and all our great time together. Thank you for teaching me hydrothermal growth. You always showed a lot of interest to our long scientific and non-scientific discussions. I enjoyed playing squash with you. I would like to thank Anil, you are a nice person. I really enjoyed your positive attitude and my duty with you for furnaces. Thanks to Jordi, who accurately read my whole thesis and enlightened me with his smart comments. I really appreciate Mart for translating my summary in Dutch. Thank you! I would like to thank my brilliant and hard-working students, Eugene and Winfried. I really enjoyed working with both of you.

I am really grateful to former members of the SSME group: to Shiva, Justin, Silviya, Mai, Alex, Sylvia, Oleksiy, Syarif, Jeroen, Alim and Saeedeh for their kind support and useful suggestions. Saeedeh, I am really grateful to you for always being very kind, helpful and supportive. I am really impressed by your positive attitude. Keep the spirit! Jeroen, I really enjoyed our coffee breaks and all scientific discussions. You are kind, smart and possibly a rich person in near-future. Thank you for growing very good $CoCr_2O_4$ films for my electrical measurements. I wish you a great future in industry.

My special thanks to our group secretary Henriet. I really appreciate that you always make sure that everything work properly. I am truly grateful for all your assistance in all official matters including my teaching duties, Thom's agenda, and

reimbursement of travel expenses.

My gratitude goes now to all my colleagues in building 13 (FND group); Niko, Arijit, Malik, Paul, Marcos, Jasper, Subir, Gaurav, Talieh, Joseph, Christian, Alok, Tom, Magda, Alok, Alina, Magda, Sander, Saurabh, Jakko, Erik (special thanks to you for always helping me in EBL), Tom Schouten, Sid, Roald, Xu, Ping (my best wishes for your future) and all others whom I have forgotten. My separate thanks especially to all people from metallic spintronics team including Jing, Juan, Ludo, Kumar, Timo, Joost, Fasil, Vincent, Geert and Frank. I am grateful to Nynke; you are a really kind, honest and well-organised scientist. I really appreciate your guidance in the SMR measurements, in which we succeed to get two nice publications. I hope we can collaborate in future too. I wish you a lot of success. Timo you are a very nice addition to FND, thank you for explaining me different spin transport measurements. I always enjoyed our scientific discussions and I appreciate your patience. I am sure that you will be a great dad. Bernard and Martijn, I would like to endlessly thank both of you for every time wire-bonding my samples. Johan and Martijn, I really appreciate your efforts for keeping all equipments efficiently running in clean-room and in other FND labs. Thank you!

For all the technical assistance, I would like to thank our technicians Jacob Baas and Henk Bonder. Henk, I am really grateful to you for always being very kind and supportive. Thank you for helping me in modifying the PPMS stick and pucks. Jacob, I almost learned everything from you in the physics and chemistry labs. Without your help I would not be able to make my hands dirty in growing crystals which led to several nice publications. I really appreciate that you could appear anytime in the lab whenever I needed you. Your help was not limited to lab, even outside the lab you were a best friend. Heel erg Bedankt! My gratitude to my colleagues from other groups in RuG who were very supportive: to Davood, Oleksandr (Sasha), Lei, Arunesh, Julius and Evgeniia. Thanks to my best friend Rianne. I would like to thank all Pakistani fellows here, Imran Fazal, Maria, Safdar, Nayeema, Samina, Foqia, Tashfeen, Naureen, Ali, Memona, Ghufrana Samin, Nazia, Aqdas, Younus and Durdana Younus.

At the end, I would like to acknowledge the prayers, best wishes and all the unconditional support of my family: Kishwar Naz (my beloved mother), Muhammad Aqeel Zia (my late father), Abdullah Aqeel, Maria Aqeel, Sara Aqeel, Fatima, Abdur Rehman, Abdul Hadi, Shanzay, and my late grandfather (Nana Ji). My sweet dad and my mother, both of you are always the source of motivation for me. I always remember your sweet words and the golden time we had together. It is beyond words to thank you, my lovely parents.

Aisha Aqeel
Punjab Pakistan (January 10, 2017)

List of publications

1. **Surface sensitivity of the spin Seebeck effect [Chapter 3]**
   A. Aqeel, I. J. Vera-Marun, B. J. van Wees & T. T. M. Palstra
   J. Appl. Phys. **116**, 153705 (2014) [doi: 10.1063/1.4897933]

2. **Self-Assembly of Ferromagnetic OrganicInorganic Perovskite-Like Films**
   N. Akhtar, A. O. Polyakov, A. Aqeel, P. Gordiichuk, G. R. Blake, J. Baas, H. Amenitsch, A. Herrmann, P. Rudolf & T. T. M. Palstra
   Small **10**, 4912 (2014) [doi: 10.1002/smll.201400259]

3. **Spin-Hall magnetoresistance and spin Seebeck effect in spin-spiral and paramagnetic phases of multiferroic $CoCr_2O_4$ films [Chapter 4]**
   A. Aqeel, N. Vlietstra, J. A. Heuver, G. E. W. Bauer, B. Noheda, B. J. van Wees & T. T. M. Palstra
   Phys. Rev. B **10**, 4912 (2015) [doi: 10.1103/PhysRevB.92.224410]

4. **Phase diagram and magnetic relaxation phenomena in Cu_2OSeO_3**
   F. Qian, H. Wilhelm, A. Aqeel, T.T.M. Palstra, A.J.E. Lefering, E. H. Brück & C. Pappas
   Phys. Rev. B **94**, 064418 (2016) [doi: 10.1103/PhysRevB.94.064418]

5. **Optically probing symmetry breaking in the chiral magnet Cu_2OSeO_3**
   R. B. Versteeg, I. Vergara, S. D. Schäfer, D. Bischoff, A. Aqeel, T. T. M. Palstra, M. Grüninger & P. H. M van Loosdrecht
   Phys. Rev. B **94**, 094409 (2016) [doi: 10.1103/PhysRevB.94.094409]

6. **Electrical detection of spiral spin structures in Pt|Cu_2OSeO_3 heterostructures [Chapter 5]**
   A. Aqeel, N. Vlietstra, A. Roy, M. Mostovoy, B. J. van Wees & T. T. M. Palstra
   Phys. Rev. B **94**, 134418 (2016) [doi: 10.1103/PhysRevB.94.134418]

7. **Dissipation phenomena and magnetic phase diagram of Cu_2OSeO_3 below 50 K**
   F. Qian, H. Wilhelm, A. Aqeel, T. T. M. Palstra, A. J. E. Lefering, E. H. Brück, and C. Pappas
   submitted in Phys. Rev. B (2016)

8. **Probing current-induced magnetic fields in Au|YIG heterostructure with low-energy muon spectroscopy [Chapter 6]**
   A. Aqeel, I. J. Vera-Marun, Z. Salman, B. J. van Wees & T. T. M. Palstra
   accepted in Appl. Phys. Lett. (2017)

9. **Magnetic functionality of thin film perovskite hybrids**
   A. O. Polyakov, N. Akhtar, A. Aqeel, P. Rudolf & T. T. M. Palstra
   to be submitted (2017)

10. **Growth and helicity of non-centrosymmetric Cu_2OSeO_3 crystals [Chapter 7]**
    A. Aqeel, J. Baas, G. R. Blake, & T. T. M. Palstra
    to be submitted in Crystal Growth & Design (2017)

11. **Spin-Hall magnetoresistance in multidomain helical spiral systems**
    A. Aqeel, M. Mostovoy, B. J. van Wees & T. T. M. Palstra
    accepted in J. Appl. Phys. D (2017)

12. **Experimental observation of quantized helimagnon resonances in the chiral magnetic insulator Cu_2OSeO_3**
    M. Weiler, A. Aqeel, M. Mostovoy, A. O. Leonov, S. Geprägs, R. Gross, H. Huebl, T. T. M. Palstra, & S. T. B. Goennenwein
    to be submitted (2017)